



**HAL**  
open science

# The Bose gas at large scattering lengths

Swann Piatecki

► **To cite this version:**

Swann Piatecki. The Bose gas at large scattering lengths. Quantum Gases [cond-mat.quant-gas]. ENS Paris - Ecole Normale Supérieure de Paris, 2015. English. NNT: . tel-01158248

**HAL Id: tel-01158248**

**<https://theses.hal.science/tel-01158248>**

Submitted on 30 May 2015

**HAL** is a multi-disciplinary open access archive for the deposit and dissemination of scientific research documents, whether they are published or not. The documents may come from teaching and research institutions in France or abroad, or from public or private research centers.

L'archive ouverte pluridisciplinaire **HAL**, est destinée au dépôt et à la diffusion de documents scientifiques de niveau recherche, publiés ou non, émanant des établissements d'enseignement et de recherche français ou étrangers, des laboratoires publics ou privés.

ÉCOLE DOCTORALE DE PHYSIQUE DE LA RÉGION PARISIENNE - ED 107  
ÉCOLE NORMALE SUPÉRIEURE



LABORATOIRE DE PHYSIQUE STATISTIQUE

Thèse de doctorat

---

The Bose gas  
at large scattering lengths

---

présentée par Swann PIATECKI  
pour obtenir le titre de docteur de l'École normale supérieure

Soutenue le 2 mai 2014 devant le jury composé de:

George BATROUNI	Rapporteur
Yvan CASTIN	Examineur
Cristiane DE MORAIS SMITH	Rapporteuse
Werner KRAUTH	Directeur de thèse
Anna MINGUZZI	Examinatrice



*À Élisabeth*



---

## Remerciements

---

Je remercie tout d'abord Werner Krauth de sa direction patiente, bienveillante et attentive de cette thèse, et de m'avoir initié aux simulations Monte-Carlo lors de son cours de master, en 2008. Je remercie Yvan Castin, Anna Minguzzi, George Batrouni et Cristiane de Morais Smith d'avoir accepté de prendre part au jury évaluant mon travail, pour ces deux derniers en tant que rapporteurs.

Pour les nombreuses conversations scientifiques que j'ai eues avec eux, et qui ont beaucoup apporté à mes travaux, je remercie également Sébastien Balibar, Frédéric Chevy, Markus Holzmann et Félix Werner. Au début de ma thèse, j'ai collaboré avec l'équipe Lithium du Laboratoire Kastler Brossel pour étudier le gaz de Bose au-delà du champ moyen. Cette collaboration s'est aussi avérée essentielle à la suite de mes recherches, car c'est à travers elle que j'ai été initié au problème du gaz de Bose unitaire. À ce titre, je tiens à remercier tout particulièrement Nir Navon. Je remercie aussi Marion Delehay, Ulrich Eisman, Igor Ferrier-Barbut, Sébastien Laurent, Andrew Grier et Benno Rem, et bien sûr Frédéric Chevy et Christophe Salomon.

Je dois mon intérêt pour la physique et les mathématiques, qui a abouti à cette thèse, à mes nombreux professeurs. La place manque pour les nommer tous, mais je tiens particulièrement à saluer Sébastien Aullen, Prebagaran Mouttou et Jean-Pierre Sanchez, Jean-Daniel Bloch et Nicolas Schlosser, et Gérard Mantin et Stéphane Olivier. Je remercie également l'équipe pédagogique de la préparation française aux Olympiades internationales de Physiques, et tout particulièrement Catherine Velay.

Pendant ma thèse, j'ai eu la chance d'enseigner aux élèves du Lycée Louis le Grand puis à ceux du parcours de physique de l'École normale supérieure, ce qui m'a permis de conserver une vision large de la physique, et donc un certain recul sur ma thèse. Je remercie leurs enseignants, pour les premiers Stéphane Olivier et Catherine Velay, et pour les seconds Bernard Derrida, Stephan Fauve et Emmanuel Trizac, de m'avoir confié cette tâche, mais aussi mes co-encadrants de travaux dirigés Éric Brunet, Aurélie Fargette, Benjamin Langlois et Guilhem Semerjian.

Pour avoir entretenu et ressuscité plusieurs fois nos serveurs de calculs, je remercie

spécialement Frédéric Ayrault, sans qui les simulations présentées ici n'auraient pas pu produire de résultats. Tant pour son support technique sans faille de mon ordinateur personnel que pour nos conversations sur Leonard Cohen, je remercie Zaire Dissi. Je remercie également Marie Gefflot, Annie Ribaudeau et Nora Sadaoui pour leur assistance bienveillante et sans faille dans toutes sortes de démarches administratives.

Pour m'avoir aidé à conserver une saine ambiance de travail à l'ENS, et pour les si nombreuses conversations dépassant largement le seul domaine de la physique, je remercie mes compagnons de bureau Étienne Bernard, Manon Michel, Maxim Berman, Sebastian Kapfer, Tommaso Comparin et Virgile Andreani. Je leur présente ici mes excuses pour les mauvais jeux de mots qui ont émaillé ces quatre années. À l'ENS, je remercie également mes nombreux co-thésards parmi lesquels Rémi Desbuquois, Michele Filippone, Fabien Nugier, Marc Santolini et Tarik Yefsah, ainsi que Fabien Souris et Kris van Houcke.

Parce que les bons moments que j'ai passés avec eux au cours de ma thèse ont été autant de bols d'air, je remercie sincèrement mes amis Alexandre «Jacky» et Claire, Anne, Guirec, Hadrien, Keihann et Sophie, Romain et Mandy, Sophie, Théodora et Mickaël, Thibaut, Thomas-Anis, Vincent, Xavier, et plus particulièrement Alexandre «Laza» et Kévin, qui ont relu cette thèse avec attention.

Pour finir, je remercie bien sûr mes parents, qui ont su me donner le goût de l'effort, de l'accomplissement individuel et de la persévérance. Plus largement, je remercie ma famille toute entière, pour avoir toujours été là et m'avoir soutenu pendant les meilleurs moments comme les moments difficiles: sans eux, ce travail aurait été encore plus ardu à accomplir. Et je remercie évidemment Élisabeth, sans qui tout ceci n'aurait simplement pas été possible.

In 1924, in three pioneering articles, Bose and Einstein showed that identical ideal bosons form a macroscopic quantum phase when the temperature is low enough that their wavefunctions start to overlap (Bose, 1924; Einstein, 1924, 1925). In this phase, since then known as a Bose–Einstein condensate, bosons are collectively described by a single wavefunction, that minimises their energy. Between this prediction and the first observation of a Bose–Einstein condensate in a cold-atom experiment seventy years later (Anderson *et al.*, 1995), theoretical tools that characterize the zero-temperature behaviour of non-ideal, weakly-interacting Bose–Einstein condensates became available (Gross, 1961, 1963; Pitaevskii, 1961). However, no theory currently describes the Bose gas in the regime where the interactions between bosons are resonant, a situation called *unitarity*, in which atomic gases suffer severe three-body losses (Rem *et al.*, 2013) that hinder their observation.

Nonetheless, at unitarity, systems of three bosons are known to exhibit a surprising Borromean behaviour: although two of them cannot bind, they form an infinite sequence of asymptotically universal trimer *Efimov states* (Efimov, 1970, 1971, 1979). These states remain elusive in experiments, but they were indirectly observed through the severe three-body losses that make the unitary Bose gas unstable (Kraemer *et al.*, 2006; Zaccanti *et al.*, 2009; Pollack *et al.*, 2009). It was later shown (von Stecher *et al.*, 2009) and observed (Ferlandino *et al.*, 2009) that, at unitarity, groups of four particles form states bound by the same effects as Efimov trimers, and clusters of up to 13 particles were found in numerical simulations at zero temperature (von Stecher, 2010). However, the many-body, thermodynamic behaviour of such cluster states has remained unknown.

This thesis is devoted to the study of the Bose gas with strong interactions using the quantum path-integral Monte Carlo simulation method, that, in the past, successfully addressed systems such as superfluid helium (Ceperley, 1995) and atomic Bose–Einstein condensates in the weakly-interacting regime (Krauth, 1996). The first chapter introduces concepts essential to this method, and consists in a description of the path-integral formalism using the free Bose gas as an example, and of powerful tools addressing the interactions between bosons.

The first results presented in this thesis were obtained in close collaboration with the Lithium group of Laboratoire Kastler Brossel at École normale supérieure, directed by Christophe Salomon, and in particular with his then PhD student Nir Navon. They concern the first correction to the mean-field zero-temperature equation of state of the weakly-interacting Bose gas, derived by [Lee, Huang, and Yang](#) in 1957. Both the simulations and the experiment allowed to confirm the grand-canonical equivalent of the Lee–Huang–Yang equation of state. The simulation also allowed to verify that the experiment was in the zero-temperature regime. These results were the object of [Publication 1](#), and are described in [Chapter 2](#), that starts with a recollection of scattering concepts and of mean-field theories in the weakly-interacting regime.

The rest of this thesis deals with the regime of unitary interactions. Before tackling the unitary Bose gas, it was necessary to make sure that Efimov trimers could be reproduced in a simulation. This point is addressed in [Chapter 3](#), that starts with a description of unitary interactions and of how they can be modelled in a simulation, and in which the Efimov effect is described both from a theoretical point of view and on the basis of the results of the simulation. [Chapter 4](#) describes a simulation of the unitary Bose gas, whose results agree with theoretical predictions such as the virial equation of state, and provide evidence for the existence of a new phase, the unitary Efimov liquid, which corresponds to the above-mentioned clusters of unitary bosons. Both [Chapter 3](#) and [Chapter 4](#) were the object of [Publication 2](#).

<b>General introduction</b>	<b>7</b>
<b>Contents</b>	<b>9</b>
<b>1 Bosons in the path-integral formalism</b>	<b>11</b>
1.1 Ideal Bose gas . . . . .	12
1.1.1 Free density matrix and permutations . . . . .	12
1.1.2 Path integrals . . . . .	13
1.2 Interacting Bose gas . . . . .	15
1.2.1 Trotter approximation . . . . .	15
1.2.2 Pair-product approximation . . . . .	17
1.2.3 Interaction boxes . . . . .	18
Appendix 1.A Metropolis algorithm . . . . .	19
<b>2 The repulsive weakly-interacting Bose gas</b>	<b>21</b>
2.1 The mean-field weakly-interacting Bose gas . . . . .	21
2.1.1 Scattering length . . . . .	21
2.1.2 Trapped bosons . . . . .	25
2.2 Beyond-mean-field corrections . . . . .	26
2.2.1 The Lee–Huang–Yang equation of state . . . . .	26
2.2.2 Path-integral simulation and comparison to experiments . . . . .	27
2.2.3 Numerical and experimental grand-canonical equation of state . . . . .	30
2.3 Conclusion . . . . .	31
<b>3 Efimov trimers in the path-integral formalism</b>	<b>33</b>
3.1 Unitary limit . . . . .	33
3.1.1 Square-well interaction potential . . . . .	34
3.1.2 Zero-range interaction potential . . . . .	36

3.2	Efimov effect . . . . .	38
3.2.1	Regularization of the zero-range interaction potential . . . . .	38
3.2.2	Path-integral argument . . . . .	39
3.2.3	Numerical simulation of a single Efimov trimer . . . . .	42
3.2.4	Universality of Efimov trimers . . . . .	50
3.3	Conclusion . . . . .	56
	Appendix 3.A Path-integral argument for the dimer state . . . . .	56
	Appendix 3.B Calculation of the pair-product zero-range correction factor . . . . .	58
	Appendix 3.C Hyperspherical coordinates . . . . .	62
<b>4</b>	<b>The unitary Bose gas</b>	<b>65</b>
4.1	High-temperature equation of state . . . . .	66
4.1.1	Many-body simulation . . . . .	66
4.1.2	Equation of state . . . . .	68
4.2	Phase diagram of the unitary Bose gas . . . . .	69
4.2.1	Transition to the Efimov liquid phase . . . . .	69
4.2.2	Simple model for the transition to the Efimov liquid phase . . . . .	74
4.2.3	Homogeneous phase diagram . . . . .	77
4.3	Unitary liquid in experimental systems . . . . .	79
4.3.1	Experimentally accessible regions of the phase diagram . . . . .	80
4.3.2	Experimental observables . . . . .	82
4.4	Conclusion . . . . .	83
	Appendix 4.A Path integrals and momentum distribution . . . . .	84
	4.A.1 Off-diagonal density matrix and momentum distribution . . . . .	84
	4.A.2 Momentum distribution of two interacting bosons . . . . .	85
	4.A.3 Simple algorithm to obtain the momentum distribution . . . . .	90
	<b>General conclusion</b>	<b>93</b>
	<b>Bibliography</b>	<b>95</b>
	<b>Publications</b>	<b>101</b>
	Publication 1 . . . . .	101
	Publication 2 . . . . .	107

---

Bosons in the path-integral formalism

---

As a computer performs only classical operations, it may seem challenging to account for the indistinguishability of quantum particles in a simulation. It is possible to work around this problem by mapping indistinguishable particles onto distinguishable particles, an approach followed in quantum path-integral Monte Carlo simulations, which are based on non-symmetrized many-body wave-vectors in place of the usual ones, symmetrized over permutations of particles. For systems of identical bosons, the symmetrized wave-vectors may be expressed in terms of the non-symmetrized ones as:

$$|\mathbf{x}_1, \mathbf{x}_2, \dots, \mathbf{x}_N\rangle = \frac{1}{N!} \sum_{P \in \mathcal{S}_N} |\mathbf{x}_{P(1)}, \mathbf{x}_{P(2)}, \dots, \mathbf{x}_{P(N)}\rangle, \quad (1.1)$$

where  $\mathbf{x}_i$  represents the position of particle  $i$ , and  $\mathcal{S}_N$  is the symmetric group of order  $N$ , that contains all permutations of  $N$  particles. For bosons, the symmetrized wave-vector (on the left) is invariant when any two particles are swapped, but the non-symmetrized wave-vectors (on the right) are not. These describe distinguishable particles.

Thus, a configuration of  $N$  identical quantum particles may be mapped onto a superposition of  $N!$  configurations of distinguishable particles. Quantum path-integral Monte Carlo simulations work with such configurations, specified both by a permutation  $P$  and a set of positions  $(\mathbf{x}_1, \dots, \mathbf{x}_N)$ . These simulations do not enumerate all possible permutations one by one, which is practically impossible for a large number of particles. Instead, both positions and permutations are sampled using a Metropolis–Hastings algorithm ([Metropolis \*et al.\*, 1953](#); [Hastings, 1970](#)), that stochastically produces new configurations from existing configurations. The sum on permutations in Eq. 1.1 is not performed explicitly, but as part of the sum on realized configurations that allows to estimate the thermal averages of physical observables.

In this first chapter, I first review basic concepts used in path-integral simulations through the physics of the free Bose gas, and present Bose–Einstein condensation in terms

of permutations. I then describe how interactions between particles may be introduced in such a simulation.

## 1.1 Ideal Bose gas

In this first section, I provide a description of the gas of  $N$  identical ideal bosons of mass  $m$  to illustrate the path-integral formalism. The Hamiltonian of this system is

$$\hat{H}_{\text{free}} = \sum_{i=1}^N \frac{\hat{\mathbf{P}}_i^2}{2m}, \quad (1.2)$$

where  $\hat{\mathbf{P}}_i$  is the momentum operator of boson  $i$ .

### 1.1.1 Free density matrix and permutations

The central role in path-integral Monte Carlo simulations is played by the the  $N$ -body density matrix elements at inverse temperature  $\beta = 1/k_B T$ , where  $k_B$  is the Boltzmann constant. They correspond to the probability of the configuration consisting in a given permutation  $P$  and particles localized at positions  $(\mathbf{x}_1, \dots, \mathbf{x}_N)$ . These density matrix elements are defined as

$$\rho(\mathbf{x}_1, \dots, \mathbf{x}_N; \mathbf{x}_{P(1)}, \dots, \mathbf{x}_{P(N)}; \beta) = \langle \mathbf{x}_1, \dots, \mathbf{x}_N | e^{-\beta \hat{H}} | \mathbf{x}_{P(1)}, \dots, \mathbf{x}_{P(N)} \rangle. \quad (1.3)$$

For ideal bosons in free space, the Hamiltonian  $\hat{H}$  equals  $\hat{H}_{\text{free}}$ , and the free density matrix is a product of single-particle density matrices:

$$\rho_{\text{free}}(\mathbf{x}_1, \dots, \mathbf{x}_N; \mathbf{x}_{P(1)}, \dots, \mathbf{x}_{P(N)}; \beta) = \prod_{i=1}^N \rho_{\text{free}}(\mathbf{x}_i, \mathbf{x}_{P(i)}; \beta), \quad (1.4)$$

where single-particle density matrices are given by (Krauth, 2006)

$$\rho_{\text{free}}(\mathbf{x}, \mathbf{x}'; \beta) = \left( \frac{m}{2\pi\hbar^2\beta} \right)^{3/2} \exp \left[ -\frac{m(\mathbf{x}' - \mathbf{x})^2}{2\hbar^2\beta} \right]. \quad (1.5)$$

To describe a permutation  $P$ , it is useful to define *permutation cycles*. The length of the permutation cycle in which particle  $i$  stands corresponds, starting from  $i$ , to the number of iterations of  $P$  needed to find back particle  $i$ . As an example, if  $P(1) = 1$ , particle 1 is in a permutation cycle of length 1, and if  $P(1) = 2$ ,  $P(2) = 4$ , and  $P(4) = 1$ , particles 1, 2, and 4 are in a permutation cycle of length 3.

At high temperature, free bosons are in a classical gas phase, in which particles are distinguishable: for all bosons, any situation other than  $\mathbf{x}_{P(i)} = \mathbf{x}_i$  is unlikely. At a lower temperature, a macroscopic fraction of atoms starts to form permutation cycles longer than 1, a phenomenon corresponding to Bose–Einstein condensation. At zero temperature

$\beta \rightarrow \infty$ , because  $\rho_{\text{free}}(\mathbf{x}_i, \mathbf{x}_{P(i)}; \beta)$  does not depend on  $\mathbf{x}_i$  and  $\mathbf{x}_{P(i)}$ , we see from Eq. 1.4 that the probability of a configuration neither depends on positions nor on the permutation, and particles have the same probability to be in a permutation cycle of any length. Bose–Einstein condensation is illustrated in terms of cycle lengths in Fig. 1.1 for ideal bosons in a periodic box.

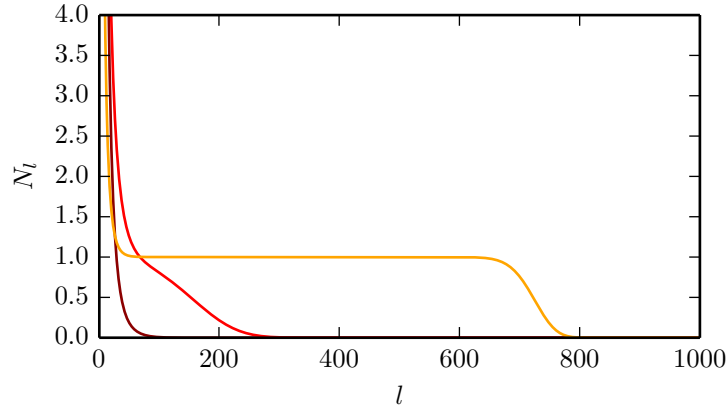


Figure 1.1: Number of bosons  $N_l$  in cycles of length  $l$  for 1000 ideal bosons in a periodic box at constant density, obtained from a recursion formula (Landsberg, 1961). At high temperature  $T/T_{\text{BEC}} = 1.2$  (brown line), long permutation cycles are unlikely. At the temperature of Bose–Einstein condensation  $T_{\text{BEC}}$  (red line), a macroscopic fraction of bosons are in long cycles, and at  $T = T_{\text{BEC}}/2$  (yellow line), the probability distribution has shifted towards its zero-temperature limit where it is equally likely for a boson to be in a cycle of any length.

### 1.1.2 Path integrals

The concept of path integrals comes from the convolution property that the density matrix satisfies for any value of  $\tau$ ,

$$\rho(\mathbf{x}_1, \dots, \mathbf{x}_N; \mathbf{x}_{P(1)}, \dots, \mathbf{x}_{P(N)}; \beta) \quad (1.6)$$

$$= \int d\mathbf{x}_1^{(1)} \dots d\mathbf{x}_N^{(1)} \langle \mathbf{x}_1, \dots, \mathbf{x}_N | e^{-\tau \hat{H}} | \mathbf{x}_1^{(1)}, \dots, \mathbf{x}_N^{(1)} \rangle \langle \mathbf{x}_1^{(1)}, \dots, \mathbf{x}_N^{(1)} | e^{-(\beta-\tau)\hat{H}} | \mathbf{x}_{P(1)}, \dots, \mathbf{x}_{P(N)} \rangle \quad (1.7)$$

$$= \int d\mathbf{x}_1^{(1)} \dots d\mathbf{x}_N^{(1)} \rho(\mathbf{x}_1, \dots, \mathbf{x}_N; \mathbf{x}_1^{(1)}, \dots, \mathbf{x}_N^{(1)}; \tau) \rho(\mathbf{x}_1^{(1)}, \dots, \mathbf{x}_N^{(1)}; \mathbf{x}_{P(1)}, \dots, \mathbf{x}_{P(N)}; \beta - \tau). \quad (1.8)$$

Using this relation, it is possible to introduce  $N(S - 1)$  additional degrees of freedom, so that

$$\rho(\mathbf{x}_1, \dots, \mathbf{x}_N; \mathbf{x}_{P(1)}, \dots, \mathbf{x}_{P(N)}; \beta) \quad (1.9)$$

$$= \int \prod_{s=1}^{S-1} d\mathbf{x}_1^{(s)} \dots d\mathbf{x}_N^{(s)} \prod_{s=0}^{S-1} \rho(\mathbf{x}_1^{(s)}, \dots, \mathbf{x}_N^{(s)}; \mathbf{x}_1^{(s+1)}, \dots, \mathbf{x}_N^{(s+1)}; \tau_S), \quad (1.10)$$

with  $\tau_S = \beta/S$ ,  $\mathbf{x}_i^{(0)} = \mathbf{x}_i$ , and  $\mathbf{x}_i^{(S)} = \mathbf{x}_{P(i)}$ .

The successive positions  $\mathbf{x}_1^{(0)}, \mathbf{x}_1^{(1)}, \dots, \mathbf{x}_1^{(S)}$  form an object called a *path* (continuous in the limit  $S \rightarrow \infty$ ), indexed by a variable  $\tau = s\tau_S$  called the *imaginary time*. The path integral consists in the sum on all paths performed in Eq. 1.10. In quantum path-integral simulations,  $S$  is finite, and is called the number of imaginary time slices.

Using the Lévy construction (Lévy, 1940), free paths may be sampled directly, which was done in Fig. 1.2, both for a configuration of one boson, and for a configuration of three ideal bosons.

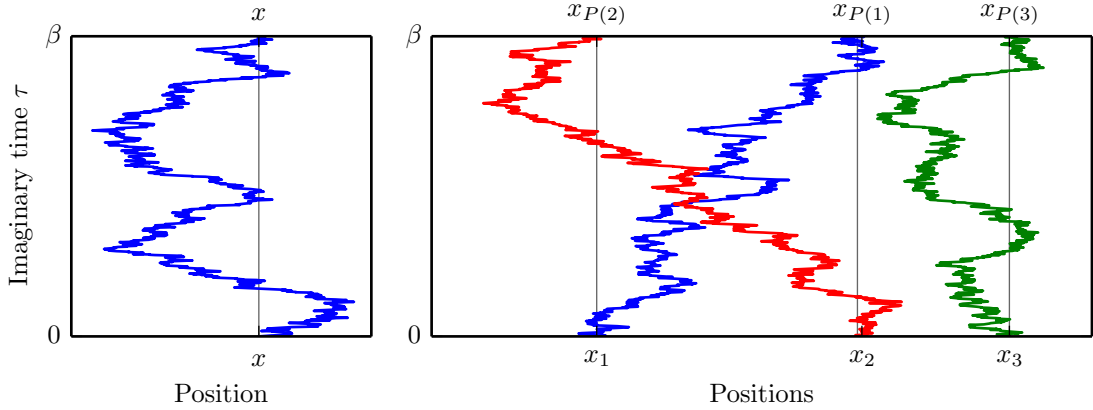


Figure 1.2: Free one-dimensional path configurations for one particle (*left*) and three particles (*right*). In the three-particle configuration, particles 1 and 2 (resp. blue and red) are in the same permutation cycle, while particle 3 (green) is alone in its permutation cycle.

From the free density matrix (1.5), we notice that, at inverse temperature  $\beta$ , the paths of a single boson with  $\mathbf{x}_{P(i)} = \mathbf{x}_i$  span a scale given by the thermal de Broglie wave-length,

$$\lambda_{\text{th}} = \sqrt{\frac{2\pi\hbar^2\beta}{m}}. \quad (1.11)$$

As stated in Section 1.1.1 and illustrated in Fig. 1.1, Bose–Einstein condensation occurs when long permutations become likely. Two bosons  $i$  and  $j$  are likely to be in the same permutation when they are closer than the order of  $\lambda_{\text{th}}$ , so that paths originating in  $\mathbf{x}_i$  and

ending in  $\mathbf{x}_j$  (and reciprocally) are likely to happen. Therefore, Bose–Einstein condensation takes place at a constant value of  $n\lambda_{\text{th}}^3$ , where  $n$  is the particle density. An accurate calculation (Feynman, 1972) yields a critical value  $\lambda_{\text{th}}^{\text{BEC}}$  such that

$$n (\lambda_{\text{th}}^{\text{BEC}})^3 = \zeta(3/2) = 2.612, \quad (1.12)$$

where  $\zeta$  is the Riemann zeta function. The critical value of the thermal de Broglie wavelength  $\lambda_{\text{th}}^{\text{BEC}}$  can be translated into the critical temperature

$$k_B T_{\text{BEC}} = \frac{3.315 \hbar^2}{m} n^{2/3}. \quad (1.13)$$

## 1.2 Interacting Bose gas

So far, I explained how path integrals may provide an interesting description of the Bose–Einstein condensation of ideal bosons. Here, I describe their practical interest in a simulation of interacting bosons. We saw in Eq. 1.4 that the free  $N$ -body density matrix breaks down into a product of (possibly non-diagonal) single-particle density matrix elements. This is not true for interacting particles, whose positions are highly correlated by interactions at low temperature. In fact, it is practically impossible to compute directly the density matrix elements (1.3) for  $N \geq 3$ . In this section, I explain how introducing a finite number of imaginary time slices makes it possible to take into account only the interactions between pairs of particles in a many-body simulation, by using either the Trotter approximation or the pair-product approximation.

In this section, I consider bosons interacting with an interaction operator  $V(\mathbf{x}_1, \dots, \mathbf{x}_N)$ , so that the Hamiltonian is

$$\hat{H} = \hat{H}_{\text{free}} + \hat{V}, \quad (1.14)$$

where  $\hat{H}_{\text{free}}$  was defined in Eq. 1.2. In particular, when only interactions between pairs of bosons are present,  $V(\mathbf{x}_1, \dots, \mathbf{x}_N)$  is defined in terms of the pair interaction  $V(\mathbf{x}_i, \mathbf{x}_j)$  as

$$V(\mathbf{x}_1, \dots, \mathbf{x}_N) = \sum_{i < j} V(\mathbf{x}_i, \mathbf{x}_j). \quad (1.15)$$

### 1.2.1 Trotter approximation

The Trotter formula may be obtained from the general formula for the product of the exponentials of two Hermitian operators  $\hat{X}$  and  $\hat{Y}$ ,

$$e^{\hat{X}} e^{\hat{Y}} = \exp \left( \hat{X} + \hat{Y} + \frac{1}{2} [\hat{X}, \hat{Y}] + \frac{1}{12} [\hat{X}, [\hat{X}, \hat{Y}]] + \frac{1}{12} [[\hat{X}, \hat{Y}], \hat{Y}] + \dots \right), \quad (1.16)$$

where the commutator between any two operators  $\hat{A}$  and  $\hat{B}$  is defined by  $[\hat{A}, \hat{B}] = \hat{A}\hat{B} - \hat{B}\hat{A}$ . Applied to  $-\tau_S \hat{H}_{\text{free}}$  and  $-\tau_S \hat{V}$ , the identity of Eq. 1.16 gives,

$$e^{-\tau_S \hat{H}_{\text{free}}} e^{-\tau_S \hat{V}} = \exp \left( -\tau_S \hat{H} + \frac{\tau_S^2}{2} [\hat{H}_{\text{free}}, \hat{V}] + O(\tau_S^3) \right). \quad (1.17)$$

This in turn yields the Trotter formula (Trotter, 1959), valid for  $\tau_S \rightarrow 0$ ,

$$e^{-\tau_S \hat{H}} = e^{-\tau_S \hat{H}_{\text{free}}} e^{-\tau_S \hat{V}}. \quad (1.18)$$

If  $S$  is large enough that the Trotter formula is valid, by noting that

$$\rho(\mathbf{x}_1^{(s)}, \dots, \mathbf{x}_N^{(s)}; \mathbf{x}_1^{(s+1)}, \dots, \mathbf{x}_N^{(s+1)}; \tau_S) \quad (1.19)$$

$$= \langle \mathbf{x}_1^{(s)}, \dots, \mathbf{x}_N^{(s)} | e^{-\tau_S \hat{H}_{\text{free}}} e^{-\tau_S \hat{V}} | \mathbf{x}_1^{(s+1)}, \dots, \mathbf{x}_N^{(s+1)} \rangle \quad (1.20)$$

$$= e^{-\tau_S V(\mathbf{x}_1^{(s+1)}, \dots, \mathbf{x}_N^{(s+1)})} \rho_{\text{free}}(\mathbf{x}_1^{(s)}, \dots, \mathbf{x}_N^{(s)}; \mathbf{x}_1^{(s+1)}, \dots, \mathbf{x}_N^{(s+1)}; \tau_S), \quad (1.21)$$

the path integral (Eq. 1.10) becomes

$$\rho(\mathbf{x}_1, \dots, \mathbf{x}_N; \mathbf{x}_{P(1)}, \dots, \mathbf{x}_{P(N)}; \beta) \quad (1.22)$$

$$= \int \prod_{s=1}^{S-1} d\mathbf{x}_1^{(s)} \dots d\mathbf{x}_N^{(s)} \exp \left[ -\tau_S \sum_{s=0}^{S-1} V(\mathbf{x}_1^{(s)}, \dots, \mathbf{x}_N^{(s)}) \right] \quad (1.23)$$

$$\times \prod_{s=0}^{S-1} \rho_{\text{free}}(\mathbf{x}_1^{(s)}, \dots, \mathbf{x}_N^{(s)}; \mathbf{x}_1^{(s+1)}, \dots, \mathbf{x}_N^{(s+1)}; \tau_S), \quad (1.24)$$

a result known as the Trotter approximation. This approximation means that, when  $\tau_S$  is small enough, the density matrix of a path with interactions is that of a free path multiplied by the weights of interactions at each imaginary time slice,

$$\exp \left[ -\tau_S \sum_{s=0}^{S-1} V(\mathbf{x}_1^{(s)}, \dots, \mathbf{x}_N^{(s)}) \right]. \quad (1.25)$$

So far, I only stated that  $\tau_S$  has to be very small for the Trotter approximation to hold, which is an imprecise condition. Only two length scales may set the validity of the Trotter approximation: the de Broglie thermal wave-length on one imaginary time slice  $\lambda_S = \lambda_{\text{th}}(\tau_S)$ , and the characteristic length scale of the interaction  $l_V$ . Therefore, a more quantitative condition for the validity of the Trotter approximation is

$$l_V \gg \lambda_S. \quad (1.26)$$

If the interaction  $V(\mathbf{x}_1, \dots, \mathbf{x}_N)$  features pair interactions only, the Trotter approximation means that it is enough to compute interactions slice by slice for pairs of particles only to solve the general problem of  $N$  interacting particles at low temperature. In that case,  $l_V$  is the characteristic length scale of pair interactions.

In a simulation using the Trotter approximation, paths of interacting bosons may be sampled using a direct free path sampling algorithm such as the Lévy construction (see Section 1.1.2), and accepted or rejected using the Metropolis–Hastings procedure (see Section 1.A) based on the weight of interactions in Eq. 1.25.

### 1.2.2 Pair-product approximation

In this section, I consider the case where the interaction between all particles consists in pair interactions only (see Eq. 1.15). In Section 1.1.2, we saw that the paths of free particles span a range  $\lambda_{\text{th}}$ . This is actually a consequence of the Heisenberg uncertainty principle: all particles “occupy” a region of volume  $\sim \lambda_{\text{th}}^3$ . Therefore, the motion of two particles interacting with a short-range potential (that is, whose range is much smaller than  $\lambda_{\text{th}}$ ) will be modified from the free case only if they are at a distance smaller than  $\lambda_{\text{th}}$ .

If we introduce additional time slices, and we consider the interaction on one slice, the scale on which the interaction between two particles cannot be neglected is the de Broglie thermal wave-length on one slice  $\lambda_S = \lambda_{\text{th}}(\tau_S)$ . If  $\lambda_S$  is small enough that  $n\lambda_S^3 \ll 1$ , where  $n$  is the particle density, the event where two particles come closer than  $\lambda_S$  is unlikely, and the event where three particles do even more. Therefore, provided that  $\lambda_S$  is small enough, it is enough to account for the interaction between pairs of particles only. This is the idea of the pair-product approximation, that may formally be written

$$\rho(\mathbf{x}_1, \dots, \mathbf{x}_N; \mathbf{x}'_1, \dots, \mathbf{x}'_N; \tau_S) = \prod_{i=1}^N \rho_{\text{free}}(\mathbf{x}_i, \mathbf{x}'_i; \tau_S) \prod_{i < j}^N \frac{\rho(\mathbf{x}_i, \mathbf{x}_j; \mathbf{x}'_i, \mathbf{x}'_j; \tau_S)}{\rho_{\text{free}}(\mathbf{x}_i, \mathbf{x}'_i; \tau_S) \rho_{\text{free}}(\mathbf{x}_j, \mathbf{x}'_j; \tau_S)}. \quad (1.27)$$

I now discuss Eq. 1.27 to explain why it corresponds to the idea exposed in the above paragraph. On the one hand, when particles  $i$  and  $j$  are farther apart than  $\lambda_S$ , their motion is identical to that of free particles. Therefore, the pair density matrix  $\rho(\mathbf{x}_i, \mathbf{x}_j; \mathbf{x}'_i, \mathbf{x}'_j; \tau_S)$ , that generally describes their correlated probability distribution, breaks down into a product of free density matrices  $\rho_{\text{free}}(\mathbf{x}_i, \mathbf{x}'_i; \tau_S) \rho_{\text{free}}(\mathbf{x}_j, \mathbf{x}'_j; \tau_S)$ . This annihilates the term corresponding to particles  $i$  and  $j$  in the right-hand product. The only term remaining for particles  $i$  and  $j$  consists in their free density matrices  $\rho_{\text{free}}(\mathbf{x}_i, \mathbf{x}'_i; \tau_S) \rho_{\text{free}}(\mathbf{x}_j, \mathbf{x}'_j; \tau_S)$  coming from the left-hand product.

On the other hand, when particles  $i$  and  $j$  are closer than  $\lambda_{\text{th}}$ , because of the hypothesis  $n\lambda_S^3 \ll 1$ , it is extremely unlikely (probability  $\propto n\lambda_S^3$ ) that any of them is closer than  $\lambda_S$  to a third particle. All pair terms involving exclusively either particle  $i$  or  $j$  in the right-hand product therefore annihilate. The only terms involving particles  $i$  and  $j$  that remain in Eq. 1.27 are:

$$\rho_{\text{free}}(\mathbf{x}_i, \mathbf{x}'_i; \tau_S) \rho_{\text{free}}(\mathbf{x}_j, \mathbf{x}'_j; \tau_S) \frac{\rho(\mathbf{x}_i, \mathbf{x}_j; \mathbf{x}'_i, \mathbf{x}'_j; \tau_S)}{\rho_{\text{free}}(\mathbf{x}_i, \mathbf{x}'_i; \tau_S) \rho_{\text{free}}(\mathbf{x}_j, \mathbf{x}'_j; \tau_S)} = \rho(\mathbf{x}_i, \mathbf{x}_j; \mathbf{x}'_i, \mathbf{x}'_j; \tau_S), \quad (1.28)$$

which is the pair density matrix describing the interaction between particles  $i$  and  $j$  in absence of other particles. This indeed corresponds to the above described scenario.

Eq. 1.27 can be enhanced by separating the motion of the centre of mass of particles  $i$  and  $j$  from their relative motion. As the centre of mass is not subject to the interaction, we have:

$$\rho(\mathbf{x}_i, \mathbf{x}_j; \mathbf{x}'_i, \mathbf{x}'_j; \tau_S) = \rho_{\text{free}}^{\text{CM}} \left( \frac{\mathbf{x}_i + \mathbf{x}_j}{2}, \frac{\mathbf{x}'_i + \mathbf{x}'_j}{2}; \tau_S \right) \rho^{\text{relative}}(\mathbf{x}_j - \mathbf{x}_i, \mathbf{x}'_j - \mathbf{x}'_i; \tau_S), \quad (1.29)$$

where  $\rho_{\text{free}}^{\text{CM}}$  is the free density matrix of the centre of mass (of mass  $2m$ ) and  $\rho^{\text{relative}}$  the density matrix of the relative motion (of mass  $m/2$ ). Injecting this identity into the term involving particles  $i$  and  $j$  in the right-hand product of Eq. 1.27, that may be called the correction factor to the free density matrices of particles  $i$  and  $j$ ,  $g(\mathbf{x}_i, \mathbf{x}_j; \mathbf{x}'_i, \mathbf{x}'_j; \tau_S)$ , gives

$$g(\mathbf{x}_i, \mathbf{x}_j; \mathbf{x}'_i, \mathbf{x}'_j; \tau_S) = \frac{\rho(\mathbf{x}_i, \mathbf{x}_j; \mathbf{x}'_i, \mathbf{x}'_j; \tau_S)}{\rho_{\text{free}}(\mathbf{x}_i, \mathbf{x}'_i; \tau_S)\rho_{\text{free}}(\mathbf{x}_j, \mathbf{x}'_j; \tau_S)} = \frac{\rho^{\text{relative}}(\mathbf{x}_j - \mathbf{x}_i, \mathbf{x}'_j - \mathbf{x}'_i; \tau_S)}{\rho_{\text{free}}^{\text{relative}}(\mathbf{x}_j - \mathbf{x}_i, \mathbf{x}'_j - \mathbf{x}'_i; \tau_S)}, \quad (1.30)$$

where  $\rho_{\text{free}}^{\text{relative}}$  is the free relative-motion density matrix.

Thus, the pair-product approximation allows to compute the probability of  $N$ -body configurations by solving the relative-motion problem of two interacting particles and obtaining their relative-motion density matrix  $\rho^{\text{relative}}(\mathbf{x}_j - \mathbf{x}_i; \mathbf{x}'_j - \mathbf{x}'_i; \tau_S)$ . As we will see in Section 2.1.1, the pair correction factor  $g(\mathbf{x}_i, \mathbf{x}_j; \mathbf{x}'_i, \mathbf{x}'_j; \tau_S)$  may be further simplified using the low-temperature  $s$ -wave approximation.

In practice, the implementation of the pair-product approximation in a simulation often consists in generating free paths with the Lévy construction (see Section 1.1.2) and accepting or rejecting them according to the pair correction factors, following the Metropolis–Hastings rule (see Section 1.A). This approximation was originally suggested by Barker (1979), and subsequently used to simulate a variety of bosonic systems including liquid helium (Pollock and Ceperley, 1984) and atomic Bose–Einstein condensates (Krauth, 1996).

So far, the Trotter approximation and the pair-product approximation look quite similar: with a pair interaction, both require to introduce additional time slices to work, and, in both cases, new configurations are generated with a free Lévy construction and accepted or rejected according to an interaction weight (either in Eq. 1.25 or Eq. 1.30). As Bose–Einstein condensates are quite dilute, quite fewer slices are needed for the pair-product approximation ( $n\lambda_S^3 \ll 1$ ) to be valid than for the Trotter approximation ( $\lambda_S \ll l_V$ ).

### 1.2.3 Interaction boxes

In a many-body simulation with a pair interaction only, the use of either the Trotter approximation or of the pair-product approximation would naively require to compute the contribution of each pair of particles. Moving one particle requires to compare its probability at its former position to its probability at its proposed position. Within this naive framework, the complexity of this operation is  $O(N)$ , where  $N$  is the number of particles in the simulation. It is then straightforward that this cannot be used to simulate systems with large  $N$  values, such as  $N \sim 10^6$  (Holzmann and Krauth, 2008).

In practice, if the pair interaction is short-range, it is not necessary to compute the interaction weight of pairs of particles more distant than the effective correction range  $r_{\text{box}}$ , that is, than the distance from which their interaction can be neglected. As we saw,  $r_{\text{box}} \sim \lambda_S$  for the pair-product approximation, and  $r_{\text{box}}$  is the range of the pair interaction potential defined in Eq. 1.15 for the Trotter approximation.

A simple way of taking advantage of this is to use *interaction boxes* (see Fig. 1.3): the three-dimensional space is divided in boxes of constant size  $r_{\text{box}}$ . To know the interaction

weight of a particle, it is enough to compute its interaction weight with particles in the neighbouring boxes only, as it is separated from all other particles by a distance greater than  $r_{\text{box}}$ .

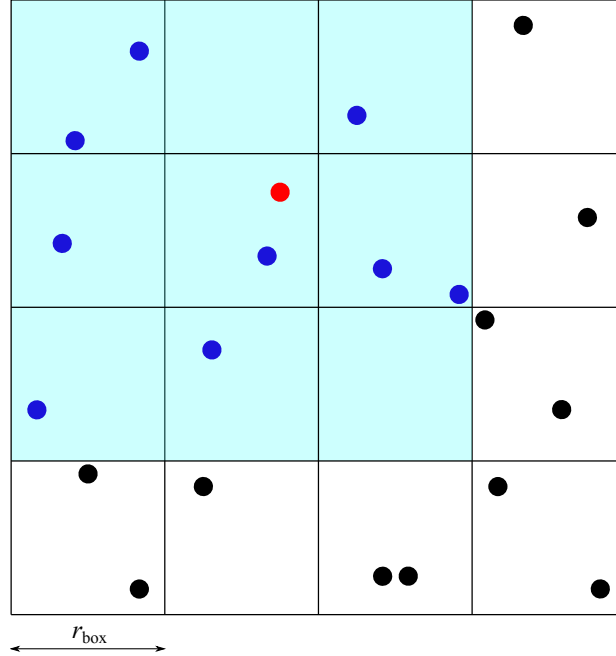


Figure 1.3: Two-dimensional interaction boxes. Space is divided in square boxes whose size is the effective correction range  $r_{\text{box}}$ . In order to compute the interaction weight of interactions involving the red particle, it is enough to compute its interaction only with the blue particles, that are in neighbouring boxes. The size of boxes guarantees that black particles are farther than  $r_{\text{box}}$  from the red particle. Therefore, their interaction with the red particle may be neglected.

With interaction boxes, moving a particle requires to compute the statistical weight due to interactions of particles in neighbouring boxes only, an operation of complexity  $O(1)$ .

## Appendix 1.A Metropolis algorithm

In a generic Markov-chain-driven system, the evolution of the probability  $\pi_t(a)$  of any configuration  $a$  with the time  $t$  is given by the master equation

$$\frac{d\pi_t(a)}{dt} = \sum_b [P(b \rightarrow a)\mathcal{A}(b \rightarrow a)\pi_t(b) - P(a \rightarrow b)\mathcal{A}(a \rightarrow b)\pi_t(a)], \quad (1.31)$$

where the sum runs over all configurations  $b \neq a$ , and the probability of a move from configuration  $a$  to configuration  $b$ , following the common Monte Carlo practice, is split

into two contributions,  $\mathcal{A}(a \rightarrow b)$ , the probability to propose such a move, and  $P(a \rightarrow b)$ , the probability to accept it.

At equilibrium, the probabilities  $\pi_t(b)$  of all configurations  $b$  do not depend on time, and, for the simulation to obtain relevant results, they must be equal to their physical value  $\pi(b)$ . This reads:

$$\sum_b [P(b \rightarrow a)\mathcal{A}(b \rightarrow a)\pi(b) - P(a \rightarrow b)\mathcal{A}(a \rightarrow b)\pi(a)] = 0. \quad (1.32)$$

This equation is called the *global balance* condition, and means that the total probability flux going into configuration  $a$  must be zero at equilibrium. To obtain global balance, it is sufficient to have *detailed balance* for all pairs of configurations  $(a, b)$ , a condition written

$$P(b \rightarrow a)\mathcal{A}(b \rightarrow a)\pi(b) - P(a \rightarrow b)\mathcal{A}(a \rightarrow b)\pi(a) = 0. \quad (1.33)$$

Detailed balance means that the probability flux from a configuration  $a$  to a configuration  $b$  and from configuration  $b$  to configuration  $a$  are equal. While most Markov-chain Monte Carlo simulations use algorithms based on detailed balance, it is worth noting that algorithms that satisfy only global balance are more efficient (Bernard *et al.*, 2009; Michel *et al.*, 2014): detailed balance algorithms explore phase space following a diffusive dynamics while algorithms satisfying global balance only can be considerably faster.

The Metropolis–Hastings algorithm (Metropolis *et al.*, 1953; Hastings, 1970) is a choice for the acceptance probabilities  $P$  that satisfies detailed balance,

$$P(a \rightarrow b) = \min \left[ 1, \frac{\mathcal{A}(b \rightarrow a)\pi(b)}{\mathcal{A}(a \rightarrow b)\pi(a)} \right]. \quad (1.34)$$

The Metropolis–Hastings algorithm is the backbone of the path-integral Monte Carlo algorithm. In practice, the *a priori* configuration update probabilities  $\mathcal{A}(a \rightarrow b)$  consist in proposing the configuration  $b$  using free density matrices only (see Eq. 1.5). The correction to them due to interactions is included in the acceptance probabilities  $P$  following the Metropolis–Hastings rule (Eq. 1.34).

---

## The repulsive weakly-interacting Bose gas

---

In this chapter, I explain how we measured the first corrections to the mean-field equation of state of the weakly-interacting Bose gas, in close collaboration with the Lithium group of Laboratoire Kastler Brossel at École normale supérieure, directed by Christophe Salomon. To this end, I first introduce the concept on which the description of quantum interactions at low temperature takes its roots, the scattering length, and provide a quick review of mean-field results for the weakly-interacting Bose gas. I then describe the first beyond-mean-field corrections to the equation of state, initially predicted in 1957 by [Lee \*et al.\* \(1957\)](#), and how they compare to simulations and experiments. These results correspond to [Publication 1](#).

### 2.1 The mean-field weakly-interacting Bose gas

Before providing a mean-field description of the weakly-interacting Bose gas, it is necessary to introduce the key concept of scattering length, that describes the low-energy collision of particles. As we will see in the first section, the scattering length actually measures the strength of pair interactions.

#### 2.1.1 Scattering length

We saw that, at low densities and in absence of interactions involving three or more particles, the pair-product approximation ensures that the physics of a gas may be described in terms of two-body effects only (see Section [1.2.2](#)). Therefore, the study of the two-body problem is essential to the understanding of Bose–Einstein condensates of mutually-interacting particles. In this section, I review general features of the quantum two-body problem.

### The scattering problem

In quantum physics, the general problem of two particles colliding without affecting their internal structure is described by the *theory of elastic scattering*. The general Schrödinger equation for two such particles, whose interaction is a potential  $V(r)$  that depends only on their separation  $r = \|\mathbf{r}\|$ , and that vanishes at  $r \rightarrow \infty$ , is:

$$\left(-\frac{\hbar^2}{2m} + V(r)\right) \psi(\mathbf{x}_1, \mathbf{x}_2) = E\psi(\mathbf{x}_1, \mathbf{x}_2), \quad (2.1)$$

where  $\mathbf{x}_1$  and  $\mathbf{x}_2$  are the positions of the two particles, and  $\mathbf{r} = \mathbf{x}_2 - \mathbf{x}_1$ .

As with the classical two-body problem, it is possible to separate the motion of the centre of mass from the relative motion of the two particles. The former is that of a free particle of mass  $2m$ , and the relative motion reduces to that of a particle of mass  $m/2$  in the central potential  $V(r)$ :

$$\left(-\frac{\hbar^2}{m} + V(r)\right) \psi(\mathbf{r}) = E\psi(\mathbf{r}). \quad (2.2)$$

As  $V(r) \rightarrow 0$  when  $r \rightarrow \infty$ , *scattering states* (that is, states that are not bound) have a positive energy  $E$ . Let us call  $k$  the corresponding wave-number ( $E = \hbar^2 k^2/m$ ). If we consider an incoming particle moving in the direction  $z$ , at large distances, the general shape of the relative wave-function is the superposition of the incoming plane wave and an outgoing spherical wave  $e^{ikr}/r$ , with a dependence on the *scattering angle*  $\theta$ , that is, the angle between the  $z$  axis and the direction of the scattered particle (see Fig. 2.1) (Landau and Lifshitz, 1981):

$$\psi(r, \theta) \approx e^{ikz} + f_k(\theta) \frac{e^{ikr}}{r}. \quad (2.3)$$

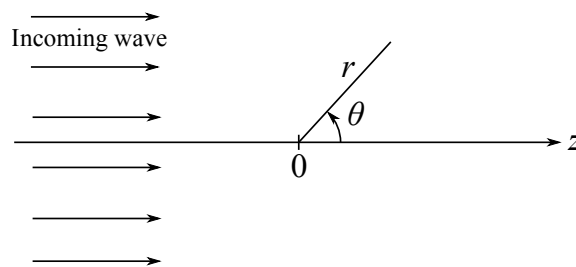


Figure 2.1: The scattering situation: an ongoing harmonic wave along the  $z$  direction is scattered into a spherical wave whose amplitude depends on the angle  $\theta$ .

The *scattering amplitudes*  $f_k(\theta)$  yield the entire physics of the quantum two-body problem. As  $V(r)$  acts only on the radial part of the wave-function, it is possible to expand

$\psi$  on axially symmetric angular momenta of various magnitudes  $l$ :

$$\psi = \sum_{l=0}^{\infty} P_l(\cos \theta) R_{kl}(r), \quad (2.4)$$

where  $P_l$  is the Legendre polynomial of order  $l$ . The Schrödinger equation for the radial wave-function  $R_{kl}$  is then:

$$\left[ -\frac{\hbar^2}{mr^2} \frac{d}{dr} r^2 \frac{d}{dr} + \frac{\hbar^2 l(l+1)}{mr^2} + V(r) - \frac{\hbar^2 k^2}{m} \right] R_{kl}(r) = 0. \quad (2.5)$$

Far from the centre,  $V(r) \approx 0$  and the motion reduces to that of a free particle, yielding a solution of the form

$$R_{kl}(r) \sim j_l(kr) \cos \delta_l(k) - y_l(kr) \sin \delta_l(k), \quad (2.6)$$

where  $j_l$  and  $y_l$  are respectively the spherical Bessel functions of order  $l$  of the first and second kind. The *phase shifts*  $\delta_l(k)$  relate to the interaction between the two particles in the region where  $V(r)$  cannot be neglected. They vanish for free particles. The small- $k$  behaviour of phase shifts  $\tan \delta_l \propto k^{2l+1}$  may be deduced from the behaviour of spherical Bessel functions near  $kr = 0$ .

Phase shifts yield the value of the scattering amplitude (Landau and Lifshitz, 1981):

$$f_k(\theta) = \frac{1}{2ik} \sum_{l=0}^{\infty} (2l+1) (e^{2i\delta_l} - 1) P_l(\cos \theta). \quad (2.7)$$

Additionally, partial scattering amplitudes may be defined at each order  $l$  by  $f_{kl} = (e^{2i\delta_l} - 1)/(2ik)$ . As expected, the partial scattering amplitude of order  $l$  vanishes when interactions are irrelevant at order  $l$  ( $\delta_l = 0$ ).

### The $s$ -wave approximation

If  $r_0$  is the range of the pair interaction  $V$ , we notice that, in Eq. 2.5, if  $kr_0 \ll \sqrt{2}$ , the incoming waves for  $l \geq 1$  cannot reach the region  $r < r_0$  for which  $V(r)$  is non-zero (Cohen-Tannoudji, 1973). In this case, only the  $s$ -waves differ from those of non-interacting particles:  $\delta_l \approx 0$  for all  $l \geq 1$ . The condition  $kr_0 \ll \sqrt{2}$  is realized in two different limits, the *low-temperature limit*  $k \rightarrow 0$ , and the *zero-range limit*  $r_0 \rightarrow 0$ .

The  $s$ -wave approximation, that, consistently with the above, lies in the assumption that  $\delta_l = 0$  for  $l \geq 1$  (valid in either the zero-range or the low-temperature limits), can be used to further simplify the interaction correction factor of the pair-product approximation (see Section 1.2.2). Separating the  $s$ -wave contribution  $\rho_s^{\text{relative}}$  from the rest of the relative-motion density matrix  $\rho^{\text{relative}}$ , the  $s$ -wave approximation yields

$$\rho^{\text{relative}} = \rho_{\text{free}}^{\text{relative}} + \rho_s^{\text{relative}} - \rho_{s,\text{free}}^{\text{relative}}, \quad (2.8)$$

where  $\rho_{s,\text{free}}^{\text{relative}}$  is the  $s$ -wave contribution to the free relative-motion density matrix  $\rho_{\text{free}}^{\text{relative}}$ . In that case, the pair-product approximation correction factor of Eq. 1.30 becomes

$$g(\mathbf{x}_i, \mathbf{x}_j; \mathbf{x}'_i, \mathbf{x}'_j; \tau_S) = 1 + \frac{\rho_s^{\text{relative}}(\mathbf{x}_j - \mathbf{x}_i, \mathbf{x}'_j - \mathbf{x}'_i; \tau_S) - \rho_{s,\text{free}}^{\text{relative}}(\mathbf{x}_j - \mathbf{x}_i, \mathbf{x}'_j - \mathbf{x}'_i; \tau_S)}{\rho_{\text{free}}^{\text{relative}}(\mathbf{x}_j - \mathbf{x}_i, \mathbf{x}'_j - \mathbf{x}'_i; \tau_S)}. \quad (2.9)$$

In our context, the above  $s$ -wave approximation is very useful as, provided that  $\tau_S$  is large enough (a condition sufficient to have  $kr_0 \ll \sqrt{2}$ ), it is enough to compute the  $s$ -wave contribution to the pair density matrix to obtain the pair-product correction factor  $g$ .

### Scattering length

The *scattering length* corresponds to the leading order of the phase shift in  $k$ :

$$a = -\lim_{k \rightarrow 0} \frac{\tan \delta_0(k)}{k}. \quad (2.10)$$

The scattering length is the only length scale describing the low-temperature (or zero-range) behaviour of the quantum two-body system, for which  $k \rightarrow 0$  and higher partial waves with  $l \geq 1$  have zero phase shifts. As a consequence, it is also the only length scale needed to describe the weakly-interacting Bose gas.

Because the scattering amplitude  $f_k(\theta)$  equals  $-a$  at low temperature,  $a$  may be seen as the size on which the incoming wave is modified in Eq. 2.3, and therefore as the effective distance on which particles interact. Hence, the Bose gas is weakly-interacting when its particle density  $n$  is small enough that  $n|a|^3 \ll 1$ .

As at low temperature, the scattering length is the only remaining length scale in the scattering problem, two *a priori* different interaction potentials with the same scattering length yield the same low-temperature physics: simple theoretical models such as quantum hard spheres may be used to describe real low-temperature atomic vapours.

### The quantum hard-sphere interaction

Repulsive ( $a > 0$ ) interactions may be described by the hard-sphere model, in which atoms are simply modelled by spheres that cannot overlap. The corresponding pair interaction is thus given by  $V(r > a) = 0$  and  $V(r < a) = \infty$  (it is possible to show that the radius of hard spheres is half the scattering length  $a$ ). The corresponding  $s$ -wave correction factor to free density matrices is (Holzmann, 2000) (see Section 1.2.2):

$$g_{\text{hs}}(\mathbf{r}, \mathbf{r}'; \tau_S) = \begin{cases} 1 + \frac{\hbar^2 \tau_S}{m} \frac{1}{r r'} \left[ 1 - \exp\left(-m \frac{a^2 - a(r+r')}{\hbar^2 \tau_S}\right) \right] \exp\left(-\frac{m r r' (1 + \cos \gamma)}{2 \hbar^2 \tau_S}\right) & r, r' > a \\ 0 & r < a \text{ or } r' < a, \end{cases} \quad (2.11)$$

where  $\mathbf{r}$  and  $\mathbf{r}'$  are the pair separations at two consecutive imaginary time slices, and  $\gamma$  is the relative angle between vectors  $\mathbf{r}$  and  $\mathbf{r}'$ .

The hard-sphere interaction was successfully used to probe the behaviour of cold-atomic gases at small  $a$  (Krauth, 1996; Holzmann and Krauth, 2008). In the rest of this chapter,

I use a path-integral Monte Carlo algorithm with the hard-sphere interaction to probe the first corrections to the mean-field behaviour of the weakly-interacting Bose gas.

### 2.1.2 Trapped bosons

In this section, I quickly review mean-field results holding for systems of trapped bosons with a small scattering length.

#### Confined gases

In experiments, atomic vapours of alkali gases are typically cooled down to near-zero temperature using a combination of laser and evaporative cooling, and kept confined in a harmonic magneto-optical trap (although geometries closer to the homogeneous gas are currently available (Gaunt *et al.*, 2013)). For the simulation results to be directly comparable to experiments, we need to introduce a confinement potential  $V_{\text{ext}}$ . This corresponds to a Hamiltonian

$$H = \sum_{i=1}^N \left( -\frac{\hbar^2}{2m} \nabla_i^2 + V_{\text{ext}}(\mathbf{x}_i) \right) + \sum_{i < j} V(\mathbf{x}_j - \mathbf{x}_i), \quad (2.12)$$

where  $\mathbf{x}_i$  is the position of particle  $i$ .

#### Mean-field zero-temperature wave-function

The Gross–Pitaevskii equation (Gross, 1961, 1963; Pitaevskii, 1961) governs the wave-function of the condensate  $\phi_0(\mathbf{x})$  in the mean-field approximation:

$$\left( -\frac{\hbar^2 \nabla^2}{2m} + V_{\text{ext}}(\mathbf{x}) + g\phi_0^2(\mathbf{x}) \right) \phi_0(\mathbf{x}) = \mu\phi_0(\mathbf{x}), \quad (2.13)$$

where  $g = 4\pi\hbar^2 a/m$ , and  $\mu$  is the chemical potential. The Gross–Pitaevskii equation is accurate in the weakly-interacting regime  $n|a|^3 \ll 1$ .

Within the mean-field Gross–Pitaevskii approximation, the energy may be expressed as a functional of the particle density  $n(\mathbf{x})$  (Dalfovo *et al.*, 1999):

$$E[n] = \int d\mathbf{x} \left[ -\frac{\hbar^2}{2m} \left| \nabla \sqrt{n(\mathbf{x})} \right|^2 + nV_{\text{ext}}(\mathbf{x}) + \frac{gn^2}{2} \right]. \quad (2.14)$$

In practice,  $n(\mathbf{x})$  is frequently smooth enough for the first term in the integral (called *quantum pressure*) to be neglected. In this case, the gas at position  $\mathbf{x}$  can be considered a homogeneous gas of chemical potential

$$\mu = \mu_0 - V_{\text{ext}}(\mathbf{x}), \quad (2.15)$$

where  $\mu_0$  is the overall chemical potential. This is a particular case of the *local density approximation*.

### Density of a thermal Bose gas within the mean-field approximation

At higher temperature, neglecting the correlations between the positions of thermal, non-condensed particles allows to obtain the following effective Schrödinger equation for the single-particle wave-function  $\phi_T(\mathbf{x})$  of energy  $E$  (Pitaevskii and Stringari, 2003):

$$\left[ -\frac{\hbar^2 \nabla^2}{2m} + V_{\text{ext}}(\mathbf{x}) + 2gn_T(\mathbf{x}) \right] \phi_T(\mathbf{x}) = E\phi_T(\mathbf{x}), \quad (2.16)$$

where  $n_T(\mathbf{x})$  is the density of thermal particles at position  $\mathbf{x}$ .

Solving this equation in momentum space allows to obtain the self-consistent mean-field Hartree–Fock expression of the density (Pitaevskii and Stringari, 2003),

$$n_T(\mathbf{x}) = \frac{1}{\lambda_{\text{th}}^3} g_{3/2} \left( e^{-\beta[V_{\text{ext}}(\mathbf{x}) + 2gn_T(\mathbf{x})] + \beta\mu} \right), \quad (2.17)$$

where  $g_{3/2}$  is the polylogarithm function of order 3/2 defined by

$$g_{3/2}(u) = \sum_{k=1}^{\infty} \frac{u^k}{k^{3/2}}. \quad (2.18)$$

## 2.2 Beyond-mean-field corrections

When  $n|a|^3$  is increased from the value at which the Bose gas is well described by the Gross-Pitaevskii equation, higher-order corrections to the equation of state Eq. 2.14 need to be introduced. In this section, I present these corrections, computed by Lee *et al.* in 1957, and I expose how I tested them jointly with experimentalists using a path-integral simulation.

### 2.2.1 The Lee–Huang–Yang equation of state

#### Canonical equation of state

The mean-field approximations described in the previous section corresponds to neglecting quantum correlations between bosons, which is valid only for small values of the scattering length. Lee, Huang, and Yang (1957) computed the first-order correction to the ground-state mean-field energy of a homogeneous weakly-interacting Bose gas  $E/V = gn^2/2$  ( $V$  is the volume occupied by the gas). They found

$$\frac{E}{V} = \frac{gn^2}{2} \left( 1 + \frac{128}{15\sqrt{\pi}} \sqrt{na^3} \right). \quad (2.19)$$

At this order, this equation of state still depends only on  $a$ . However, non-universal terms, that are connected to the large- $a$  physics exposed in the following chapters, appear at higher orders of  $na^3$  (Braaten *et al.*, 2002).

The only parameters on which this equation of state depends are  $\hbar$ ,  $m$ , and  $a$ . Therefore, the equation of state  $\tilde{E}(\tilde{n})$  expressed in terms of the dimensionless energy  $\tilde{E} = E/(\hbar^2/(ma^2))$  and density  $\tilde{n} = na^3$  is universal as it no longer depends on the interactions (even through  $a$ ).

### Grand-canonical Lee–Huang–Yang equation of state

Although the energy  $E$  may be accessed in Monte Carlo simulations (Ceperley, 1995), it is very hard to access it in experiments. It is however possible to deduce a grand-canonical zero-temperature equation of state  $P(\mu)$  from Eq. 2.19 by using the thermodynamic identities

$$\begin{cases} \mu(n) = \frac{\partial E}{\partial N} = \frac{\partial(E/V)}{\partial n}, \\ P = n\mu(n) - \frac{E}{V}. \end{cases} \quad (2.20)$$

Like for the canonical Lee–Huang–Yang equation (Eq. 2.19), this equation of state may be cast into a dimensionless form that does not depend on  $a$  by defining the dimensionless variables  $\tilde{\mu} = \mu/(\hbar^2/(ma^2))$  and  $\tilde{P} = P/(\hbar^2/(ma^5))$ . This dimensionless grand-canonical equation of state is plotted on Fig. 2.2 along with its mean-field equivalent  $\tilde{P} = \tilde{\mu}^2/(8\pi)$ .

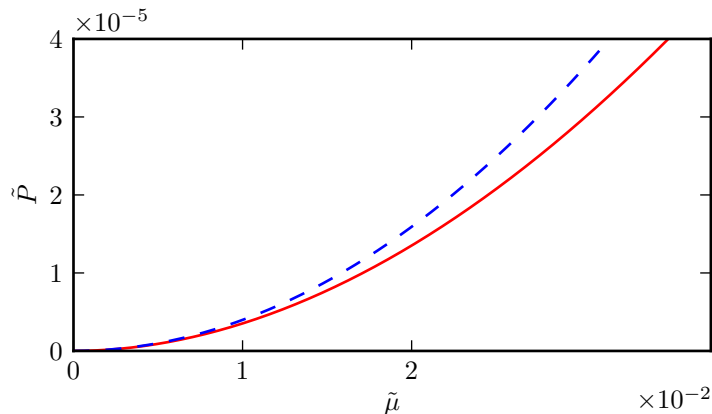


Figure 2.2: Grand-canonical version of the Lee–Huang–Yang equation (*solid red line*, see Eq. 2.20), together with its mean-field equivalent  $\tilde{P} = \tilde{\mu}^2/(8\pi)$  (*dashed blue line*). We see that for small values of  $\tilde{\mu}$ , and therefore of  $\tilde{n}$ , the mean-field equation holds well and is practically identical to the Lee–Huang–Yang equation. For higher values of  $\tilde{\mu}$ , however, the Lee–Huang–Yang equation clearly departs from the mean-field equation.

### 2.2.2 Path-integral simulation and comparison to experiments

To test the grand-canonical Lee–Huang–Yang equation (Eq. 2.20), we built up a simulation based on the hard-sphere interaction (Eq. 2.11), that both provided a numerical grand-

canonical equation of state of the interacting Bose gas and allowed to check that the equation of state obtained in experiments probes the zero-temperature regime, in which the Lee-Huang–Yang equation is valid. In this section, I describe the experimental set-up used by Christophe Salomon’s group at Laboratoire Kastler Brossel, our quantum path-integral Monte Carlo simulation, and compare their results.

### Experimental set-up and need for a simulation

The experiment of Christophe Salomon’s group at Laboratoire Kastler Brossel consists in atoms of  ${}^7\text{Li}$  cooled down and trapped in a magneto-optical trap. They can measure the density of atoms in the trap by direct *in-situ* imaging. Because imaging projects the cloud onto one direction of space, the image that they obtain corresponds to a two-dimensional atomic density distribution  $n_{2d}(x, y)$ .

In the experiment, this density distribution is the only accessible observable. At high temperature, the density distribution of non-condensed atoms explicitly depends on the temperature, and may be used to probe it. However, at temperatures much lower than the that of Bose–Einstein condensation, most atoms are in the Bose–Einstein condensate, and the temperature cannot be accessed directly in the experiment. Measuring the temperature is however a prerequisite for properly testing the Lee–Huang–Yang equation (Eq. 2.20): before any quantitative check, it is necessary to make sure that the zero-temperature assumption is correct.

In path-integral Monte Carlo simulations, however, the temperature comes as a parameter (see Chapter 1). Therefore, it is possible to deduce the validity of the zero-temperature assumption from the comparison of experiments to numerical simulations, whose temperature is well-known.

### Monte Carlo simulation

In order to provide such a Monte Carlo simulation, I built up a new simulation based on that of Krauth (1996). The use of the Python programming language considerably simplified the former Fortran 77 code, and, because the essential routines were compiled using Cython, this did not lead to a significant slow-down of the simulation.

The algorithm itself, using the hard-core bosons interaction potential in the pair-product approximation (see Section 2.1.1), was slightly altered from that of Krauth (1996) to make it work at the large values of  $a$  probing the Lee–Huang–Yang regime, but its general principles were kept unchanged.

With this simulation, we were able to probe the physics of a system of 39 000 bosons at  $a/a_0 = 2150$ , where  $a_0$  is the Bohr radius, in an axially-symmetric trap of frequencies  $\omega_z = 2\pi \times 18.5$  Hz,  $\omega_\perp = \omega_x = \omega_y = 2\pi \times 345$  Hz, which corresponds to the experimental trap. This simulation was run down to temperatures as small as  $T = 0.125T_{\text{BEC}}^{\text{trap}}$ , where  $T_{\text{BEC}}^{\text{trap}}$  is the temperature at which a Bose–Einstein condensate appears at the centre of the trap for non-interacting bosons (Dalfovo *et al.*, 1999),

$$T_{\text{BEC}}^{\text{trap}} = 0.94\hbar\omega_{\text{ho}}N^{1/3}, \quad (2.21)$$

where  $\omega_{\text{ho}} = (\omega_z \omega_{\perp}^2)^{1/3}$  is the geometric average of the trap frequencies. At such low temperatures, the simulations had to be run for up to two weeks on eight independent processors to reduce the statistical error.

### Assessment of the zero-temperature approximation

In order to compare our simulations to the experimental data, we used the doubly-integrated density profile,

$$\bar{n}(z) = \int dx dy n(x, y, z), \quad (2.22)$$

where  $n(\mathbf{x} = (x, y, z))$  is the particle density in the trap.

The doubly-integrated density profile may be obtained numerically by ensemble averaging independent configurations of the Monte Carlo simulation, or experimentally by integrating the *in situ* absorption image. On Fig. 2.3, the numerical density profiles at several temperatures are shown together with the average of several experimental images. The experimental data seems to correspond to the numerical data for temperatures smaller than  $T = 0.25T_{\text{BEC}}^{\text{trap}}$ .

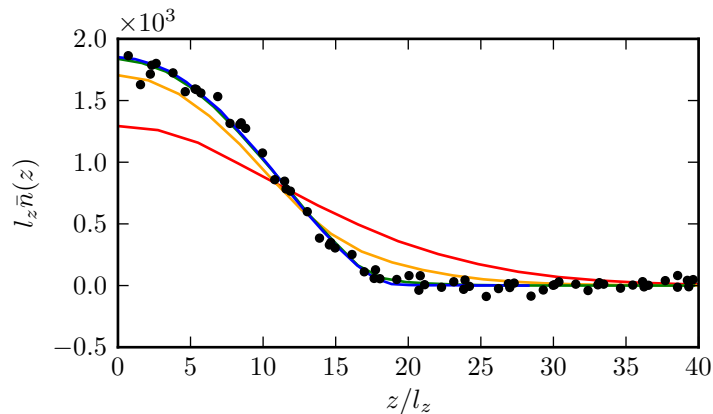


Figure 2.3: Doubly-integrated numerical density profiles at  $T/T_{\text{BEC}}^{\text{trap}} = 0.75$  (red), 0.5 (orange), 0.25 (green), and 0.125 (blue), together with the experimental average of several density profiles (black points). Lengths are expressed in units of the  $z$ -axis trap length  $l_z = \sqrt{\hbar/m\omega_z}$ . The experimental data agrees well with the numerical data at  $T_{\text{BEC}}^{\text{trap}} = 0.25$  and 0.125.

This agreement between the numerical and experimental data may be measured more quantitatively using a  $\chi^2$  test. As shown on Fig. 2.4, the numerical and experimental data agree for temperatures lower than  $T = 0.25T_{\text{BEC}}^{\text{trap}}$ . Since it is also hard to distinguish between the numerical data at  $T/T_{\text{BEC}}^{\text{trap}} = 0.25$  and 0.125 (see Fig. 2.3), this shows that the experiment is indeed probing a Bose gas in the zero-temperature assumption.

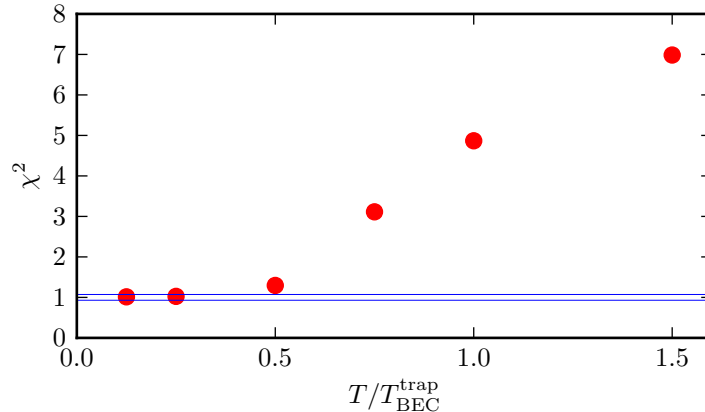


Figure 2.4: Chi-squared test values comparing experimental doubly-integrated density profiles to the numerical data at various temperature (*red points*). The two blue horizontal lines denote the interval of likely values of the  $\chi^2$  test if the experimental and numerical data match.

### 2.2.3 Numerical and experimental grand-canonical equation of state

We just saw that the experiment and simulations indeed probe the zero-temperature physics of the Bose gas. Here, I explain how we retrieved the grand-canonical equation of state from the numerical and experimental density profiles, and how these numerical and experimental equations of state compare to the Lee–Huang–Yang grand-canonical equation of state (Eq. 2.20).

#### Pressure and doubly-integrated density profile

As explained for the Gross–Pitaevskii equation of state (see Section 2.1.2), within the local density approximation, the subsystem at position  $\mathbf{x}$  of an inhomogeneous system of overall chemical potential  $\mu_0$  in a trapping potential  $V_{\text{ext}}$  may be considered a homogeneous system at chemical potential  $\mu_0 - V_{\text{ext}}(\mathbf{x})$  at the price of neglecting all terms involving density gradients.

Within the local-density approximation, by integrating out the  $x$  and  $y$  axes, we may define the chemical potential along the  $z$ -axis by

$$\mu(z) = \mu_0 - \frac{1}{2}m\omega_z^2 z^2. \quad (2.23)$$

The pressure is then related to the doubly-integrated density profile as

$$P(\mu(z)) = \frac{m\omega_z^2}{2\pi} \bar{n}(z). \quad (2.24)$$

This relation can be obtained by integrating the Gibbs–Duhem equation  $dP = nd\mu + sdT$  at fixed temperature (Ho and Zhou, 2010). Thus, the grand-canonical equation of state

can be extracted from the doubly-integrated density profile at the price of estimating the overall chemical potential  $\mu_0$ .

### Comparison with the Lee–Huang–Yang expansion

Using Eq. 2.23 and 2.24, it is possible to compare both the experimental and numerical data to the grand-canonical Lee–Huang–Yang equation of state. For the experimental data, the value of  $\mu_0$  was obtained from an iterative scheme based on trial density distributions (see Publication 1). For the numerical data, it was obtained from a fit of the wings of the doubly-integrated density profile to the corresponding doubly-integrated mean-field density distribution, obtained from Eq. 2.17 within the local density approximation Eq. 2.15.

As shown on Fig. 2.5, the agreement between the Lee–Huang–Yang equation of state and both the numerical and the experimental data is very good.

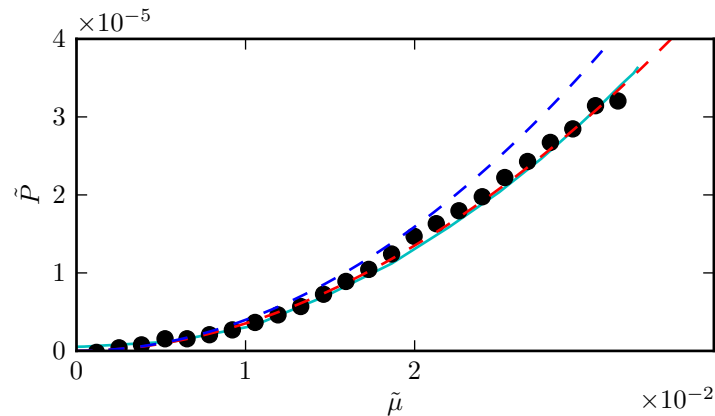


Figure 2.5: Grand-canonical equation of state obtained experimentally (*black points*) and numerically at  $T/T_c = 0.25$  (*plain cyan line*), compared to the zero-temperature mean-field dimensionless pressure  $\tilde{P} = \tilde{\mu}^2/(8\pi)$  (*dashed blue line*), and to the grand-canonical Lee–Huang–Yang equation of state (*dashed red line*). The experimental data is an average of several experimental samples.

## 2.3 Conclusion

In this chapter, I showed that a quantum path-integral Monte Carlo simulation with hard-sphere pair interactions quantitatively reproduces the behaviour of a gas of weakly-interacting bosons, with the access to more observables than in experiments, and in particular to the temperature. Along with the experimental data, this simulation allowed to validate the Lee–Huang–Yang equation (Eq. 2.19), that describes the first corrections to the mean-field equation of state of the weakly-interacting Bose gas.



---

## Efimov trimers in the path-integral formalism

---

At unitarity, when the scattering length becomes much larger than any other length scale, although no pair of particles can bind, three particles can form a infinity of three-body bound states called *Efimov trimers*. The properties of these trimer states are universal, in that they depend on the short-range details of the interactions only through an overall scaling factor.

The Efimov effect was initially discovered in the 1970s in nuclear physics (Efimov, 1970, 1971, 1979). Subsequently, it was discussed in various domains such as quantum magnets (Nishida *et al.*, 2013) or the biophysics of DNA (Maji *et al.*, 2010), and, more importantly, in cold-atoms experiments, where Feshbach resonances (Chin *et al.*, 2010) allow to tune the scattering length to unitarity. There, they have been observed through the decay of the near-unitary Bose gas into deeply-bound states (Kraemer *et al.*, 2006; Zaccanti *et al.*, 2009; Pollack *et al.*, 2009). Stable Efimov trimers, however, remain elusive in experiments.

Although Efimov trimers have been very well characterized theoretically (Braaten and Hammer, 2006), descriptions of the Efimov effect in terms of path integrals are scarce (Maji *et al.*, 2010). In this chapter, after having explained in details the unitary limit for two bosons and presented a model interaction potential, I provide a path-integral description of the Efimov effect based on semi-quantitative considerations and I describe a numerical simulation of three bosons that matches theoretical predictions. This chapter corresponds to the three-body physics described in [Publication 2](#).

### 3.1 Unitary limit

In this section, I first illustrate the unitary limit of pair interactions through the square-well interaction potential. I then describe another interaction potential more suited for numerical simulations, the zero-range unitary potential, and, most importantly, derive the

corresponding pair-product correction factor (see Section 1.2.2).

### 3.1.1 Square-well interaction potential

Let us consider the square-well interaction potential  $V_{\text{SW}}$ , given as a function of the interparticle distance  $r$  by:

$$V_{\text{SW}}(r) = \begin{cases} -V_0 & 0 < r < r_0, \\ 0 & r > r_0, \end{cases} \quad (3.1)$$

where  $r_0$  is the range of the potential and  $V_0$  its depth. The square-well interaction potential is depicted in Fig. 3.1.

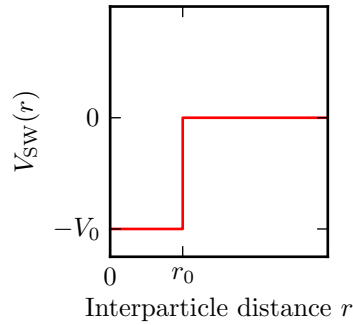


Figure 3.1: Square-well interaction potential of depth  $V_0$  and range  $r_0$ .

The Schrödinger equation for the radial wave-function is given by Eq. 2.5. If we restrict to  $s$ -waves ( $l = 0$ ),  $\chi(r) = R_{ks}(r)r$  obeys the Schrödinger equation of a free particle in the potential  $V_{\text{SW}}(r)$ :

$$-\frac{\hbar^2}{m}\chi'' + V_{\text{SW}}(r)\chi = E\chi. \quad (3.2)$$

#### Scattering length

Let us determine the scattering length associated to the square-well potential. For this, we need to compute the phase shift  $\delta_s(k)$  defined in Eq. 2.6. The Schrödinger equation for a diffusive state of energy  $\hbar^2 k^2/m$  is

$$\begin{cases} \frac{\hbar^2}{m}\chi''(r) + \left(V_0 + \frac{\hbar^2}{m}k^2\right)\chi = 0 & 0 < r < r_0 \\ \chi''(r) + k^2\chi = 0 & r > r_0, \end{cases} \quad (3.3)$$

so that

$$\begin{cases} \chi(r) = A \sin\left(r\sqrt{\frac{V_0 m}{\hbar^2} + k^2}\right) & 0 \leq r \leq r_0 \\ \chi(r) = B \sin(kr + \delta_s(k)) & r \geq r_0. \end{cases} \quad (3.4)$$

The continuity of the logarithmic derivative of the wave-function yields

$$\delta_s = -kr_0 + \arctan \left( k \frac{\tan \left( r_0 \sqrt{V_0 m / \hbar^2 + k^2} \right)}{\sqrt{V_0 m / \hbar^2 + k^2}} \right). \quad (3.5)$$

Applying Eq. 2.10 to the above value of  $\delta_s$  gives

$$a = -\lim_{k \rightarrow 0} \frac{\delta_s}{k} = r_0 \left( 1 - \frac{\tan(r_0 \sqrt{V_0 m / \hbar^2})}{r_0 \sqrt{V_0 m / \hbar^2}} \right). \quad (3.6)$$

Contrary to the hard-sphere interaction described in Section 2.1.1, for which the scattering length, that may be identified to the diameter of the hard spheres, has to be positive and finite, the scattering length of the square-well interaction may be either positive or negative, and is even infinite for  $r_0 \sqrt{V_0 m / \hbar^2} = \pi/2$ .

This situation, where the scattering length is infinite, or much larger than all other length scales, is called *unitarity*. In the next section, I describe how the bound state of the square-well interaction potential behaves through the unitary region.

### Bound states of the square-well interaction potential

Let us now consider bound states of small negative energy  $-E_D \ll V_0$ . The Schrödinger equation for such states is

$$\begin{cases} \frac{\hbar^2}{m} \chi'' + V_0 \chi = 0 & 0 < r < r_0 \\ \frac{\hbar^2}{m} \chi'' - E_D \chi = 0 & r > r_0, \end{cases} \quad (3.7)$$

which yields solutions of the form

$$\begin{cases} \chi = A \sin \left( r \sqrt{V_0 m / \hbar^2} \right) & 0 < r < r_0 \\ \chi = B \exp \left( -r \sqrt{E_D m / \hbar^2} \right) & r > r_0, \end{cases} \quad (3.8)$$

where  $A$  and  $B$  are two constants.

When  $r_0 \sqrt{V_0 m / \hbar^2} \geq \pi/2$ , the continuity of the logarithmic derivative of the wave-function yields

$$E_D = \frac{\sqrt{V_0}}{\tan^2 \left( r_0 \sqrt{V_0 m / \hbar^2} \right)} = \frac{\hbar^2}{m(a - r_0)^2}. \quad (3.9)$$

On the contrary, when  $r_0 \sqrt{V_0 m / \hbar^2} < \pi/2$ , there is no solution: at unitarity, the dimer state is at the threshold of its existence. This result may be qualitatively obtained by a reasoning based on path integrals (see Section 3.A). The extension of the dimer,  $\sqrt{\hbar^2 / (m E_D)}$ , is equal to  $a$  when  $a \gg r_0$ . This, and that the dimer vanishes with zero energy at unitarity, are

known results for any interaction potential in the limit  $a \gg r_0$  (Braaten and Hammer, 2006).

By considering  $s$ -waves of small energy only, we omitted both other possible bound states associated to higher partial waves ( $l \geq 1$ ) and  $s$ -wave bound states with a large binding energy. These anyway do not exist when the interaction potential, such as that considered, has only one  $s$ -wave bound state with a small binding energy. These omitted states, called *deeply-bound states*, exist in general and make Efimov trimers hard to observe in experiments (Braaten and Hammer, 2006). This is why we restrict to a regime in which the square-well potential does not feature any deeply-bound state.

### 3.1.2 Zero-range interaction potential

#### Scaling limit

To eliminate finite-range effects, that depend on the chosen interaction potential, we study the limit  $r_0 \rightarrow 0$  at fixed  $a$ , called the *scaling* or *zero-range limit* (Braaten and Hammer, 2006), illustrated in Fig. 3.2.

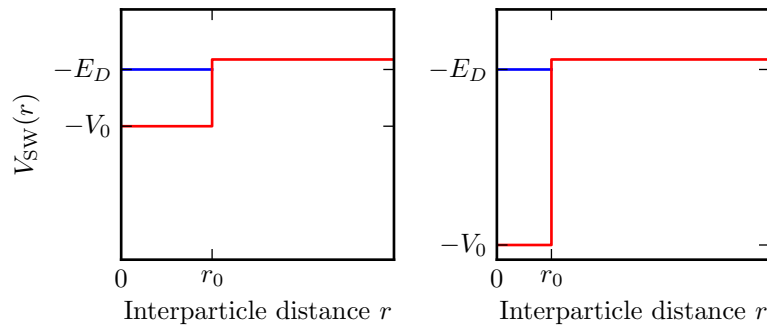


Figure 3.2: The left and right panel show square-well interaction potentials with the same scattering length (and therefore with approximately the same dimer state binding energy). The right-hand potential has a smaller range  $r_0$  and is therefore closer to the zero-range limit  $r_0 \rightarrow 0$  and  $V_0 \rightarrow \infty$ .

In the zero-range limit, for positive values of  $a$ ,

$$E_D = \hbar^2/ma^2, \quad (3.10)$$

and the condition of validity of the  $s$ -wave approximation,  $kr_0 \ll \sqrt{2}$ , where  $k$  is the wave-number of partial waves, is fulfilled at all temperatures (see Section 2.1.1).

### Bethe–Peierls boundary condition

In the scaling limit,  $\delta_s(k) = -\arctan(ka)$ , so that the normalized radial wave-function  $\chi$  is given by (see Eq. 3.4)

$$\chi(r) = \sqrt{\frac{2}{\pi}} \sin(kr - \arctan(ka)), \quad (3.11)$$

or alternatively

$$R_{ks}(r) = \frac{\chi(r)}{r} = \sqrt{\frac{2}{\pi}} \frac{\sin(kr - \arctan(ka))}{r}. \quad (3.12)$$

The only remainder of the square-well interaction in the  $r < r_0$  region is a boundary condition on  $R_{ks}$ , that holds also for the total wave-function  $\psi$ ,

$$\psi \xrightarrow{r \rightarrow 0} C \left( \frac{1}{r} - \frac{1}{a} \right). \quad (3.13)$$

For  $R_{ks}$ , we find  $C = (\sqrt{2/\pi})ka/\sqrt{1+k^2a^2}$ . This limit condition is called the Bethe–Peierls boundary condition (Bethe and Peierls, 1935a,b), and can be taken, together with the equations of free motion for  $r > 0$ , as a definition of the zero-range interaction potential (Braaten and Hammer, 2006).

### Pair-product correction factor for the zero-range interaction

The Trotter approximation (see Section 1.2.1) is not suited to simulate particles that interact with the zero-range interaction, since the corresponding interaction potential is zero unless both particles are at the same position.

As the pair-product approximation is based on the full quantum solution of the two-body problem (see Section 1.2.2), it is suited in a simulation of particles interacting with the zero-range potential. The corresponding pair-product correction factor is therefore essential to any simulation featuring the zero-range interaction potential. I found its value to be (see Section 3.B for the detailed calculation):

$$g(\mathbf{r}, \mathbf{r}'; \tau_S; a) = 1 + \frac{2\tau_S \hbar^2}{mrr'} \left[ 1 + \frac{\hbar \sqrt{\pi \tau_S}}{ma} e^{\left( \frac{r+r'}{2\hbar} \sqrt{\frac{m}{\tau_S}} - \frac{\hbar}{a} \sqrt{\frac{\tau_S}{m}} \right)^2} \operatorname{erfc} \left( \frac{r+r'}{2\hbar} \sqrt{\frac{m}{\tau_S}} - \frac{\hbar}{a} \sqrt{\frac{\tau_S}{m}} \right) \right] \quad (3.14)$$

$$\times \exp \left[ -\frac{mrr'(1 + \cos \gamma)}{2\tau_S \hbar^2} \right], \quad (3.15)$$

where  $\gamma$  is the relative angle between  $\mathbf{r}$  and  $\mathbf{r}'$ . At unitarity, only the infinite- $a$  version of the above formula is used,

$$g_\infty(\mathbf{r}, \mathbf{r}'; \tau_S) = 1 + \frac{2\tau_S \hbar^2}{mrr'} \exp \left[ -\frac{mrr'(1 + \cos \gamma)}{2\tau_S \hbar^2} \right]. \quad (3.16)$$

## 3.2 Efimov effect

As we saw in the previous section, in absence of deeply-bound dimer states, at unitarity, two particles cannot bind. In this section, I describe how adding a third particle results in an infinity of bound trimer states, a surprising result known as the Efimov effect. To this end, I first explain why the zero-range interaction potential needs to be regularized at short three-body distances, and I then describe Efimov physics in the path-integral formalism both through theoretical arguments and a numerical simulation.

### 3.2.1 Regularization of the zero-range interaction potential

When three particles interact only *via* the zero-range unitary potential, the total density matrix features a singularity at short three-body distances. This phenomenon, called the *Thomas collapse* (Thomas, 1935), may be overcome by a three-body short-range regularization.

#### Thomas collapse

Let us consider three distinguishable identical particles, mutually interacting with the zero-range potential, at very high temperature. For distances higher than the de Broglie thermal wave-length  $\lambda_{\text{th}}$  (that may be set to an arbitrarily small value by increasing the temperature), the total interaction correction factor of a configuration will be, within the pair-product approximation (see Section 1.2.2):

$$g(\mathbf{r}_{12}, \mathbf{r}_{12}; \beta)g(\mathbf{r}_{23}, \mathbf{r}_{23}; \beta)g(\mathbf{r}_{31}, \mathbf{r}_{31}; \beta), \quad (3.17)$$

where  $\mathbf{r}_{ij}$  denotes the separation between particles  $i$  and  $j$ . Therefore, if we concentrate on terms that cause the strongest divergence when the distances are very small, from Eq. 3.16, the total statistical weight  $w$  of such a configuration will behave as

$$w \sim \frac{1}{r_{12}^2 r_{23}^2 r_{31}^2}. \quad (3.18)$$

All other terms are either non-divergent or more regular.

Using Jacobi coordinates (see Section 3.C), the positions of all particles may be expressed in terms of that of the centre of mass  $\mathbf{r}_{\text{CM}}$ , whose motion is independent of the inter-particle interactions, and two relative-motion vectors,  $\mathbf{r}_{12}$  and  $\mathbf{r}_{3,12} = \mathbf{x}_3 - (\mathbf{x}_1 + \mathbf{x}_2)$ . The pair separations  $\mathbf{r}_{23}$  and  $\mathbf{r}_{31}$  may be expressed in terms of  $\mathbf{r}_{12}$  and  $\mathbf{r}_{3,12}$  as

$$\begin{cases} \mathbf{r}_{23} = \mathbf{r}_{3,12} - \frac{1}{2}\mathbf{r}_{12}, \\ \mathbf{r}_{31} = -\mathbf{r}_{3,12} - \frac{1}{2}\mathbf{r}_{12}. \end{cases} \quad (3.19)$$

Thus, Eq. 3.18 may be rewritten as

$$w \sim \frac{1}{r_{12}^2 \left(\mathbf{r}_{3,12} - \frac{1}{2}\mathbf{r}_{12}\right)^2 \left(\mathbf{r}_{3,12} + \frac{1}{2}\mathbf{r}_{12}\right)^2}. \quad (3.20)$$

In particular, we have:

$$\int w d^3 \mathbf{r}_{12} \sim \frac{1}{r_{3,12}^3}. \quad (3.21)$$

In three-dimensional space,  $1/r_{3,12}^3$  is clearly non-integrable: the zero-range potential features a non-integrable singularity when all three particles are very close one to another.

As the pair-product approximation is valid only when particles are typically farther than the de Broglie thermal wave-length  $\lambda_{\text{th}}$  (see Section 1.2.2), this calculation actually has no meaning when all three particles are at a distance smaller than  $\lambda_{\text{th}}$  from one another. Instead, the singularity causes all three particles to fall into a bound state with interparticle distances at most of order  $\lambda_{\text{th}}$ , which goes to zero at infinite temperature. Since three particles interacting with a zero-range pair potential collapse into the identified singularity at high temperature, they also do at all lower temperatures, as decreasing thermal energy makes it harder for particles to leave a bound state.

Although we used distinguishable particles in this reasoning, this singularity also exists for indistinguishable bosons as permutations leave the leading divergence term of Eq. 3.20 unchanged. As a consequence, the zero-range interaction potential needs a short-distance regularization to be physically meaningful when more than three particles are involved.

### Three-body hard core

As the zero-range interaction potential is pathological for more than two bosons, we need to introduce a small three-body distances regularization. This may be done by adding a three-body hard-core to our model, for example by imposing a bound on the hyperradius (or root-mean-square distance)  $R$ :

$$R^2 = \frac{1}{3}(r_{12}^2 + r_{23}^2 + r_{31}^2). \quad (3.22)$$

We define the three-body hard core potential  $V_3$  by a hyperradial cutoff  $R_0$ :

$$V_3(R) = \begin{cases} 0 & R > R_0, \\ \infty & R \leq R_0. \end{cases} \quad (3.23)$$

The short-distances regularized Hamiltonian that we use to study the system of three indistinguishable bosons of mass  $m$  is therefore

$$H = \frac{-\hbar^2}{2m} (\nabla_1^2 + \nabla_2^2 + \nabla_3^2) + V_2(r_{12}) + V_2(r_{23}) + V_2(r_{31}) + V_3(R), \quad (3.24)$$

where  $V_2$  is the zero-range unitary pair interaction.

### 3.2.2 Path-integral argument

In the former section, we saw that in absence of a regularization, three bosons will collapse into a state of infinitely negative energy and zero extension for all values of  $a$ , although

there is no pair bound state at unitarity (and for  $a < 0$ ). It is thus reasonable to expect that with the three-body hard-core regularization, the same kind of effective interaction as that leading to the Thomas collapse will induce the existence of a three-body bound state, a surprising situation known as the *Efimov effect*. In this section, I use the path-integral formalism to give qualitative arguments for the emergence of three-body bound states at unitarity.

### Simple path-integral model

As we saw in Section 3.1.1, at unitarity, in absence of deeply-bound states, two particles never bind. Let us consider two bosons at a distance  $r$ , interacting *via* a unitary interaction potential. We add a *third* boson whose scattering length  $a$  with the two former ones is *large, finite and positive*, and we look for the condition under which this third boson stabilizes the system into a bound state. This situation, depicted in Fig. 3.3, is identical to that studied in Maji *et al.* (2010), although my arguments are based on the statistical weights of configurations, not on scaling considerations.

For practical reasons, we use the square-well finite-range potential of Section 3.1.1 with a range  $r_0$  much smaller than all other length scales. As the energy is bounded by  $-3V_0$ , this potential has the advantage of featuring no three-body collapse. However, we shall keep in mind that the limit  $r_0 \rightarrow 0$  (at fixed scattering length) should be taken only together with a short-distance regularization such as the three-body hard core discussed in Section 3.2.1.

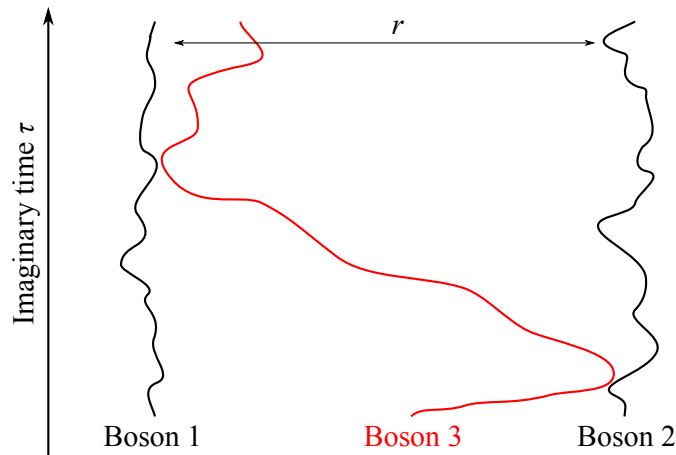


Figure 3.3: Simple qualitative path-integral model. Bosons 1 and 2 are kept at a distance  $r$ . We study the statistical weights of class 1 configurations, where boson 3 keeps scattering between boson 1 and 2 (as depicted), and class 2 configurations, where boson 3 forms a dimer with either boson 1 or boson 2.

### Weights of configurations

We consider two different classes of configurations:

- In class 1, boson 3 keeps scattering between bosons 1 and 2 (this situation is depicted in Fig. 3.3).
- In class 2, boson 3 forms a stable dimer with either boson 1 or boson 2.

In absence of any three-body effect, with a positive scattering length  $a$ , the most likely configurations are in class 2, where two particles form a dimer of extension  $a$  (see Section 3.1.1). If class 1 paths are more likely, the three particles spontaneously form trimer states.

Class 2 paths consist in paths that are close to boson 1 (or 2) and that are allowed to scatter to a distance  $a$  before coming back. This process takes place for an imaginary time  $\tau_a$  of order such that  $\lambda_{\text{th}}(\tau_a) = a$ . For  $\tau_a$ , we may approximate the statistical weight of such paths by that of free paths originating and ending at the same position (one close to either boson 1 or boson 2),  $\rho_{\text{free}}(0, 0; \beta)$ , multiplied by the volume  $\mathcal{V}_0$  in which this position may be chosen and an interaction weight  $w_{\text{int}}$ . The volume  $\mathcal{V}_0$  corresponds to positions where the interaction energy is non-zero, that is, to the volume inside the interaction square well:

$$\mathcal{V}_0 = \frac{4\pi}{3} r_0^3. \quad (3.25)$$

The interaction weight is

$$w_{\text{int}} = e^{\tau_{r_0} V_0}, \quad (3.26)$$

where  $\tau_{r_0}$  is the imaginary time typically spent in the interaction square well (a simple estimate is  $\tau_{r_0}$  such that  $\lambda_{\text{th}}(\tau_{r_0}) = r_0$ ). Thus, keeping in mind that the possibility to bind with either boson 1 or 2 produces a multiplicative factor 2, and using the expression of the free density matrix of Eq. 1.5, the total weight of class 2 configurations is

$$w_2 = 2w_{\text{int}}\rho_{\text{free}}(0, 0; \tau_a)\mathcal{V}_0 = \frac{8\pi}{3} r_0^3 \frac{e^{\tau_{r_0} V_0}}{\lambda_{\text{th}}^3(\tau_a)}. \quad (3.27)$$

In the same fashion, for the imaginary time  $\tau_r$  such that  $\lambda_{\text{th}}(\tau_r) = r$ , the paths in class 1 scatter between bosons 1 and 2. Bearing in mind that boson 3 may scatter either from boson 1 to boson 2, or from boson 2 to boson 1, which here also produces a factor 2, we obtain the total weight of class 1 configurations,

$$\tilde{w}_1 = 2w_{\text{int}}\rho_{\text{free}}(0, r; \tau_r)\mathcal{V}_0 = \frac{8\pi}{3} r_0^3 \frac{e^{\tau_{r_0} V_0}}{\lambda_{\text{th}}^3(\tau_r)} e^{-mr^2/(2\hbar^2\tau_r)}. \quad (3.28)$$

In order to compare the total weights of class 1 and class 2 configurations properly, we need to consider these weights for the same imaginary time. For the imaginary time  $\tau_a$ , the statistical weight of class 1 configurations where boson 3 is initially close to boson 1

is  $(\tilde{w}_1/2)^{a^2/r^2}$ , and is identical to that of class 1 configurations where boson 3 is initially close to boson 2. Thus, the weight of class 1 configuration for the imaginary time  $\tau_a$  is

$$w_1 = 2 \left( \frac{\tilde{w}_1}{2} \right)^{\tau_a/\tau_r} = 2 \left( \frac{\tilde{w}_1}{2} \right)^{a^2/r^2}. \quad (3.29)$$

The condition for class 1 configurations to dominate over class 2 configurations is

$$w_1 \gg w_2. \quad (3.30)$$

Eliminating pure numerical factors including  $\tau_{r_0} V_0$ , that remains constant at fixed  $a$  (see Section 3.1.1), this condition may be rewritten

$$\frac{1}{r^2} \ln \frac{r_0}{r} \gg \frac{1}{a^2} \ln \frac{r_0}{a}. \quad (3.31)$$

As  $x \mapsto (1/x^2) \ln(1/x)$  is a decreasing function, this condition is ensured provided that

$$a \gg r. \quad (3.32)$$

Thus, when  $a$  is so much greater than  $r_0$  that it is possible to introduce an additional length scale  $r$  so that  $r_0 \ll r \ll a$ , a three-body bound state with one boson scattering between the two other bosons (which corresponds to a class 1 state) is more stable than a free boson and a dimer (which corresponds to a class 2 state). This is a first description of the Efimov effect: when  $a$  is much greater than all other length scales, three bosons form a trimer. At unitarity, and for  $a < 0$ , Efimov trimers are Borromean states, in that they form a three-body bound state although two particles cannot bind. The condition for their existence,

$$|a| \gg r_0, \quad (3.33)$$

is achieved in both the unitary ( $a \rightarrow \pm\infty$ ) and scaling ( $r_0 \rightarrow 0$ ) limits. In the case of the zero-range interaction potential with a hyperradial cutoff  $R_0$ , the condition  $|a| \gg r_0$  may be replaced by  $|a| \gg R_0$ . This mechanism, in which a third boson stabilizes two otherwise non-bound bosons by scattering between them, is the hallmark of the Efimov effect (Efimov, 1979).

### 3.2.3 Numerical simulation of a single Efimov trimer

In this section, I describe how the path-integral Monte Carlo algorithm can be adapted to the case of three particles interacting with the zero-range potential regularized with the three-body hard core. I then present some of the results that were discussed in [Publication 2](#).

### Compression-dilation move

We saw that the zero-range unitary potential causes the pair wave-function to obey the Bethe–Peierls boundary condition (see Eq. 3.13) and diverge as  $1/r$  when  $r \rightarrow 0$ . In consequence, the pair density matrix of the relative motion (that we deduce from Eq. 3.16 and Eq. 1.5) diverges as  $1/r r'$ :

$$\rho^{\text{relative}}(\mathbf{r}, \mathbf{r}'; \beta) = \left( \frac{m}{4\pi\hbar^2\beta} \right)^{3/2} \exp \left[ -\frac{m(\mathbf{r} - \mathbf{r}')^2}{4\hbar^2\beta} \right] \left\{ 1 + \frac{2\beta\hbar^2}{mrr'} \exp \left[ -\frac{mrr'(1 + \cos\gamma)}{2\beta\hbar^2} \right] \right\}. \quad (3.34)$$

In particular, the interaction weight of a single slice  $s$  diverges as  $1/(r^{(s)})^2$  at  $r^{(s)} \rightarrow 0$ , where  $r^{(s)}$  is the pair separation at slice  $s$ :

$$w(r^{(s)}) \propto \rho^{\text{relative}}(\mathbf{r}^{(s-1)}, \mathbf{r}^{(s)}; \tau_S) \rho^{\text{relative}}(\mathbf{r}^{(s)}, \mathbf{r}^{(s+1)}; \tau_S) \underset{r^{(s)} \rightarrow 0}{\sim} \frac{1}{(r^{(s)})^2}. \quad (3.35)$$

In usual path-integral Monte Carlo simulations (Krauth, 1996, 2006), new configurations are sampled using the free density matrix, and accepted or rejected following the Metropolis–Hastings rule applied to the additional weight due to the interactions (see Section 1.A). Because the free density matrix has no divergence at small values of  $r^{(s)}$  (see Eq. 1.5), usual Monte Carlo updates will typically propose new configurations  $r^{(s)} + \Delta$ , where  $\Delta$  is a constant that does not depend on  $r^{(s)}$ . If  $r^{(s)}$  is very small,  $r^{(s)} + \Delta$  will be such that  $w(r^{(s)} + \Delta) \ll w(r^{(s)})$ , which leads to near-zero acceptance rates. In order to overcome this, I devised a new Monte Carlo update, the *compression-dilation move*, illustrated in Fig. 3.4. It consists in proposing a new configuration where the separation of two nearby particles at a slice  $s$  has been multiplied (*dilation*) or divided (*compression*) by a factor  $1 + h$ , while keeping their centre of mass in place and not altering other particles nor other slices. If  $h$  is small, the weight of the proposed new configuration may be expressed through a Taylor series expansion:

$$w(r^{(s)}(1 \pm h)) = w(r^{(s)}) \pm hr^{(s)}w'(r^{(s)}), \quad (3.36)$$

and, because  $w'(r^{(s)}) \sim 1/(r^{(s)})^3$  when  $r^{(s)} \rightarrow 0$ , the interaction weight of the new proposed configuration is of the same order as  $w(r^{(s)})$ . Therefore, this new move has high acceptance rates, and successfully samples the  $r^{(s)} \rightarrow 0$  region.

Two additional facts must be taken into account for compression-dilation moves to satisfy detailed balance (see Section 1.A):

- Compression-dilation moves need to be micro-reversible, that is, for each compression move, the inverse dilation move must be allowed, and *vice versa*.
- Dilation moves affect phase space by sending a volume  $d\mathbf{r}^{(s)}$  to a volume  $(1 + h)^3 d\mathbf{r}^{(s)}$ , and compression moves  $d\mathbf{r}^{(s)}$  to  $d\mathbf{r}^{(s)}/(1 + h)^3$ .

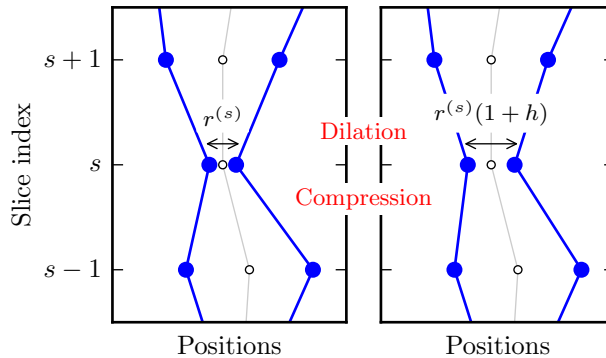


Figure 3.4: Compression-dilation move. Positions (*blue dots*) are kept in place at all slices but slice  $s$ , where, from an initial pair separation  $r^{(s)}$ , the proposed new configuration has a pair separation  $r^{(s)}(1+h)$  in the case of a dilation move. The compression move consists in the inverse move. The centres of mass (*white dots*) are kept in place at all slices.

If we always proposed a compression or a dilation regardless of the initial pair separation  $r^{(s)}$ , there would be no concern for the micro-reversibility of compression-dilation moves. However, there is no need to propose compression-dilation moves at large inter-particle distances, where  $w(r^{(s)})$  is regular: this would be a waste of resources. Therefore, we wish to set an upper bound on the pair distances from which we propose compressions or dilations. We also would like a compression and the corresponding inverse dilation to be proposed with equal probability.

Let us define  $r_c^{\max}$  as largest pair distance from which we propose a compression move. The algorithm used in the simulation is shown in Fig. 3.5. It sets the *a priori* probabilities  $\mathcal{A}(r \rightarrow r^{(s)}(1+h))$  and  $\mathcal{A}(r^{(s)}(1+h) \rightarrow r^{(s)})$  to be equal (see Section 1.A for the definition of  $\mathcal{A}$ ).

We noted that the compression-dilation move also affects phase space by compressing (or dilating) the volume element  $d\mathbf{r}^{(s)}$ . In fact, the volume elements have to be taken into account in the detailed balance equation (see Eq. 1.33), that therefore reads:

$$P(r^{(s)} \rightarrow r^{(s)}(1+h)) \pi(r^{(s)}) d\mathbf{r}^{(s)} = P(r^{(s)}(1+h) \rightarrow r^{(s)}) \pi(r^{(s)}(1+h)) d[(1+h)\mathbf{r}^{(s)}] \quad (3.37)$$

$$= P(r^{(s)}(1+h) \rightarrow r^{(s)}) \pi(r^{(s)}(1+h)) (1+h)^3 d\mathbf{r}^{(s)}. \quad (3.38)$$

Thus, when using the Metropolis–Hastings rule for accepting or rejecting the proposed updates,  $\pi(r^{(s)}(1+h))$  must be formally replaced by  $(1+h)^3 \pi(r^{(s)}(1+h))$  in Eq. 1.34.

### Compression-dilation of nearest neighbours only

The compression-dilation move described in the above paragraph could directly be used in a simulation. We already saw that it is not worth trying to perform compression-dilation

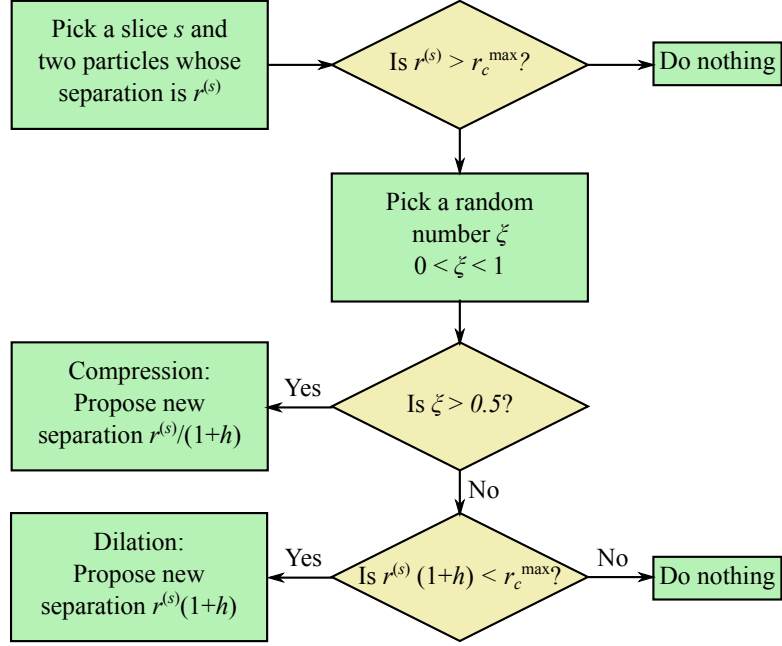


Figure 3.5: Compression-dilation algorithm used in the simulations. This algorithm ensures the micro-reversibility of the Monte Carlo moves.

moves for two particles far away from one another, hence the upper bound  $r_c^{\max}$  from which compression moves are proposed. In fact, it is even more efficient to try to perform the compression-dilation move at a slice  $s$  for nearest neighbours only. In the program, this is done by picking a first boson randomly, and then by picking its nearest neighbour as the boson with which to perform the compression-dilation move. However, for the move to be reversible, we need to make sure that, after the compression-dilation move, the two picked bosons will still be nearest neighbours.

The three-body hard-core condition makes that, if particles are closer than  $R_0/\sqrt{2}$ , they are nearest neighbours. Let us consider two particles, with a pair distance  $\mathbf{r}_{12}$ , and a third particle whose distance with the second one is  $\mathbf{r}_{23}$ . The three-body hard core condition is

$$r_{12}^2 + r_{23}^2 + (\mathbf{r}_{12} + \mathbf{r}_{23})^2 \geq 3R_0^2, \quad (3.39)$$

or

$$r_{23}^2 + r_{12}r_{23} \cos \gamma + r_{12}^2 - \frac{3}{2}R_0^2 \geq 0, \quad (3.40)$$

where  $\gamma$  is the relative angle between vectors  $\mathbf{r}_{12}$  and  $\mathbf{r}_{23}$ . We would like to see how the value of  $r_{12}$  sets a bound on  $r_{23}$ , therefore we take  $r_{23}$  as a variable. The left-hand side of Eq. 3.40 is a polynomial that is positive for values of  $r_{23}$  lower than its smaller root, and higher than its larger root. If  $r_{12} \leq \sqrt{3/2}R_0$ , which we take as an assumption because we are interested in small separations  $r_{12}$ , there are a positive and a negative root, and,

because  $r_{23}$  is positive, it is greater than the positive root:

$$r_{23} \geq \frac{1}{2} \left( -r_{12} \cos \gamma + \sqrt{r_{12}^2 \cos^2 \gamma + 6R_0^2 - 4r_{12}^2} \right). \quad (3.41)$$

The right-hand side of this inequality is a decreasing function of  $\cos \gamma$ . Therefore, it is sufficient to have

$$r_{23} \geq \frac{1}{2} \left( -r_{12} + \sqrt{6R_0^2 - 3r_{12}^2} \right). \quad (3.42)$$

This is the lower bound on  $r_{23}$ , given a value of  $r_{12} \leq \sqrt{3/2}R_0$ . Therefore, in order to have  $r_{23} \geq r_{12}$ , it is enough to have

$$\frac{1}{2} \left( -r_{12} + \sqrt{6R_0^2 - 3r_{12}^2} \right) \geq r_{12}, \quad (3.43)$$

that is,

$$r_{12} \leq \frac{R_0}{\sqrt{2}}. \quad (3.44)$$

In order to be sure that bosons 1 and 2 are nearest neighbours before and after the compression-dilation move, we must therefore make sure that we do not propose a dilation to a distance larger than  $R_0/\sqrt{2}$ . This corresponds to the largest acceptable value of the pair distance from which we propose a compression move,  $r_c^{\max}$ , that was defined in the above paragraph.

### Efficiency of the compression-dilation move

In order to numerically show that the compression-dilation samples the  $1/r^2$ -diverging pair distribution function efficiently, I simulated two interacting bosons on the same permutation cycle. At inverse temperature  $\beta$ , their pair separation distribution is  $\rho^{\text{relative}}(\mathbf{r}, -\mathbf{r}; \beta)$ , where  $\rho^{\text{relative}}$  is given by Eq. 3.34. As is shown in Fig. 3.6, the path-integral Monte Carlo algorithm with the compression-dilation move succeeds in sampling that distribution.

The compression-dilation move is one of the many ways of successfully sampling  $\rho^{\text{relative}}$ . This algorithm could be improved by including stochastic compression-dilation moves affecting several slices at a time or by using moves that reconstruct paths on several slices in the  $r \rightarrow 0$  region by direct sampling of  $\rho^{\text{relative}}$ .

### Simulation on a single permutation cycle

At finite temperature, in infinite space, entropic effects make that, even in presence of a bound state, three particles are always far apart from one another. Therefore, to simulate a single Efimov trimer, it is necessary to regulate the volume. Simple choices of volume regulation include the use of a (possibly periodic) box, or of a harmonic trap whose characteristic length is much larger than the size of the studied Efimov trimer. Going with

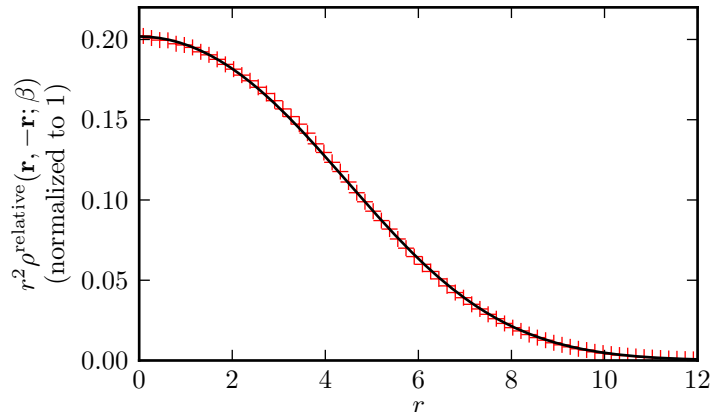


Figure 3.6: Pair distribution function for two unitary bosons on the same permutation cycle, with  $\beta/\tau_S = 100$ . The numerical results (*red crosses*) are compared with the analytical formula of Eq. 3.34 (*black line*), the good agreement showing that the compression-dilation move succeeds in sampling that distribution.

any of these two choices requires a cautious assessment of their finite-size effects on Efimov trimers.

The path-integral structure of Efimov trimers, that we already described to some extent in Section 3.2.2, may also be used to regulate the volume. In Efimov trimers, all three bosons come very close one to another at some imaginary time, which is due to the divergence of the pair correlation function following the Bethe–Peierls boundary condition (see Eq. 3.13). Let us look at the contribution of two close bosons to the statistical weight of two consecutive slices  $s-1$  and  $s$ . In the pair-product approximation (see Section 1.2.2), the joint weight of slices  $s-1$  and  $s$  may be written

$$w^{(s-1,s)} = g_\infty(\mathbf{r}^{(s-1)}, \mathbf{r}^{(s)}; \tau_S) w_{\text{reg}}, \quad (3.45)$$

where  $w_{\text{reg}}$  is the regular part of the joint weight of slices  $s-1$  and  $s$ , which consists in the free contributions of all three particles, and depends on their positions at slices  $s-1$  and  $s$ , that are not written explicitly,  $g_\infty$  is the pair-product correction factor at unitarity (see Eq. 3.16), and  $\mathbf{r}^{(s)}$  is the separation of the two bosons, that we label 1 and 2 in the following, at slice  $s$ .

We would like to see what the change in  $w^{(s-1,s)}$  is when the positions of the two bosons  $\mathbf{x}_1^{(s)}$  and  $\mathbf{x}_2^{(s)}$  at slice  $s$  and above are swapped. This corresponds to a single-slice permutation move, that may be used in path-integral Monte Carlo simulations to sample permutations (Krauth, 2006) (see Fig. 3.7). The single-slice permutation move changes the statistical weight on one slice only.

From Eq. 1.5, we know that the free contribution to  $w^{(s-1,s)}$  is unchanged with such a move if  $r^{(s-1)}, r^{(s)} \ll \lambda_S$ , where  $\lambda_S = \lambda_{\text{th}}(\tau_S)$  is the thermal de Broglie wavelength on one slice. Within the same condition, the unitary pair-product correction factor  $g_\infty$

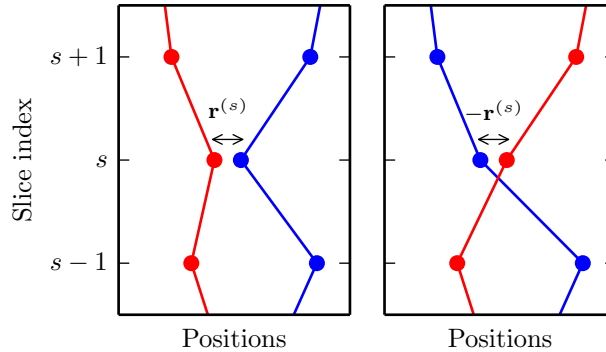


Figure 3.7: Single-slice permutation move. The positions of the red and blue bosons are swapped at slice  $s$ , and the path at above slices is kept in place, resulting in a change of the particle it describes. Only the statistical weight of the paths between slices  $s - 1$  and  $s$  is changed, since the signs of all separations at slices above  $s$  are changed, and the positions at slices below  $s - 1$  are all unchanged.

is also invariant under the permutation  $\mathbf{r}^{(s)} \mapsto -\mathbf{r}^{(s)}$  (see Eq. 3.16). As stated above, in Efimov trimers, pairs of particles come very close one to another, so that the condition  $r^{(s-1)}, r^{(s)} \ll \lambda_S$  is true at some slice for each pair of bosons. At these slices, permutations may therefore be sampled at no statistical cost. This means that the physical properties of Efimov trimers do not depend on the permutation.

In the following, I describe a path-integral Monte Carlo simulation of three unitary bosons on the same permutation cycle, which regulates the available volume at a size  $\sim \lambda_{\text{th}}^3$  with no finite-size effect: the simulation will probe the fundamental Efimov trimer for temperatures  $k_B T$  smaller than its binding energy. As shown in the following of this chapter, this simulation reproduces exactly known results about Efimov trimers. It was presented in [Publication 2](#).

### Simulation of an Efimov trimer

In order to simulate an Efimov trimer using three co-cyclic bosons, as explained above, I used a path-integral Monte Carlo algorithm with the compression-dilation algorithm. Because of the  $1/r^2$  divergence of the pair correlation function, paths in Efimov trimers differ significantly from free paths, and for the Trotter approximation (used for the three-body hard core, see Section 1.2.1) to be valid, quite a large number of slices are necessary to get to temperatures smaller than the binding energy of Efimov trimers. In practice, simulations went as far as  $S = 10\,240$  slices. Starting from a free co-cyclic configuration, it takes a very long time to make a simulation with such a large number of slices converge to an Efimov trimer. To experience smaller convergence times, the initial configuration of the simulation at inverse temperature  $2\beta$  was built from the final configuration of a converged simulation at inverse temperature  $\beta$ . Using this method, 32 independent simulations were

run at each temperature for up to two days.

As we may see on Fig. 3.8, the distribution of hyperradii  $R$  (defined in Eq. 3.22) of the three bosons evolves when  $\beta$  is increased, and finally stabilizes at very low temperatures  $\beta\hbar^2/(mR_0^2) \sim 10^3$ . This is a sign that, at such a temperature, the system is probing its fundamental Efimov trimer state.

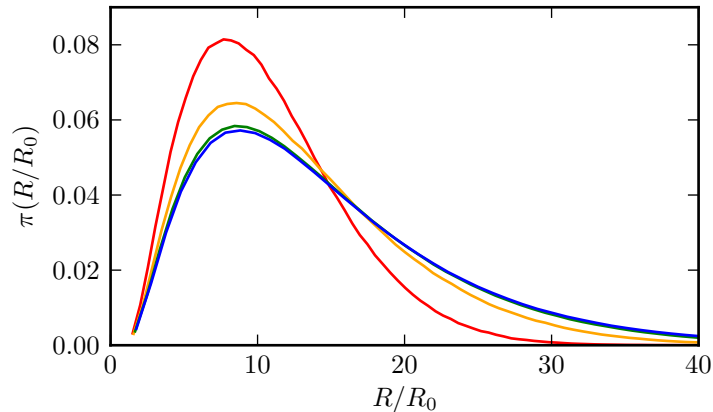


Figure 3.8: Evolution of the hyperradial distribution  $\pi(R)$  as a function of  $\beta$ :  $\beta\hbar^2/(mR_0^2) = 200$  (*red*), 400 (*orange*), 800 (*green*), 1600 (*blue*). The imaginary time slice  $\tau_S$  is kept at the value  $0.1mR_0^2/\hbar^2$ . These distributions are ensemble averages over thermalized configurations. (The value of  $R_0$  was adjusted from its input value using the known universal physics of Efimov states, as discussed in Section 3.2.4.)

Looking at a single snapshot of paths for three unitary interacting bosons (see central panel in Fig. 3.9) shows that the simple argument of Section 3.2.2 takes its roots in a good intuition of Efimov trimers: in an Efimov trimer, at a given imaginary time, only two of the three bosons may be close one to another, but bosons keep changing interaction partners. As we derived the analytical formula for the pair-product correction factor  $g$  also for finite values of  $a$ , I also obtained snapshots of three co-cyclic non-bound particles for  $a/R_0 \sim -1$  (Fig. 3.9, left panel), and a single atom together with a dimer state for  $a/R_0 \sim 1$  (Fig. 3.9, right panel), consistently with the two-body theory described in Section 3.1. The last configuration ( $a/R_0 \sim 1$ ) could not be obtained with the compression-dilation algorithm only, as, with this algorithm, it is impossible to untie two bosons that are close on a very long imaginary time. Starting from a free configuration, at very low temperatures, different pairs of bosons come very close at different imaginary times, resulting in a situation where all pairs of bosons form tightly-bound states at different imaginary times. The depicted configuration, that maximises entropy, and where the same pair of bosons is bound throughout the imaginary time, was therefore obtained by repetitively annealing configurations where only two bosons were close.

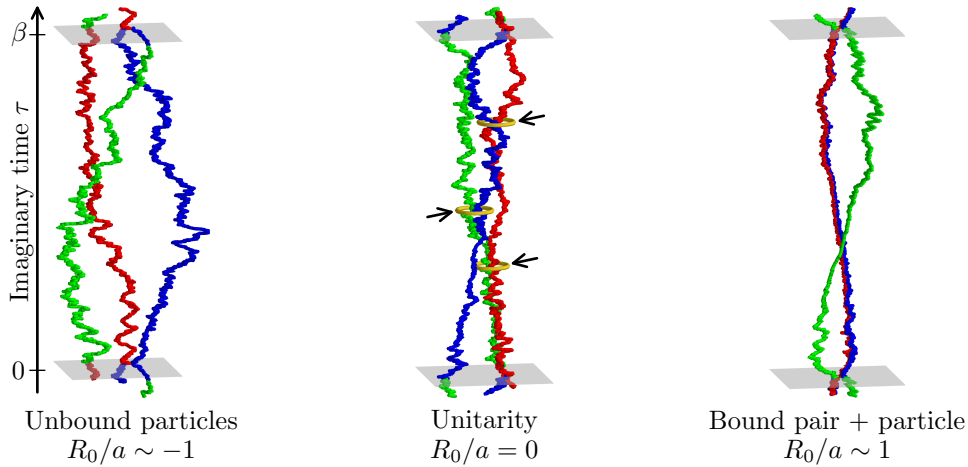


Figure 3.9: Single snapshots of configurations of three co-cyclic bosons. *Left* ( $R_0/a \sim -1$ ): the three bosons do not bind and typical pair distances are given by  $\lambda_{\text{th}}$ . *Centre* ( $R_0/a = 0$ , unitarity): the three bosons form an Efimov trimer, where, in turn, all pairs of bosons are close and the third boson is far from them (yellow highlights and arrows). *Right* ( $R_0/a \sim 1$ ): two of the three bosons bind into a dimer state. These snapshots were obtained at  $\beta\hbar^2/(mR_0^2) = 1045$  with  $S = 2560$ .

### 3.2.4 Universality of Efimov trimers

In the previous section, I described the Efimov effect and, using both theoretical arguments and a simulation, I showed how it surprisingly can bind three bosons in a situation where two bosons cannot bind. However, this description leaves out an essential feature of the Efimov effect: its universal nature, in the sense that Efimov trimers do not depend on the shape of the interactions. In this section, I review a few of the known results on universal Efimov trimers, and show that the Efimov trimers obtained in our three-body simulation are universal.

#### Excited Efimov trimers

In this section, I follow mostly the calculations of Braaten and Hammer (2006), with the addition of the three-body hard core potential  $V_3(R)$ . In hyperspherical coordinates (see Section 3.C), after having eliminated the motion of the centre of mass, the Hamiltonian of Eq. 3.24 may be recast into the form

$$H^{\text{relative}} = T_R + T_{\alpha_k} + \frac{\Lambda_{k,ij}}{2mR^2} + V(R, \Omega), \quad (3.46)$$

where  $i, j, k$  refer to bosons 1, 2, 3 in any order,  $V(R, \Omega)$  is the sum of the zero-range unitary pair interactions and the hyperradial cutoff  $V_3$ ,  $T_R$  the kinetic energy associated to

the hyperradius  $R$ ,  $T_{\alpha_k}$  to the Delves hyperangle

$$\alpha_k = \arctan \frac{\sqrt{3}r_{ij}}{2r_{k,ij}}, \quad (3.47)$$

where  $\mathbf{r}_{ij}$  and  $\mathbf{r}_{k,ij}$  were defined in Section 3.2.1,  $\Lambda_{k,ij}$  denotes the generalized angular momentum operator of  $\mathbf{r}_{ij}$  and  $\mathbf{r}_{k,ij}$ , and  $\Omega$  collectively denotes  $\alpha_k$  and the other hyperangles that describe the orientation of  $\mathbf{r}_{ij}$  and  $\mathbf{r}_{k,ij}$  (see Section 3.C for details on the hyperspherical coordinates  $(R, \Omega)$ ).

In the following, as we wish to describe the low-energy behaviour of Efimov trimers, we consider only the zero generalized angular momentum sector, which means that the wave-function depends only on  $r_{ij}$  and  $r_{k,ij}$ , or equivalently on  $R$  and  $\alpha_k$ .

We saw that Efimov trimers are a superposition of states where two bosons are very close one to another and the third is very far from them (see Section 3.2.2 and 3.2.3). Mathematically, this can be expressed through the *Faddeev approximation* for the total wave-function  $\Psi$  (Faddeev, 1960):

$$\Psi(\mathbf{x}_1, \mathbf{x}_2, \mathbf{x}_3) = \psi(r_{23}, r_{1,23}) + \psi(r_{31}, r_{2,31}) + \psi(r_{12}, r_{3,12}). \quad (3.48)$$

The wave-function  $\psi(r_{ij}, r_{k,ij}) = \psi(R, \alpha_k)$  describes the correlation between the (close) particles  $i$  and  $j$  and the (distant) particle  $k$ , and is assumed to satisfy the Faddeev equations, that add up to the Schrödinger equation associated to  $H^{\text{relative}}$ ,

$$(T_R + T_{\alpha_1} + V_3(R))\psi(R, \alpha_1) + V_2(r_{23})(\psi(R, \alpha_1) + \psi(R, \alpha_2) + \psi(R, \alpha_3)) = E\psi(R, \alpha_1), \quad (3.49)$$

the two other Faddeev equations consisting in the circular permutations of the indices  $(1, 2, 3)$  in the above equation.

At unitarity, the Faddeev equations may be solved using the hyperspherical expansion

$$\psi(R, \alpha) = \frac{1}{R^{5/2} \sin(2\alpha)} \sum_n f_n(R) \phi_n(R, \alpha), \quad (3.50)$$

where  $n$  is a channel index. For the lowest-energy channel, it is possible to show that the hyperradial wave-function  $f_0(R)$  satisfies the hyperradial Schrödinger equation

$$\left[ \frac{\hbar^2}{2m} \left( -\frac{d^2}{dR^2} - \frac{s_0^2 + 1/4}{R^2} \right) + V_3(R) \right] f_0(R) = E f_0(R), \quad (3.51)$$

where  $s_0 \approx 1.00624$  (Braaten and Hammer, 2006). In this equation, the pair interaction has been replaced by the lowest-energy channel effective potential

$$V_0 = -\frac{\hbar^2}{2m} \frac{s_0 + 1/4}{R^2}, \quad (3.52)$$

by integrating the angular wave-function  $\phi_0(R, \alpha)$  out.

The general solution of this equation that vanishes at  $R \rightarrow \infty$  is, for  $R \geq R_0$ ,

$$f_0(R) = R^{1/2} K_{is_0}(\sqrt{2}\kappa R), \quad (3.53)$$

where  $K_{is_0}$  is the modified Bessel function of the second kind of imaginary index  $is_0$  and  $\kappa$  is the binding wave-number of the bound state, given by

$$E_T = \frac{\hbar^2 \kappa^2}{m}. \quad (3.54)$$

The value of  $\kappa$  is determined by the hyperradial cutoff  $R_0$ , that imposes  $K_{is_0}(\sqrt{2}\kappa R_0) = 0$ . When  $\kappa R_0 \ll 1$ , this condition may be rewritten, using the behaviour of  $f_0$  at small values of  $R_0$ ,

$$f_0(R_0) = -\sqrt{\frac{\pi R_0}{s_0 \sinh(\pi s_0)}} \sin[s_0 \ln(\kappa R_0) + \alpha_0] = 0, \quad (3.55)$$

where  $\alpha_0$  is a constant. This leads to the quantified wave-numbers

$$\kappa_n \propto \frac{e^{-n\pi/s_0}}{R_0}. \quad (3.56)$$

The above equation is valid only provided that  $\kappa R_0 \ll 1$ . From our simulation, this condition holds for the fundamental trimer of our Hamiltonian, for which  $E_T \sim 10^{-3} \hbar^2 / (m R_0^2)$  and therefore  $\kappa R_0 \sim 10^{-1}$  (see the simulation results in Section 3.2.3). We set  $n = 0$  to correspond to the fundamental trimer.

Thus, in our system, there are infinitely many Efimov trimers, whose wave-numbers are given by

$$\kappa_n = \kappa_0 e^{-n\pi/s_0} = \frac{\kappa_0}{22.7^n} \quad n \geq 0, \quad (3.57)$$

or, alternatively, whose energies are given by

$$E_n = E_0 e^{-2n\pi/s_0} = \frac{E_0}{515^n} \quad n \geq 0, \quad (3.58)$$

where  $E_0$  is the energy of the fundamental Efimov trimer. From Braaten and Hammer (2006), we can relate the mean-square hyperradius to  $\kappa_0$  by numerical integration,

$$\langle R^2 \rangle = \frac{2(1 + s_0^2)}{3} \kappa_0^{-2}, \quad (3.59)$$

which gives

$$E_0 = 4.27 \times 10^{-3} \frac{\hbar^2}{m R_0^2}. \quad (3.60)$$

From Eq. 3.57 and 3.58, we see that the  $(n + 1)$ -th excited trimer is a rescaled version of the  $n$ -th excited trimer, with  $E_n/E_{n+1} = 515$ , and with all distances multiplied by a

factor 22.7. In particular, the first excited trimer is 22.7 times larger than the fundamental trimer. For quantum coherence to be built on such a larger size, the thermal de Broglie wave-length  $\lambda_{\text{th}}$ , which is the scale that the wave-functions of bosons span, needs to be multiplied by the same factor: the first excited trimer could only be seen at temperatures 515 times smaller than that at which we start probing the fundamental Efimov trimer. However, such a temperature is also very small compared to the binding energy of the fundamental Efimov trimer, so that at such a temperature, only the fundamental Efimov trimer is thermodynamically populated. This is the reason why any simulation that probes thermodynamics, and ours in particular, is incapable of observing excited Efimov trimers.

### Other interaction potentials

For a general pair-interaction potential without a pure three-body interaction, such as the more realistic Lennard–Jones interaction potential, at distances higher than a given interaction distance, and therefore, at large hyperradii, the pair-interaction potential effectively vanishes, which means that the effective channel potential  $V_0$  (see Eq. 3.52) is valid above these distances.

At small hyperradial values, the channel potential deviates from its universal value  $V_0$  as the pair interaction becomes non-negligible. This short-hyperradii deviation is absent from our zero-range interaction potential (this leads to the Thomas collapse, see Section 3.2.1), but the three-body hard core  $V_3$  plays the same role although, as discussed above, it does not lead to significant deviations from universal theory.

Therefore, for large hyperradii, the hyperradial wave-function of Eq. 3.53 remains valid, and the value of the hyperradial wave-number  $\kappa$  is determined by the short-hyperradius non-universal Schrödinger equation. If  $\kappa$  is small enough that it is possible to neglect the deviations from the effective channel potential  $V_0$  while keeping  $\kappa R \ll 1$ , we may write, for this range of values of  $R$ , similarly to Eq. 3.55,

$$f_0(R) \xrightarrow{\kappa R \ll 1} -\sqrt{\frac{\pi R}{s_0 \sinh(\pi s_0)}} \sin [s_0 \ln(\kappa R) + \alpha_0], \quad (3.61)$$

and the continuity of the logarithmic derivative of  $f_0$  can be used to match its non-universal value at small  $R$  to the universal solution in Eq. 3.61 at a point  $R_{\text{match}}$  where both expressions are valid:

$$R_{\text{match}} \frac{f_0'(R_{\text{match}})}{f_0(R_{\text{match}})} = \frac{1}{2} + s_0 \cot [s_0 \ln(\kappa R_{\text{match}}) + \alpha] \quad (3.62)$$

which yields the same scaling properties as above (Eq. 3.57 and 3.58). Of course, these properties are accurate provided that a matching point where both expressions of  $f_0$  are valid exists, that is, that  $R_{\text{match}}$  is a point where non-universal effects can be neglected and  $\kappa_n$  is small enough that  $\kappa_n R_0 \ll 1$ . At larger values of  $\kappa$ , and therefore at larger binding energies, the scaling properties are no longer valid, and non-universal trimer states may exist.

This shows that, in general, excited trimer states are asymptotically universal in the limit  $n \rightarrow \infty$ , in the sense that their properties do not depend on the short-range behaviour of the interaction potential. As we just saw, for a generic interaction, the fundamental and first few excited trimers may experience possibly large deviations from universal theory. In general, the phrase *Efimov trimers* qualifies trimers whose deviations from unitarity can be neglected.

If we go back to our model, we notice that the universal wave-function of Eq. 3.53 is valid only for  $R \geq R_0$ . When  $n$  is increased, the size of the trimers is increased, so that the  $R \leq R_0$  region consists in a smaller and smaller portion of space: the relative domain on which the universal wave-function is valid is larger and larger when  $n$  is increased. This is the only deviations from universality that our model experiences, and, in practice, for  $R \leq R_0$ , the universal wave-function of Eq. 3.53 oscillates so quickly that, within very good approximation, we may state that the fundamental trimer of our model interaction potential is an Efimov trimer.

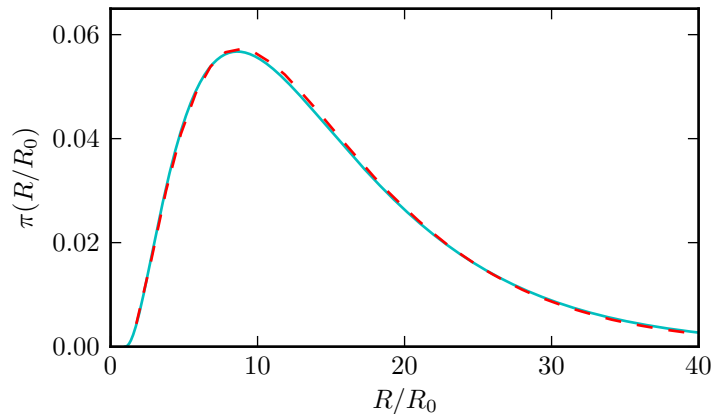


Figure 3.10: Comparison of the numerical hyperradial density distribution obtained by ensemble averaging of the configurations of our single trimer simulation (*dashed red line*) to the exact hyperradial distribution of Eq. 3.63 (*solid cyan line*), for  $\hbar^2\beta/(mR_0^2) = 1600$ . The fit obtains a value of  $R_0 = 0.80R_0^{\text{input}}$ .

### Hyperradial probability distribution and rescaling of $R_0$

I now describe how the three-bosons simulation of Section 3.2.3 *quantitatively* compares with the universal theory described in the last few paragraphs. In particular, it is possible to compare the hyperradial distribution obtained in Fig. 3.8 to its universal value of Eq. 3.53,

$$\pi(R) \propto f_0(R)^2 = RK_{is_0}^2 \left( \sqrt{2}\kappa_0 R \right) \quad (R \geq R_0). \quad (3.63)$$

(The proportionality sign is due to the absence of normalization in Eq. 3.53.) We observed that this comparison works only when  $R_0$  is included as a fit parameter, which means that

we need to correct the input value of  $R_0$  of our program (that in the following is called  $R_0^{\text{input}}$ ). With this correction, in agreement with the above theoretical considerations, the comparison is quantitatively very satisfying (see Fig. 3.10).

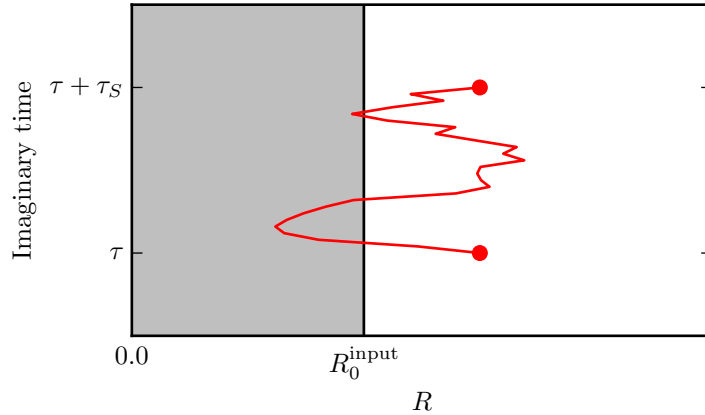


Figure 3.11: Situation on one single imaginary time slice of a simulation where the three-body hard core is included through the Trotter approximation (see Section 1.2.1). At the two points where the three-body hard core condition is enforced, the condition  $R \geq R_0$  is satisfied. However, this configuration accounts for all free paths going between these two points, some of which wander into the  $R < R_0$  region, yielding an effective value of  $R_0$  smaller than its input value  $R_0^{\text{input}}$ .

This correction is caused by  $\tau_S$  being finite. As illustrated in Fig. 3.11, the finite imaginary time slice  $\tau_S$  causes some paths that would not be taken into account in the limit  $\tau_S \rightarrow 0$  to be included in the statistical weight between two slices, that takes into account all free paths that propagate between two consecutive discretization points (see Section 1.2.1), some of which step into the  $R < R_0$  region.

As the shift in  $R_0$  is related to free paths propagating on an imaginary time  $\tau_S$ , if we define it quantitatively by

$$\Delta R_0 = R_0^{\text{input}} - R_0, \quad (3.64)$$

we must have a relation of the type

$$\Delta R_0 \propto \lambda_S \quad (3.65)$$

in the limit  $\lambda_S \ll R_0$ , where  $\lambda_S = \lambda_{\text{th}}(\tau_S)$  is the de Broglie thermal wave-length on one imaginary time slice (see Eq. 1.11). As shown in Fig. 3.12, this proportionality relation holds well.

This numerically proves that, provided that the value of  $R_0$  is properly rescaled, the fundamental trimer of the model Hamiltonian of Eq. 3.24 is an Efimov trimer for all practical purposes.

### 3.3 Conclusion

In this chapter, I described and used a simple model Hamiltonian consisting in a zero-range unitary pair interaction regularized by a three-body hard core. After having explained what holds Efimov trimers together with a simple path-integral argument, I described the underlying theory of the Efimov effect and, using our path-integral Monte Carlo simulation, I showed that the model Hamiltonian reproduces Efimov trimers. In the following chapter, I use this model Hamiltonian as the building block of a many-particle simulation of the unitary Bose gas.

## Appendix 3.A Path-integral argument for the dimer state

The path-integral formalism may be used to show semi-quantitatively that a dimer state forms depending on the value of  $a$ . Let us consider two particles interacting *via* the square-well interaction potential discussed in Section 3.1.1, of which we study the relative motion, described as a single particle of mass  $m/2$ .

We compare the paths going twice in the  $r < r_0$  region (hereafter referred to as *type 2 paths*) to those going through that region only once (hereafter referred to as *type 1 paths*). Such paths are depicted on Fig. 3.13.

### Weight of type 1 paths

As free paths most probably do not return the  $r < r_0$  region once they have left it, the statistical weight of type 1 paths is the same as that of free paths originating and ending

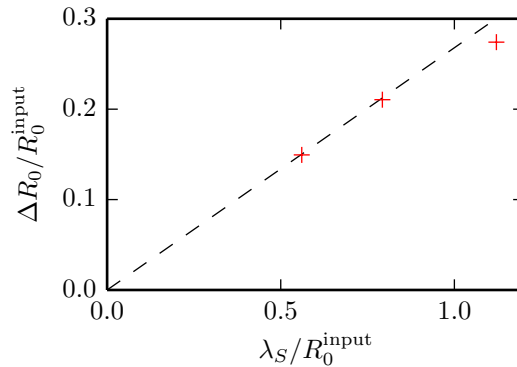
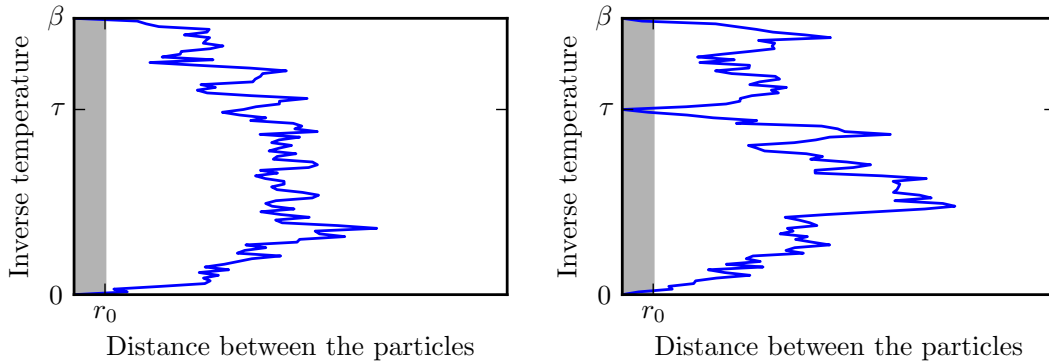


Figure 3.12: Plot of  $\Delta R_0$  as a function of  $\lambda_S$ , using simulations at a fixed value of  $\hbar^2\beta/[m(R_0^{\text{input}})^2] = 512$ . The red crosses show the shifts obtained by fitting the numerical hyperradial distribution against the exact analytical distribution of Eq. 3.63. The dashed black line shows that the proportionality relation in Eq. 3.65 holds well.



(a) Path travelling through  $r < r_0$  only once      (b) Path travelling through  $r < r_0$  twice

Figure 3.13: Paths going through  $r < r_0$  once (left, type 1 path) or twice (right, type 2 path).

in  $(0,0,0)$ . As the imaginary time spent in the  $r < r_0$  region has to be proportional to  $\tau_0 = mr_0^2/2\hbar^2$ , the weight of type 1 paths may be approximated to

$$w_1(\beta) = \underbrace{\left(\frac{m}{4\pi\hbar^2\beta}\right)^{3/2}}_{\text{Weight of the free path}} \cdot \underbrace{\frac{4}{3}\pi r_0^3}_{\text{Choice of the origin}} \cdot \underbrace{e^{2\tau_0 V_0}}_{\text{Effect of the interaction}}. \quad (3.66)$$

### Weight of type 2 paths

A type 2 path comes back once in the  $r < r_0$  region, and may be described as two consecutive type 1 paths, one of them at inverse temperature  $\tau$  and the other at inverse temperature  $\beta - \tau$ . The intermediate time step  $\tau$  should be integrated out as we would like to compare the weight of *all* type 1 paths to that of *all* type 2 paths,

$$w_2 = \int_{\tau_0}^{\beta - \tau_0} \frac{d\tau}{2\tau_0} w_1(\tau) w_1(\beta - \tau). \quad (3.67)$$

The ultraviolet cutoff and the normalization were introduced for the following reasons:

- a path cannot return in the  $r < r_0$  region before it has left it, therefore we should not integrate on regions closer than  $\tau_0$  to  $\tau = 0$  and  $\tau = \beta$ .
- a path takes an imaginary time  $2\tau_0$  to travel through the  $r < r_0$  region, hence the normalization  $N = 2\tau_0$ .

Carrying out the integral yields

$$w_2 = \left[ \left(\frac{m}{4\pi\hbar^2}\right)^{3/2} \frac{4}{3}\pi r_0^3 e^{2\tau_0 V_0} \right]^2 \frac{2(\beta - 2\tau_0)}{\tau_0 \beta^2 \sqrt{\tau_0(\beta - \tau_0)}} \xrightarrow{\beta \gg \tau_0} \frac{2}{3} \sqrt{\frac{2}{\pi}} e^{\tau_0 V_0} w_1. \quad (3.68)$$

Thus, the condition for type 2 paths to be favoured over type 1 paths is:

$$w_2 > w_1 \Leftrightarrow \frac{mr_0^2 V_0}{\hbar^2} > \log\left(\frac{3}{2}\sqrt{\frac{\pi}{2}}\right) \approx 0.63. \quad (3.69)$$

When type 2 paths are favoured over type 1 paths, each of the two type 1 paths that constitute type 2 paths is also less favoured than a path that come back again in the  $r < r_0$  region. Thus, once the above condition is met, the paths should come back into the square well as much as possible, hence creating a dimer: free paths are unstable.

The value we found is of the same order of magnitude as the exact value  $\pi^2/4 \approx 2.47$  (see Section 3.1.1). In fact, we made a quite a few approximations, as  $\tau_0$  should be multiplied by a dimensionless factor at each place where it appears. These are the origin of the difference with the analytical result.

## Appendix 3.B Calculation of the pair-product zero-range correction factor

As explained in Section 3.1.2, the zero-range interaction potential cannot be treated in the Trotter approximation. To use it in a simulation, it is necessary to obtain the corresponding correction factor in the pair-product approximation. The derivation of this correction factor, that follows, is therefore essential to the results of both Chapter 3 and 4.

We recall the pair-product correction factor to the free density matrix in the  $s$ -wave approximation (which is here exact, see Section 2.1.1 and 3.1.2),

$$g(\mathbf{x}_1, \mathbf{x}_2; \mathbf{x}'_1, \mathbf{x}'_2; \tau_S; a) = 1 + \frac{\rho_s^{\text{relative}}(r, r'; \tau_S; a) - \rho_{s, \text{free}}^{\text{relative}}(r, r'; \tau_S; a)}{\rho_{\text{free}}(\mathbf{r}, \mathbf{r}'; \tau_S; a)}. \quad (3.70)$$

Here,  $\mathbf{x}_1$  and  $\mathbf{x}_2$  respectively denote the positions of particles 1 and 2 at slice  $s$ ,  $\mathbf{x}'_1$  and  $\mathbf{x}'_2$  at slice  $s + 1$ , and  $\mathbf{r} = \mathbf{x}_2 - \mathbf{x}_1$  and  $\mathbf{r}' = \mathbf{x}'_2 - \mathbf{x}'_1$  the pair separations between particles 1 and 2 respectively at slices  $s$  and  $s + 1$ .

We saw that, within the zero-range approximation, the  $s$ -wave radial wave-function is (see Eq. 3.12)

$$R_{ks}(r) = \sqrt{\frac{2}{\pi}} \frac{\sin(kr - \arctan(ka))}{r}. \quad (3.71)$$

Therefore, the relative-motion  $s$ -wave contribution to the two-body density matrix is

$$\rho_s^{\text{relative}}(r, r'; \tau_S) = \frac{1}{4\pi} \int_0^{+\infty} dk e^{-\tau_S \hbar^2 k^2 / m} R_{ks}(r) R_{ks}^*(r') \quad (3.72)$$

$$= \frac{1}{4\pi^2 r r'} \int_0^{+\infty} dk e^{-\tau_S \hbar^2 k^2 / m} (\cos[k(r' - r)] - \cos[k(r + r') - 2 \arctan(ka)]). \quad (3.73)$$

From that, we can compute the difference between the full and the free density matrices, which is directly used in Eq. 3.70,

$$\Delta\rho_s = \rho_s^{\text{relative}} - \rho_s^{\text{free}} = \frac{a}{2\pi^2 r r'} \int_0^{+\infty} \frac{k e^{-\tau_S \hbar^2 k^2 / m} dk}{\sqrt{1 + k^2 a^2}} \sin[\arctan(ka) - k(r + r')] = \frac{1}{2\pi^2 r r'} \Delta\tilde{\rho}_s. \quad (3.74)$$

To evaluate Eq. 3.74, we expand the sine term:

$$\Delta\tilde{\rho}_s = \underbrace{\int_0^{+\infty} \frac{k^2 a^2 dk}{1 + k^2 a^2} e^{-\tau_S \hbar^2 k^2 / m} \cos(ku)}_{I_1} - \underbrace{\int_0^{+\infty} \frac{k a dk}{1 + k^2 a^2} e^{-\tau_S \hbar^2 k^2 / m} \sin(ku)}_{I_2}, \quad (3.75)$$

where we set  $u = r + r'$ .

Let us define  $I_0$  as

$$I_0 = \int_0^{\infty} \frac{dk}{1 + k^2 a^2} e^{-\tau_S \hbar^2 k^2 / m} \cos(ku). \quad (3.76)$$

$I_0$  gives access to  $I_1$  and  $I_2$  as  $I_1 = -(ma^2/\hbar^2)\partial_{\tau_S} I_0$  and  $I_2 = \int_0^u du' I_1(\tau_S, a, u')/a$ . Let us compute  $I_0$ .

$$I_0 = \frac{1}{2} \int_{-\infty}^{\infty} \frac{dk}{1 + k^2 a^2} e^{-\tau_S \hbar^2 k^2 / m + iku} \quad (3.77)$$

$$= \frac{1}{4} \underbrace{\int_{-\infty}^{\infty} \frac{dk}{1 + ik|a|} e^{-\tau_S \hbar^2 k^2 / m + iku}}_{I_+} + \frac{1}{4} \underbrace{\int_{-\infty}^{\infty} \frac{dk}{1 - ik|a|} e^{-\tau_S \hbar^2 k^2 / m + iku}}_{I_-} \quad (3.78)$$

The integrals  $I_{\pm}$  may be cast into the form

$$I_{\pm} = \int_{-\infty}^{\infty} \frac{dk}{1 \pm ik|a|} \exp \left[ -\frac{\tau_S \hbar^2}{m} \left( k - i \frac{um}{2\tau_S \hbar^2} \right)^2 - \frac{u^2 m}{4\tau_S \hbar^2} \right] \quad (3.79)$$

$$= \pm e^{-u^2 m / 4\tau_S \hbar^2} \int_{-\infty - iu/2\tau_S}^{\infty - iu/2\tau_S} \frac{dk}{ik|a| - um|a|/2\tau_S \hbar^2 \pm 1} e^{-\tau_S \hbar^2 k^2 / m} \quad (3.80)$$

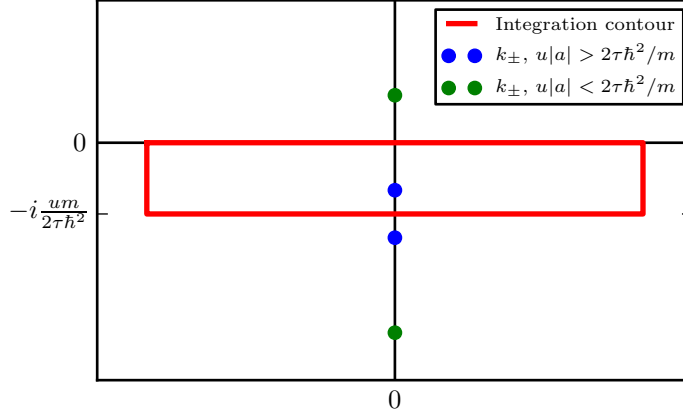
To compute  $I_{\pm}$ , we use the integration contour described on Fig. 3.14. The poles of  $I_{\pm}$  are:

$$k_{\pm} = -i \frac{um}{2\tau_S \hbar^2} \pm \frac{i}{|a|}. \quad (3.81)$$

We notice that  $k_-$  is never in the integration contour, and  $k_+$  is only if  $u|a| > 2\tau_S \hbar^2 / m$ .

Since the integrals on the vertical part of the contour go to 0 when the width of the contour goes to  $\infty$ , we can equate the integration on  $\mathbb{R}$  to that on  $\mathbb{R} - ium/2\tau_S \hbar^2$ , taking into account the possible residues:

$$I_{\pm} = \pm e^{-u^2 m / 4\tau_S \hbar^2} \int_{-\infty}^{\infty} \frac{dk}{ik|a| - um|a|/2\tau_S \hbar^2 \pm 1} e^{-\tau_S \hbar^2 k^2 / m} + 2i\pi \text{Residues}. \quad (3.82)$$

Figure 3.14: Poles and integration contour for integrals  $I_{\pm}$ .

This allows us to write:

$$\begin{cases} I_+ = -\frac{\pi}{|a|} e^{\tau_S \hbar^2 / (ma^2) - u/a} \operatorname{erfc} \left( \frac{u}{2\hbar} \sqrt{\frac{m}{\tau_S}} - \frac{\hbar}{|a|} \sqrt{\frac{\tau_S}{m}} \right) + \frac{2\pi}{|a|} e^{\tau_S \hbar^2 / (ma^2) - u/|a|} & u|a|m > 2\tau_S \hbar^2, \\ I_+ = \frac{\pi}{|a|} e^{\tau_S \hbar^2 / (ma^2) - u/|a|} \operatorname{erfc} \left( \frac{\hbar}{|a|} \sqrt{\frac{\tau_S}{m}} - \frac{u}{2\hbar} \sqrt{\frac{m}{\tau_S}} \right) & u|a|m < 2\tau_S \hbar^2, \\ I_- = \frac{\pi}{|a|} e^{\tau_S \hbar^2 / (ma^2) + u/|a|} \operatorname{erfc} \left( \frac{\hbar}{|a|} \sqrt{\frac{\tau_S}{m}} + \frac{u}{2\hbar} \sqrt{\frac{m}{\tau_S}} \right), \end{cases} \quad (3.83)$$

where  $\operatorname{erfc}$  is the complementary error function related to the error function  $\operatorname{erf}$  by  $\operatorname{erfc} = 1 - \operatorname{erf}$ . Using the identity  $\operatorname{erfc}(-x) = 2 - \operatorname{erfc}(x)$ , we notice that both expressions of  $I_+$  are identical regardless of the values of  $u|a|m$  and  $2\tau_S/\hbar^2$ . Therefore,

$$I_0 = \frac{\pi}{4|a|} e^{\tau_S \hbar^2 / (ma^2)} \left[ e^{u/|a|} \operatorname{erfc} \left( \frac{\hbar}{|a|} \sqrt{\frac{\tau_S}{m}} + \frac{u}{2\hbar} \sqrt{\frac{m}{\tau_S}} \right) + e^{-u/|a|} \operatorname{erfc} \left( \frac{\hbar}{|a|} \sqrt{\frac{\tau_S}{m}} - \frac{u}{2\hbar} \sqrt{\frac{m}{\tau_S}} \right) \right]. \quad (3.84)$$

We stated above that  $I_1 = -(ma^2/\hbar^2) \partial_{\tau_S} I_0$ . This yields

$$I_1 = \sqrt{\frac{\pi m}{4\tau_S \hbar^2}} e^{-mu^2/(4\tau_S \hbar^2)} - \frac{\pi}{4|a|} e^{\tau_S \hbar^2 / (ma^2)} \left[ e^{u/|a|} \left( \frac{\hbar}{|a|} \sqrt{\frac{\tau_S}{m}} + \frac{u}{2\hbar} \sqrt{\frac{m}{\tau_S}} \right) \right. \quad (3.85)$$

$$\left. + e^{-u/|a|} \operatorname{erfc} \left( \frac{\hbar}{|a|} \sqrt{\frac{\tau_S}{m}} - \frac{u}{2\hbar} \sqrt{\frac{m}{\tau_S}} \right) \right]. \quad (3.86)$$

In the same fashion, we obtain  $I_2$  as  $\int_0^u I_1/a$ :

$$I_2 = \frac{\pi}{4a} e^{\tau_S \hbar^2 / (ma^2)} \left[ e^{-u/|a|} \operatorname{erfc} \left( \frac{\hbar}{|a|} \sqrt{\frac{\tau_S}{m}} - \frac{u}{2\hbar} \sqrt{\frac{m}{\tau_S}} \right) - e^{u/|a|} \operatorname{erfc} \left( \frac{\hbar}{|a|} \sqrt{\frac{\tau_S}{m}} + \frac{u}{2\hbar} \sqrt{\frac{m}{\tau_S}} \right) \right]. \quad (3.87)$$

The values of  $I_1$  and  $I_2$  yield  $\Delta\tilde{\rho}_s$  (see Eq. 3.75):

$$\Delta\tilde{\rho}_s = I_1 - I_2 = \frac{1}{2} \left[ \sqrt{\frac{\pi m}{\tau_S \hbar^2}} e^{-(r+r')^2 m / (4\tau_S \hbar^2)} \right. \quad (3.88)$$

$$\left. - \frac{\pi}{|a|} e^{\tau_S \hbar^2 / (ma^2) - (r+r')/a} \operatorname{erfc} \left( \frac{\hbar}{|a|} \sqrt{\frac{\tau_S}{m}} - \operatorname{sgn} a \frac{u}{2\hbar} \sqrt{\frac{m}{\tau_S}} \right) \right]. \quad (3.89)$$

In its domain of existence  $a > 0$ , it is necessary to take the bound state into account. Its normalized radial wave-function may be deduced from Section 3.1.2:

$$R_{\text{bound}}(r) = \sqrt{\frac{2}{a}} \frac{e^{-r/a}}{r}. \quad (3.90)$$

The value of the density-matrix contribution of the bound state is then straightforward:

$$\tilde{\rho}_{\text{bound}}(r, r'; \tau_S) = 2\pi^2 r r' \rho_{\text{bound}}(r, r'; \tau_S) = \frac{\pi}{a} e^{-(r+r')/a + \tau_S \hbar^2 / (ma^2)}. \quad (3.91)$$

Using again  $\operatorname{erfc}(-x) = 2 - \operatorname{erfc}(x)$ , we can write the total density-matrix correction when  $a > 0$  as

$$\Delta\tilde{\rho}_s^{\text{total}} = \Delta\tilde{\rho}_s + \tilde{\rho}_{\text{bound}} \quad (3.92)$$

$$= \frac{1}{2} \sqrt{\frac{\pi m}{\tau_S \hbar^2}} e^{-(r+r')^2 m / (4\tau_S \hbar^2)} + \frac{\pi}{2a} e^{\tau_S \hbar^2 / (ma^2) - (r+r')/a} \operatorname{erfc} \left( \frac{r+r'}{2\hbar} \sqrt{\frac{m}{\tau_S}} - \frac{\hbar}{a} \sqrt{\frac{\tau_S}{m}} \right). \quad (3.93)$$

We notice that Eq. 3.89 gives the same equation for  $a < 0$ .

The limit  $a \rightarrow 0^-$  describes a free particle. As  $\operatorname{erfc} x \approx e^{-x^2} / (x\sqrt{\pi})$  for  $x \gg 1$ , we have indeed

$$\lim_{a \rightarrow 0^-} \Delta\rho_s^{\text{total}} = 0. \quad (3.94)$$

Dividing  $\Delta\rho_s^{\text{total}}$  by  $\rho_{\text{relative}}^{\text{free}}$  gives the pair-product correction factor for the zero-range potential. The free relative-motion density matrix, given by Eq. 1.5 with a mass  $m/2$ , may be rewritten

$$\rho_{\text{relative}}^{\text{free}}(r, r'; \tau_S) = \left( \frac{m}{4\pi\hbar^2\tau_S} \right)^{3/2} \exp \left[ -\frac{m(r+r')^2}{4\tau_S\hbar^2} + \frac{mrr'(1+\cos\gamma)}{2\tau_S\hbar^2} \right], \quad (3.95)$$

where  $\gamma$  is the relative angle between vectors  $\mathbf{r}$  and  $\mathbf{r}'$ .

Using its expression in the  $s$ -wave approximation (see Eq. 3.70), we obtain the pair-product correction factor for all values of  $a$

$$g(\mathbf{r}, \mathbf{r}'; \tau_S; a) = 1 + \frac{2\tau_S\hbar^2}{mrr'} \left[ 1 + \frac{\hbar\sqrt{\pi\tau_S}}{ma} e^{\left(\frac{r+r'}{2\hbar} \sqrt{\frac{m}{\tau_S}} - \frac{\hbar}{a} \sqrt{\frac{\tau_S}{m}}\right)^2} \operatorname{erfc} \left( \frac{r+r'}{2\hbar} \sqrt{\frac{m}{\tau_S}} - \frac{\hbar}{a} \sqrt{\frac{\tau_S}{m}} \right) \right] \quad (3.96)$$

$$\times \exp \left[ -\frac{mrr'(1+\cos\gamma)}{2\tau_S\hbar^2} \right]. \quad (3.97)$$

## Appendix 3.C Hyperspherical coordinates

This section reviews coordinate systems applying to the three-body problem, that are used throughout Chapter 3.

As with the two-body problem, it is possible to separate the motion of the centre of mass from the relative motion of the three particles (Braaten and Hammer, 2006). If we keep with the case of three identical bosons of mass  $m$ , we may define the coordinates of the centre of mass  $\mathbf{x}_{\text{CM}} = (\mathbf{x}_1 + \mathbf{x}_2 + \mathbf{x}_3)/3$  (where  $\mathbf{x}_i$  is the position of boson  $i$ ) and two other coordinates, called the *Jacobi coordinates*,

$$\begin{cases} \mathbf{r}_{ij} = \mathbf{r}_j - \mathbf{r}_i \\ \mathbf{r}_{k,ij} = \mathbf{r}_k - \frac{1}{2}(\mathbf{r}_i + \mathbf{r}_j). \end{cases} \quad (3.98)$$

This set of coordinates is already quite useful, since the kinetic energy operator may be separated into the motion of three independent particles of masses  $3m$  (centre of mass),  $m/2$ , and  $2m/3$ , as the kinetic energy operator is diagonal in the three coordinates  $\mathbf{x}_{\text{CM}}$ ,  $\mathbf{r}_{ij}$ , and  $\mathbf{r}_{k,ij}$

$$-\frac{\hbar^2}{2m} \left( \frac{\partial^2}{\partial \mathbf{x}_1^2} + \frac{\partial^2}{\partial \mathbf{x}_2^2} + \frac{\partial^2}{\partial \mathbf{x}_3^2} \right) = -\frac{\hbar^2}{2m} \left( \frac{1}{3} \frac{\partial^2}{\partial \mathbf{x}_{\text{CM}}^2} + 2 \frac{\partial^2}{\partial \mathbf{r}_{ij}^2} + \frac{3}{2} \frac{\partial^2}{\partial \mathbf{r}_{k,ij}^2} \right). \quad (3.99)$$

The Jacobi coordinates may be used to compute the properties of three interacting bosons in relative space only, not sampling the centre of mass and, in theory, making the simulation of a trimer converge faster. (In practice, this did not lead to an important speed-up of the simulation of a trimer.)

From the Jacobi coordinates, it is possible to define the *hyperspherical coordinates*. As with spherical coordinates, the idea is to replace the 6 coordinates  $\mathbf{r}_k$  and  $\mathbf{r}_{k,ij}$  by one hyperradial coordinate and five angular degrees of freedom. The hyperradius  $R$  is defined by

$$R^2 = \frac{1}{2}r_{ij}^2 + \frac{2}{3}r_{k,ij}^2 = \frac{1}{3}(r_{12}^2 + r_{23}^2 + r_{31}^2), \quad (3.100)$$

the first angular coordinate (called the *Delves hyperangle*)  $\alpha_k$  by

$$\alpha_k = \arctan \frac{\sqrt{3}r_{ij}}{2r_{k,ij}}, \quad (3.101)$$

and the four remaining angular coordinates are given by the directions of  $\mathbf{r}_{ij}$  and  $\mathbf{r}_{k,ij}$ . The five angular coordinates are collectively denoted by  $\Omega$ .

The Delves hyperangle is zero when  $r_{ij} \ll r_{k,ij}$ , and infinite when  $r_{ij} \gg r_{k,ij}$ : it measures the ratio of the relative distance between two particles  $i$  and  $j$  to the distance between particle  $k$  and their centre of mass. Therefore, it is quite relevant to describe Efimov trimers, that are a superposition of states where two particles are close and the third far from them (see Section 3.2.2, 3.2.3, and the Faddeev equation Eq. 3.48).

The kinetic energy operator may be expressed in terms of the hyperspherical coordinates:

$$-\frac{\hbar^2}{2m} \left( 2 \frac{\partial^2}{\partial \mathbf{r}_{ij}^2} + \frac{3}{2} \frac{\partial^2}{\partial \mathbf{r}_{k,ij}^2} \right) = T_R + T_{\alpha_k} + \frac{\Lambda_{k,ij}^2}{2mR^2}, \quad (3.102)$$

where

$$T_R = -\frac{\hbar^2}{2m} \left( \frac{\partial^2}{\partial R^2} + \frac{5}{R} \frac{\partial}{\partial R} \right) \quad (3.103)$$

is the hyperradial kinetic energy operator,

$$T_{\alpha_k} = -\frac{\hbar^2}{2mR^2} \left[ \frac{\partial^2}{\partial \alpha_k^2} + 4 \cot(2\alpha) \frac{\partial}{\partial \alpha} \right] \quad (3.104)$$

is the Delves hyperangle kinetic energy operator, and  $\Lambda_{k,ij}$  is a generalized angular momentum operator expressed in terms of the angular momentum operators associated to  $\mathbf{r}_{ij}$  and  $\mathbf{r}_{k,ij}$ ,

$$\Lambda_{k,ij}^2 = \frac{\mathbf{L}_{ij}^2}{\sin^2 \alpha_k} + \frac{\mathbf{L}_{k,ij}^2}{\cos^2 \alpha_k}. \quad (3.105)$$



## CHAPTER 4

---

### The unitary Bose gas

---

In experiments, Efimov trimers were observed through the three-body losses of the near-unitary Bose gas (Kraemer *et al.*, 2006; Zaccanti *et al.*, 2009; Pollack *et al.*, 2009). These losses into deeply-bound pair states are also responsible for the difficulties to observe a unitary Bose gas at low temperature, as their rate is proportional to  $a^4$  (Esry *et al.*, 1999). Important experimental efforts are currently made towards observing the unitary Bose gas, and its momentum distribution was observed in an out-of-equilibrium regime (Makotyn *et al.*, 2014). Its low-temperature thermodynamic properties, however, are still unknown.

Nevertheless, insights are provided by the known zero-temperature behaviour of groups of more than three unitary bosons. Efimov tetramers, that may be fully described by three-body Efimov observables (von Stecher *et al.*, 2009), were observed through the four-body losses of the near-unitary Bose gas (Ferlaino *et al.*, 2009). Numerical studies, either in a harmonic trap (Thøgersen *et al.*, 2008) or in homogeneous space (von Stecher, 2010), have shown that the ground state of up to  $\sim 10$  bosons is a cluster state. Therefore, unitary bosons are expected to clusterize at low temperature, whereas they should still behave as an ideal gas at high temperature.

As we saw in Chapter 3, the path-integral Monte Carlo simulation of three unitary bosons succeeds in probing the thermodynamic behaviour of Efimov trimers. In this chapter, I describe a generalization of that algorithm to up to 100 bosons, and use it to show that the unitary Bose gas exists under three phases: the normal gas, the conventional Bose–Einstein condensate, and a third phase that corresponds to the previously described clusters, the Efimov liquid. The latter phase is a superfluid state that may be accessed from the two other phases by a first-order phase transition, and whose transition line with the Bose–Einstein condensate ends in a critical point. I also provide a few insights on how this phase diagram could be probed in experiments. These results were presented in [Publication 2](#).

## 4.1 High-temperature equation of state

At high temperature, the unitary Bose gas is in a normal gas phase. In this section, after having described the many-body path-integral Monte Carlo simulation of unitary bosons, I obtain the numerical equation of state of that normal gas phase and compare it to that obtained with the available virial coefficients.

### 4.1.1 Many-body simulation

In order to study the unitary Bose gas, I devised a simulation in a isotropic harmonic trap of frequency  $\omega$ .

#### Hamiltonian

The model Hamiltonian of the unitary Bose gas simulation is the generalization to  $N$  bosons of the zero-range pair interaction  $V_2$  regularized by the hyperradial cutoff  $V_3$ , here applied to all triples of bosons:

$$H = - \sum_{i=1}^N \left[ \frac{\hbar^2}{2m} \nabla_i^2 + V_{\text{trap}}(\mathbf{x}_i) \right] + \sum_{i \neq j} V_2(r_{ij}) + \sum_{i,j,k} V_3(R_{ijk}), \quad (4.1)$$

where the hyperradius  $R_{ijk}$  for the three bosons  $(i, j, k)$  is defined by

$$R_{ijk}^2 = \frac{1}{3} (r_{ij}^2 + r_{jk}^2 + r_{ki}^2), \quad (4.2)$$

and the trapping potential by

$$V_{\text{trap}}(\mathbf{x}) = \frac{1}{2} m \omega^2 \mathbf{x}^2. \quad (4.3)$$

Unlike the single-trimer simulation, the  $N$ -bosons simulation is not restricted to a single permutation cycle: the length of permutation cycles accounts for the superfluid fraction in the Bose gas (see Section 1.1.1). Permutation cycles are sampled through multiple-slice permutation moves similar in their principle to the single-slice permutation move described (but not used) in Section 3.2.3.

In the  $N$ -bosons simulation, the Bethe–Peierls divergence of the pair probability distribution (see Eq. 3.13) is also dealt with through the compression-dilation algorithm (see Section 3.2.3). Proposing compression-dilation moves only for pairs of bosons that are nearest neighbours is even more crucial than in the three-body simulation: picking at random two bosons on which to perform the move would mostly consist in picking pairs of bosons that are quite far from one another, and would be a waste of computing resources.

#### Size of interaction boxes

In Section 1.2.3, we saw that using interaction boxes whose size is the effective correction range of the interactions  $r_{\text{box}}$  allows to significantly reduce the complexity of evaluating

the statistical weight due to interactions involving a given boson. We also saw that, when a pair-product approximation is used,  $r_{\text{box}}$  is of the order of the thermal de Broglie wavelength on one slice  $\lambda_S$ .

Although the pair-product approximation is used for the zero-range unitary pair interaction, the three-body hard-core interaction is enforced following the Trotter framework. To use interaction boxes with the three-body hard core, we must compute its two-body range, that is, the distance from which two bosons cannot be involved, together with *any* third boson, in a triple whose hyperradius  $R$  violates the hyperradial cutoff condition

$$3R^2 = r_{12}^2 + r_{23}^2 + r_{31}^2 \geq 3R_0^2, \quad (4.4)$$

where  $r_{ij}$  is the distance between bosons  $i$  and  $j$ .

If we minimize  $r_{23}^2 + r_{31}^2$  while keeping  $r_{12}$  fixed, we get the smallest value of  $R$  over all possible positions of particle 3. As, for any three points in space, the foot of the altitude going through point 3 has smaller separations  $r_{23}$  and  $r_{31}$  than point 3, we may consider the case where points 1, 2, and 3 are aligned (see Fig. 4.1).

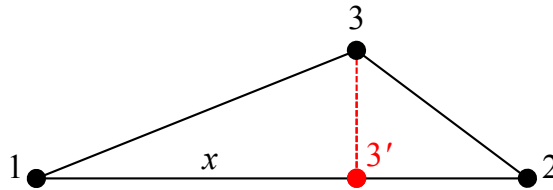


Figure 4.1: Point  $3'$ , the foot of the altitude going through point 3, has smaller distances to points 1 and 2 than point 3, and therefore  $r_{23'}^2 + r_{3'1}^2 \leq r_{23}^2 + r_{31}^2$ .

If the three points are aligned, and  $x$  is the distance between points 1 and 3, minimizing  $r_{23}^2 + r_{31}^2$  is the same as minimizing  $x^2 + (r_{12} - x)^2$ , and the minimal value is  $r_{12}^2/2$ . Therefore, the two-body range of the three-body hard core, that corresponds to the minimal size of interaction boxes associated to it, is

$$r_{12}^2 + \frac{1}{2}r_{12}^2 = 3R_0^2, \quad (4.5)$$

that is,

$$r_{12} = R_0\sqrt{2}. \quad (4.6)$$

We saw previously that interaction boxes associated to the pair interaction are of the order of  $\lambda_S$  (see Section 1.2.3). The interaction boxes associated to the three-body hard core are of size  $R_0\sqrt{2}$ . Several algorithms are possible to conciliate these two prescriptions. At first, one may think of choosing the maximum of  $\lambda_S$  and  $R_0\sqrt{2}$ . However, this may in practice not be optimal if  $\lambda_S \geq R_0\sqrt{2}$ , because the three-body hard core involves three bosons and therefore, to compute the statistical weight of the interactions involving a boson, it must be enforced for each *pair* of neighbouring bosons, which yields a quadratic complexity in terms of the number of neighbours.

From there, a simple solution would be to use two different kinds of boxes: one that suits the pair interaction, and one that suits the three-body hard core. The solution retained in the many-body simulation is to have only one kind of boxes of size  $R_0\sqrt{2}$ . For computing the pair interactions, higher-order neighbouring boxes are taken into account to virtually use boxes of size  $\lambda_S$ . However, in practice, using higher-order boxes was not needed.

### 4.1.2 Equation of state

The high-temperature phase of the unitary Bose gas is necessarily a normal gas, because thermal energy dominates at high temperature. In this section, the equation of state of the normal gas phase of the unitary Bose gas is compared to the first deviations from that of the ideal gas, given by the virial expansion, that is first introduced.

#### Virial expansion

The *virial expansion* of the equation of state of a gas describes its deviations from the classical ideal gas. It is defined as

$$P = nk_B T \sum_{l=1}^{\infty} a_l(T) (n\lambda_{\text{th}}^3)^{l-1}, \quad (4.7)$$

where  $P$  is the pressure of the gas,  $T$  its temperature, and  $n$  its particle density. The coefficients  $\{a_l\}$  are collectively known as *virial coefficients*. For the classical ideal gas,  $a_1 = 1$  and all other virial coefficients are zero.

Closely related to the virial expansion is the *cluster expansion*, which is also an expansion of the equation of state of a gas describing its deviations from the ideal classical gas, but in parametric form, in terms of the fugacity  $e^{\beta\mu}$ , where  $\mu$  is the chemical potential of the gas (Huang, 1987):

$$\begin{cases} P = \frac{k_B T}{\lambda_{\text{th}}^3} \sum_{l=1}^{\infty} b_l(T) e^{l\beta\mu}, \\ n = \frac{1}{\lambda_{\text{th}}^3} \sum_{l=1}^{\infty} l b_l(T) e^{l\beta\mu}. \end{cases} \quad (4.8)$$

The  $l$ -th *cluster integral*  $b_l$  describes the  $l$ -body interactions that cannot be reduced to non-interacting sub-groups of interacting particles. Therefore,  $b_l$  is non-zero for  $l \geq 1$  even for the ideal quantum gas, where it takes into account entanglement.

Virial coefficients and cluster integrals are related by simple relations (Huang, 1987):

$$\begin{cases} a_1 = b_1 = 1, \\ a_2 = -b_2, \\ a_3 = 4b_2^2 - 2b_3, \\ \dots \end{cases} \quad (4.9)$$

Recently, the third virial coefficient of the unitary Bose gas was made available by [Castin and Werner \(2013\)](#). They obtained, for the third cluster integral of the unitary Bose gas:

$$\frac{b_3}{3\sqrt{3}} = C + \sum_{q \geq 0} (e^{-\beta E_q} - 1) + \frac{s_0}{\pi} \left\{ \frac{1}{2} \ln(e^\gamma \beta E_t) - \sum_{q \geq 1} e^{-q\pi s_0} \Re [\Gamma(-iqs_0)(\beta E_T)^{iqs_0}] \right\}, \quad (4.10)$$

where  $C \approx 0.648$  and  $s_0 \approx 1.00624$  are two constants,  $\gamma \approx 0.577$  is the Euler constant, and  $E_q$  is the energy of the  $q$ -th excited Efimov trimer, defined in Eq. 3.58. In practice, it is enough to compute both sums up to  $q = 1$ . [Castin and Werner \(2013\)](#) also obtained the second cluster integral of the unitary Bose gas,

$$b_2 = \frac{9}{2^{5/2}}. \quad (4.11)$$

### Numerical equation of state

Using the two above cluster integrals  $b_2$  and  $b_3$ , we may compare the cluster expansion (Eq. 4.8) of the normal phase of the unitary Bose gas to the numerical grand-canonical equation of state that we obtained through the method presented in Section 2.2.3. As shown on Fig. 4.2, the obtained equation of state is in very good agreement with the cluster expansion up to the third coefficient, where the virial coefficients were computed using the rescaling of  $R_0$  obtained in a three-body simulation (see Section 3.2.4).

As the third cluster integral is the first order that encompasses three-body interactions, and namely the Efimov effect, this good agreement is essential to check that the many-body simulation of the trapped unitary Bose gas works. To our knowledge, this was also the first time that the prediction of [Castin and Werner \(2013\)](#) was confirmed.

## 4.2 Phase diagram of the unitary Bose gas

Now that we saw that the high-temperature behaviour of the unitary Bose gas is very well described in terms of its virial expansion up to the third order, I describe the low-temperature physics of the unitary Bose gas. As we will see in this section, at low temperature and for small values of  $R_0$ , the unitary Bose gas undergoes a first-order phase transition to a new quantum phase, held together by the same effects as Efimov trimers, the *superfluid Efimov liquid*.

### 4.2.1 Transition to the Efimov liquid phase

In order to identify a first-order phase transition, we observe the joint distribution of the distance of the centre of mass of two particles to the trap centre,  $\bar{r}_{ij} = \|\mathbf{x}_i + \mathbf{x}_j\|/2$  and of their pair distance  $r_{ij} = \|\mathbf{x}_j - \mathbf{x}_i\|$  as a function of the temperature.

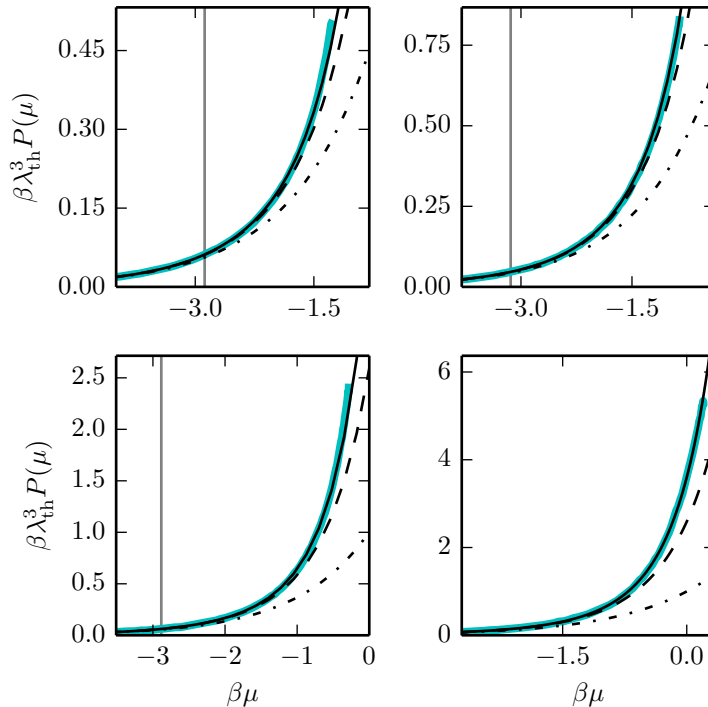


Figure 4.2: Comparison of the cluster expansion (Eq. 4.8) up to the first (*dash-dotted black lines*), second (*dashed black lines*), and third order (*solid black lines*) to the numerical data (*thick cyan lines*) obtained by ensemble averaging and following the method described in Section 2.2.3, for  $T/T_{\text{BEC}}^{\text{trap}} = 1.7$  (*top left*), and  $R_0/l_\omega = 0.07$ ,  $T/T_{\text{BEC}}^{\text{trap}} = 1.4$  and  $R_0/l_\omega = 0.13$  (*top right*),  $T/T_{\text{BEC}}^{\text{trap}} = 1.05$  and  $R_0/l_\omega = 0.18$  (*bottom left*), and  $T/T_{\text{BEC}}^{\text{trap}} = 0.80$  and  $R_0/l_\omega = 0.23$  (*bottom right*), where  $l_\omega = \sqrt{\hbar/(m\omega)}$  is the harmonic trap length. For each curve, the chemical potential at the centre of the trap  $\mu_0$  was determined by a fit to the ideal gas for  $\beta\mu$  smaller than a threshold indicated by the vertical grey line (out of the plotting region for the bottom right curve).

### First-order phase transition

As shown in Fig. 4.3, at high temperature and for small values of  $R_0/l_\omega$ , where  $l_\omega = \sqrt{\hbar/(m\omega)}$  is the harmonic trap length, the joint distribution of  $r_{ij}$  and  $\bar{r}_{ij}$  exhibits only one peak, which corresponds to the normal phase of the gas. When the temperature is decreased, a second peak appears: due to the variation of the local density approximation chemical potential in the trap (see Eq. 2.15), the gas may be found under different thermodynamic phases in different regions of the trap. When the temperature is further decreased, only the second peak persists.

This behaviour, with the appearance of a second peak in the joint density distribution, is typical of a first-order phase transition to a new phase, the superfluid Efimov liquid, and differs fundamentally from second-order phase transitions such as Bose–Einstein con-

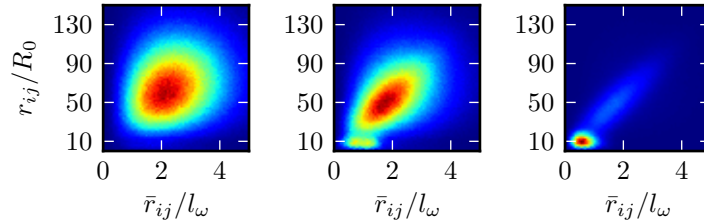


Figure 4.3: Joint distribution of the position of the centre of mass of two trapped particles  $\bar{r}_{ij}$  and their pair separation  $r_{ij}$  for a unitary Bose gas of 100 bosons with  $R_0/l_\omega = 0.07$ . At  $T/T_{\text{BEC}}^{\text{trap}} = 1.7$  (*left*), the distribution is that of the normal phase. At  $T/T_{\text{BEC}}^{\text{trap}} = 1.6$  (*centre*), a second peak appears in the centre of the trap, a sign that part of the gas is in the superfluid Efimov liquid phase. At  $T/T_{\text{BEC}}^{\text{trap}} = 1.5$ , most particles are in the superfluid Efimov liquid phase, with small pair distances  $\sim 10R_0$ .

densation, for which the peak of the joint distribution moves smoothly through the phase transition (see Fig. 4.4).

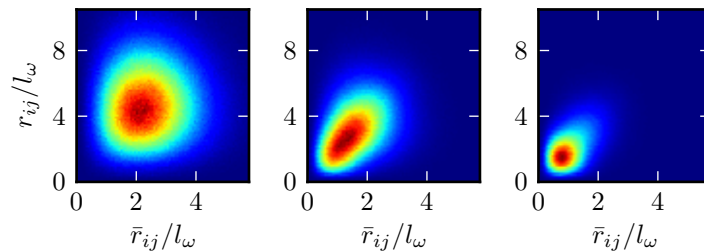


Figure 4.4: Joint distribution of the position of the centre of mass of two trapped particles  $\bar{r}_{ij}$  and their pair separation  $r_{ij}$  for the free Bose gas. The peak of the joint distribution moves continuously from the normal phase at  $T/T_{\text{BEC}}^{\text{trap}} = 1.4$  (*left*) to the regime at  $T/T_{\text{BEC}}^{\text{trap}} = 0.7$  where most of the bosons are in a Bose–Einstein condensate (*right*) through the coexistence region at  $T/T_{\text{BEC}}^{\text{trap}} = 0.9$ .

For larger values of  $R_0/l_\omega$ , however, we see no sign of a first-order phase transition (see Fig. 4.5): there is only one peak in the joint distribution of  $r_{ij}$  and  $\bar{r}_{ij}$ , that stabilizes around the same pair distances  $\sim 10R_0$  as the superfluid Efimov liquid in the case where a first-order phase transition is seen (see Fig. 4.3).

By following the permutation cycle distribution, for such values of  $R_0/l_\omega$ , we notice that the unitary Bose gas undergoes a conventional Bose–Einstein phase transition at temperatures higher than that at which the pair distances stabilize around  $10R_0$  (see Section 1.1.1). We attribute this stabilization of the pair-distance distribution around the same value as in the case of the first-order phase transition to the superfluid Efimov liquid to a cross-over from the Bose–Einstein condensate to a superfluid Efimov liquid behaviour.

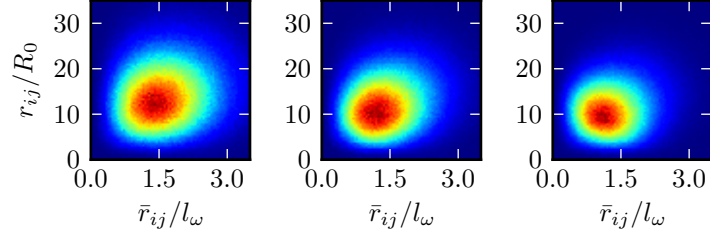


Figure 4.5: Joint distribution of the position of the centre of mass of two trapped particles  $\bar{r}_{ij}$  and their pair separation  $r_{ij}$  for a unitary Bose gas of 100 bosons with  $R_0/l_\omega = 0.23$ . The pair distance distribution decreases smoothly between  $T/T_{\text{BEC}}^{\text{trap}} = 0.9$  and  $T/T_{\text{BEC}}^{\text{trap}} = 0.8$  and has stabilized at pair distances of about  $10R_0$  at  $T/T_{\text{BEC}}^{\text{trap}} = 0.7$ .

### Identification of the first-order phase transition in the intermediate regime

For values of  $R_0/l_\omega$  between 0.07, where the system clearly undergoes a first-order phase transition (see Fig. 4.3), and 0.23, where no first-order phase transition is seen (see Fig. 4.5), it may be hard to determine whether the system undergoes a first-order phase transition or not by only observing the joint distribution of the pair distance and the position of the centre of mass, because the typical pair distances in the normal gas and in the superfluid Efimov liquid become of the same order (see Fig. 4.6).

Nevertheless, a close follow-up of the position of the first peak of the pair distribution function  $\pi(r_{ij})$  allows to determine whether the system undergoes a first-order phase transition (see Fig. 4.7): for small values of  $R_0/l_\omega$ , such as  $R_0/l_\omega = 0.7$  employed in Fig. 4.3, we see a strong step of the position of the first peak of the pair distribution function when the temperature is decreased. For large values of  $R_0/l_\omega$  such as  $R_0/l_\omega = 0.23$ , used in Fig. 4.5,

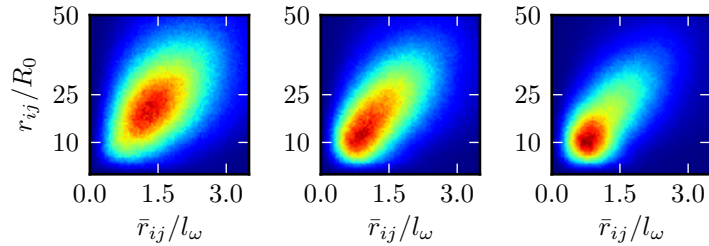


Figure 4.6: Joint distribution of the position of the centre of mass of two trapped particles  $\bar{r}_{ij}$  and their pair separation  $r_{ij}$  for a unitary Bose gas of 100 bosons with  $R_0/l_\omega = 0.13$ , at  $T/T_{\text{BEC}}^{\text{trap}} = 1.17$  (left),  $T/T_{\text{BEC}}^{\text{trap}} = 1.14$  (centre), and  $T/T_{\text{BEC}}^{\text{trap}} = 1.09$  (right). Although the peak of the distribution changes of position on quite a small temperature window, the observation of this histogram does not allow to tell whether the system undergoes a first-order phase transition.

we see no step. For intermediate values of  $R_0/l_\omega$ , such as  $R_0/l_\omega = 0.13$ , used in Fig. 4.6, we see that a step may still be present, therefore indicating that the system is also undergoing a first-order phase transition to the superfluid Efimov liquid.

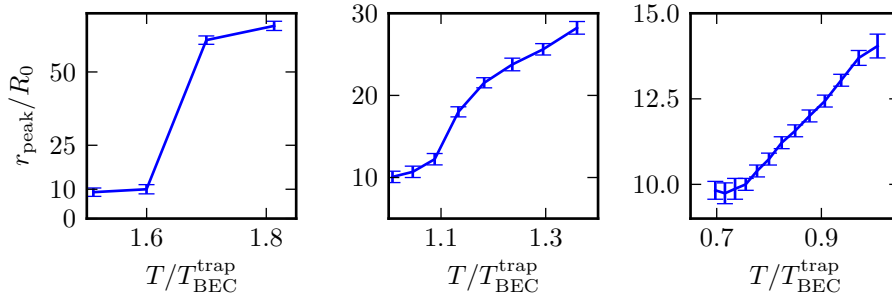


Figure 4.7: Position of the first peak of the pair distribution  $r_{\text{peak}}$  as a function of the temperature. At  $R_0/l_\omega = 0.07$  (*left*), the presence of a strong step corresponds to the case where the first-order phase transition is identifiable through the joint distribution of the distance of the centre of mass and the pair distance of pairs of particles in the trap (see Fig. 4.3). At  $R_0/l_\omega = 0.13$  (*centre*), a clear step still indicates that the unitary Bose gas undergoes a first-order phase transition although this behaviour is unclear from the joint distribution (see Fig. 4.6). At  $R_0/l_\omega = 0.23$ , there is no step and the system does not undergo a first-order phase transition (see Fig. 4.5).

### Numerical phase diagram for trapped unitary bosons

Monitoring the first-order phase transition as explained in the above section, together with monitoring conventional Bose–Einstein condensation through the length of permutation cycles, we obtained a numerical phase diagram for 100 trapped unitary bosons (see Fig. 4.8). The unitary Bose gas may be found under three thermodynamic phases: the normal gas, well characterized by the virial expansion (see Section 4.1.2), the conventional Bose–Einstein condensate, and the Efimov liquid, whose long permutation cycles also demonstrate the superfluid nature. When the temperature is decreased, the normal gas may undergo a transition to either the superfluid Efimov liquid (first-order) or the conventional Bose–Einstein condensate (second-order), that we characterize by a particle having probability greater than 0.05 to be in a cycle of length greater than 10. From that phase, a coexistence line with the superfluid Efimov liquid ends in a critical point, that is allowed by the superfluid nature of both the conventional Bose–Einstein condensate, and of the Efimov liquid.

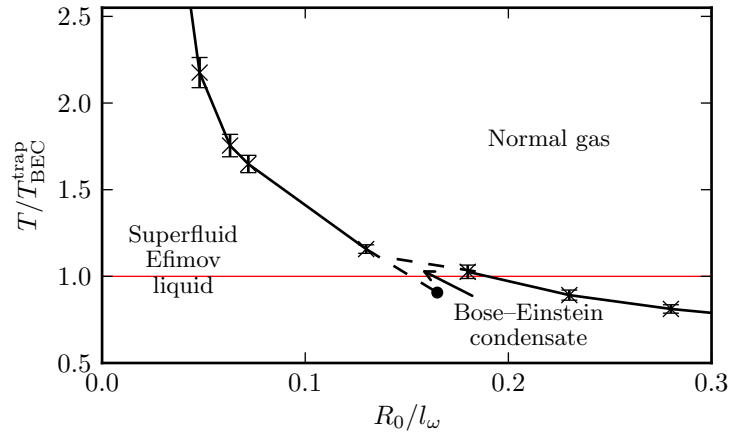


Figure 4.8: Numerical phase diagram for 100 trapped bosons. Crosses denote either normal-gas-to-Efimov-liquid transitions, or normal-gas-to-Bose–Einstein-condensate transitions, and the error bars correspond to the lowest temperature at which a pure normal gas was observed and to the highest temperature at which a superfluid phase was observed. The coexistence lines are *qualitatively* continued to a triple point and a critical point (*dashed lines*). The temperature of condensation of a free Bose–Einstein condensate in the trap,  $T_{\text{BEC}}^{\text{trap}}$  is indicated for comparison purposes (*thin horizontal red line*).

## 4.2.2 Simple model for the transition to the Efimov liquid phase

To obtain an approximate theoretical description of the normal-gas-to-Efimov liquid coexistence line, we need a simple model both of the normal gas and of the superfluid Efimov liquid. We already showed that the virial expansion up to the third coefficient is a very good model for the former (see Section 4.1.2). In order to build this simple model for the coexistence line, we devised a simple theoretical model of the Efimov liquid, both from previous work achieved in the field of unitary bosons, and from our observations.

### Energy of the superfluid Efimov liquid

In 2010, in a pioneering article, using a variational Monte Carlo method, [von Stecher](#) demonstrated that, at zero temperature, small groups of unitary bosons form clusters bound by the Efimov effect, and obtained their energy. Using the data of this article, by identifying these clusters to the superfluid Efimov liquid at low temperature, it is possible to extrapolate the bulk energy of the Efimov liquid (see Fig. 4.9) to

$$\epsilon_l = -\frac{E_l}{N} = 10.1E_T, \quad (4.12)$$

where  $-E_T$  is the energy of the fundamental Efimov trimer.

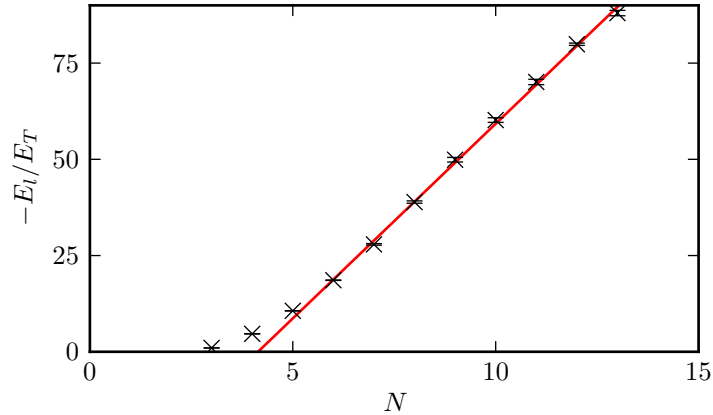


Figure 4.9: Energy  $E_l$  of the superfluid Efimov liquid at zero temperature as a function of the number of particles  $N$ , from von Stecher (2010) (black crosses). A linear regression (red line) gives  $-E_l/N = 10.1E_T$  for large values of  $N$ .

### Incompressible fluid approximation

In Section 4.2.1, we saw that, in the liquid phase, the first peak of the pair correlation function is at distances of order  $10R_0$  (see Fig. 4.3, 4.5, and 4.7), regardless of the value of  $R_0$ . This allows to model the superfluid Efimov liquid by a incompressible fluid of density  $n_l \propto R_0^{-3}$ . From simulations, we obtain  $n_l \sim (5R_0)^{-3}$ .

When the entropic contribution to the free energy of the liquid can be neglected (this holds in particular at low temperatures and for an equilibrium with a gaseous phase, such as that happening in the first-order phase transition which we are studying), the free energy is identical to the internal energy. As, in a pure phase, the Gibbs free energy per particle corresponds to the chemical potential, we may write:

$$G_l = \mu_l N = F_l + PNv_l = -N\epsilon_l + PNv_l, \quad (4.13)$$

where  $v_l = 1/n_l$  is the specific volume of the superfluid Efimov liquid,  $F_l$  its free energy,  $G_l$  its Gibbs free energy, and  $\mu_l$  its chemical potential.

This allows to write the grand-canonical equation of state of the superfluid liquid phase in the incompressible fluid approximation,

$$P = n_l(\mu_l + \epsilon_l). \quad (4.14)$$

### First-order phase transition

In the case where the free energy  $F$  of a homogeneous system is not a convex function of its volume  $V$ , it becomes more favourable to split the system into two homogeneous phases. These two phases must have equal temperatures (thermal equilibrium), pressures (mechanical equilibrium), and chemical potentials (chemical equilibrium). This picture is

valid when interface energy may be neglected, which we assume in the modelling of the phase transition to the Efimov liquid phase. The case of the equilibrium between the normal gas in the virial approximation and the superfluid liquid in the incompressible fluid approximation is illustrated in Fig. 4.10.

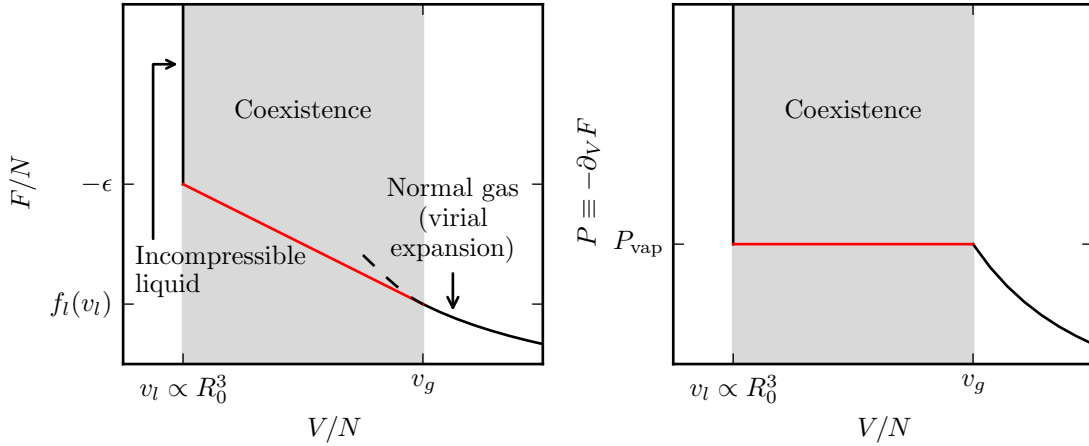


Figure 4.10: Sketch of the behaviour of the free energy (*left*) and pressure (*right*) of the unitary Bose gas through the normal-gas-to-Efimov-liquid phase transition. At coexistence, the free energy  $F$  is not identical to its convex envelope, and the slope of the convex envelope is identical to the pressure of both phases, called the saturating vapour pressure  $P_{\text{vap}}$ . When the specific volumes  $v_l$  and  $v_g$  of the liquid and of the gas become equal, coexistence ceases to be possible and there is no longer a phase transition between the two phases. This corresponds to the critical point.

### Comparison of the model to the numerical phase diagram

As we just saw, the equilibrium of the normal gas and the superfluid Efimov liquid is given by the equality of the pressures, of the temperature, and of the chemical potentials of both phases. If we use the virial expansion to describe the normal gas and the incompressible fluid model to describe the Efimov liquid, Eq. 4.8 and 4.14 read

$$n_l (\mu(T) + \epsilon_l) = \frac{k_B T}{\lambda_{\text{th}}^3} (e^{\beta\mu(T)} + b_2 e^{2\beta\mu(T)} + b_3 e^{3\beta\mu(T)}). \quad (4.15)$$

Because, at the threshold of the transition, bosons are in the gaseous phase throughout the trap, it is possible to use the density of the gas phase  $n_g$ , given by Eq. 4.8 in the virial approximation, to obtain the equilibrium chemical potential  $\mu(T)$ . In the local density approximation (see Section 2.1.2), integrating the density throughout the trap gives the

total number of particles, yielding the implicit equation for  $\mu(T)$

$$4\pi \int_0^\infty r^2 dr n_g \left( \mu(T) - \frac{1}{2} m \omega^2 r^2 \right) = N. \quad (4.16)$$

Solving Eq. 4.15 for  $T$ , where  $\mu(T)$  is given by Eq. 4.16, yields the temperature of co-existence of the two phases. In Fig. 4.11, where  $\epsilon_l$  was empirically reduced to  $-8E_T$  to account for the deviation of the energy of small unitary clusters from its large- $N$  value (see Fig. 4.9), we see that the obtained temperatures match the numerical phase diagram very well.

When the virial expansion no longer holds in the gaseous phase, and when the transition to the Efimov liquid occurs from the Bose–Einstein condensate, neither Eq. 4.15 nor Eq. 4.16 are valid any longer. However, because all physical quantities are continuous through Bose–Einstein condensation, the solution of Eq. 4.15 is continued to these regimes, where it still conveys *qualitative* information up to the critical point, where both phases have the same specific volume.

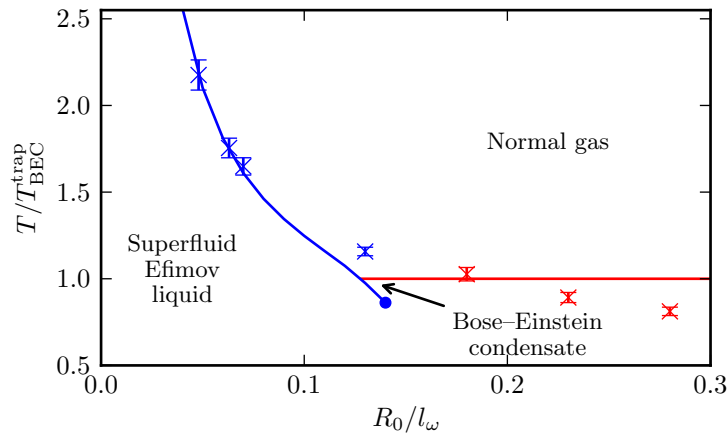


Figure 4.11: Comparison of the numerical data for the normal-gas-to-Efimov-liquid phase transition (*blue crosses*) to the simple model of Eq. 4.15 (*blue line*). The Bose–Einstein transition (*red crosses*) is naively modelled by that of the free Bose gas (*red line*).

### 4.2.3 Homogeneous phase diagram

In this section, I use the simple theoretical model for the normal-gas-to-Efimov-liquid transition, that we derived in the previous section, to describe the physics of a homogeneous system at the thermodynamic limit.

#### Diagram in terms of pressure and temperature

In the canonical ensemble, the thermodynamics of the homogeneous unitary Bose gas is described in terms of two independent thermodynamic quantities, that may be chosen to

be the pressure  $P$  and the temperature  $T$ . When the non-universality of the fundamental Efimov trimer may be neglected (see Section 3.2.4), the system is driven by one only parameter, that may be chosen to be the hyperradial cutoff  $R_0$ , or  $\epsilon_l$ . This means that only two independent dimensionless quantities may be built, in terms of which the phase diagram is universal in that it does not depend on  $R_0$ . For example, we may choose them to be the dimensionless pressure  $\tilde{P}$  and temperature  $\tilde{T}$ ,

$$\begin{cases} \tilde{T} = \frac{k_B T}{\epsilon_l}, \\ \tilde{P} = \frac{P \hbar^3}{\sqrt{m \epsilon_l^5}}. \end{cases} \quad (4.17)$$

To treat the case of the homogeneous unitary gas, there is no need to define a chemical potential, and it is possible to use the virial expansion Eq. 4.7 to obtain the relation between the pressure and the density instead of the cluster expansion Eq. 4.8. However, in the degenerate regime, where the cluster expansion was qualitatively continued, both expansions yield different coexistence curves, because of the appearance of terms of order higher than 3 when the cluster equation for the density is used together with the cluster equation for the pressure (see Eq. 4.8).

In the aim of being consistent with the coexistence line for the trapped system of 100 bosons, the transition line into the superfluid liquid is computed parametrically using the cluster expansion: Eq. 4.15 is solved for  $\mu$  at a given value of  $T$ , which gives the value of the saturating vapour pressure from, for example, the equation of state of the superfluid liquid Eq. 4.14.

As in the homogeneous phase diagram (see Fig. 4.11), the transition curve into the Bose–Einstein condensate is naively modelled by that of a free Bose gas (Huang, 1987):

$$P_{\text{BEC}}(T) = \frac{k_B T}{\lambda_{\text{th}}^3} g_{5/2}(1) \approx 0.085 \frac{m^{3/2}}{\hbar^3} (k_B T)^{5/2}, \quad (4.18)$$

where  $g_{5/2}$  is the polylogarithm function of order 5/2, defined by

$$g_{5/2}(z) = \sum_{k=1}^{\infty} \frac{z^k}{k^{5/2}}. \quad (4.19)$$

Alternatively, this equation may be rewritten in terms of the dimensionless pressure and temperature:

$$\tilde{P}_{\text{BEC}} = 0.085 \tilde{T}^{5/2}. \quad (4.20)$$

The universal phase diagram in terms of dimensionless pressure and temperature is displayed in Fig. 4.12. At high pressure and temperature, the gas is in its normal phase. Depending on the pressure, when the temperature is decreased, the system may undergo a transition to the Efimov liquid (low pressure), to the Bose–Einstein condensate and then to the Efimov liquid (intermediate pressure), or to the critical phase (high pressure).

This phase diagram also presents non-universal features, in the sense that they are specific to our model. At high temperature, the three-body hard core is assumed to block quantum coherence when the thermal wave-length  $\lambda_{\text{th}}$  is much smaller than  $R_0$ , and at very high pressure, the system is expected to be in a solid phase driven by steric effects.

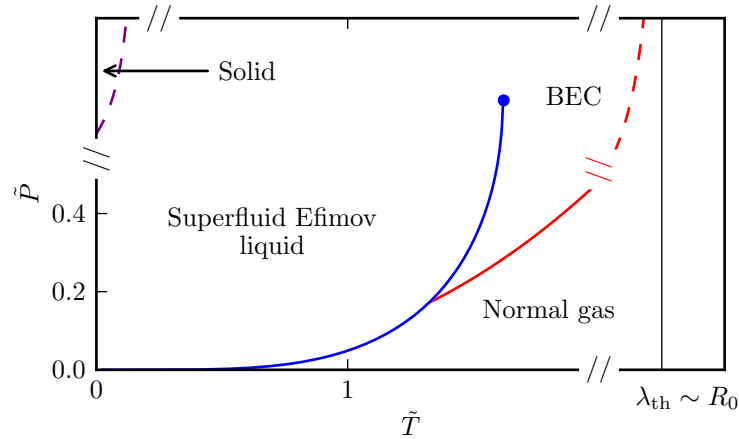


Figure 4.12: Universal phase diagram of the unitary Bose gas, expressed in terms of the dimensionless temperature and pressure. The unitary Bose gas exists under three phases, the normal gas, the Bose–Einstein condensate and the Efimov liquid. Both latter phases are superfluid and they are separated by a critical point. At high temperature, quantum coherence cannot be built, because the thermal wave-length becomes smaller than  $R_0$ , and unitary bosons are found only in the normal gas phase. At high pressure, unitary bosons are in a solid state.

### Densities diagram

Alternatively, and more conveniently for experiments, in which the density  $n$  may be accessed by *in situ* imaging (see Section 2.2.2), the two independent dimensionless physical quantities that govern the unitary Bose gas may be chosen to be  $\lambda_{\text{th}}n^{1/3}$  and  $R_0n^{1/3}$  (see Fig. 4.13).

This diagram also provides a way to view phase separation at coexistence: at constant values of  $R_0$  and  $T$ , from a density  $n$  in the coexistence region, the gas phase-separates along a line going through the origin and the point  $(\lambda_{\text{th}}n^{1/3}, R_0n^{1/3})$ . The densities of the liquid and of the gas at coexistence are given by the crossings of this line and each of the two borders of the phase-separation region.

## 4.3 Unitary liquid in experimental systems

In the previous sections, I presented the results of the simulation of 100 trapped unitary bosons, and deduced a universal phase diagram from them. In the following, I first discuss

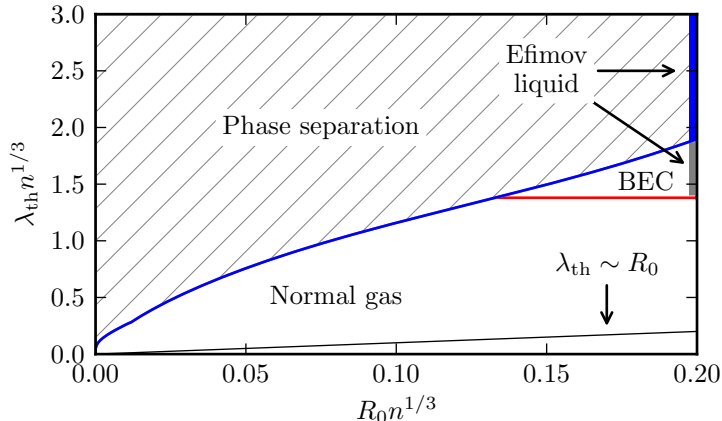


Figure 4.13: Phase diagram of unitary bosons expressed in terms of densities. This corresponds to the same data as Fig. 4.12. When the temperature is decreased and  $R_0$  and  $n$  kept fixed, from the normal gas, the system either phase-separates into the normal gas and the Efimov liquid, or undergoes a second-order phase transition to the Bose–Einstein condensate and then phase separates or undergoes a cross-over into the Bose–Einstein condensate and the Efimov liquid.

the regions of the universal phase diagram that should be accessible in experiments, and I then describe how the Efimov liquid could be characterized.

### 4.3.1 Experimentally accessible regions of the phase diagram

To discuss how the superfluid Efimov liquid could be experimentally observed, I relate the three-body hard-core parameter  $R_0$  to experimental physical quantities. I then use realistic values of experimental parameters to discuss the region of the phase diagram that could be probed in current-day experiments.

#### Connection between $R_0$ and the Van der Waals length

It was recently observed in experiments with various atomic species (Ferlaino *et al.*, 2011; Berninger *et al.*, 2011; Wild *et al.*, 2012; Roy *et al.*, 2013) that the scattering length at which Efimov trimers form scales with their van der Waals length,

$$l_{\text{vdW}} = \frac{1}{2} \left( \frac{mC_6}{\hbar^2} \right)^{1/4}, \quad (4.21)$$

where  $C_6$  is the coefficient describing the long-range behaviour of the Lennard–Jones pair-interaction potential  $V_{\text{vdW}} \rightarrow -C_6/r^6$ , the reference model for interaction between neutral atoms. This relation was also found from theoretical calculations (Schmidt *et al.*, 2012). Because universal Efimov theory depends on one unique scaling factor (see Section 3.2.4),

this also means that, if the non-universal deviations of the fundamental trimer can be neglected, the effective value of  $R_0$  describing actual atomic species is related to  $l_{\text{vdW}}$ .

As explained in Section 3.2.4, there is no reason why the fundamental Efimov trimer of the Lennard–Jones interaction potential should look like a universal trimer. However, recent computations showed that the fundamental trimer of unitary particles with such an interaction looks like a universal Efimov trimer with an effective infinite barrier at  $R \sim 2l_{\text{vdW}}$  (Wang *et al.*, 2012). This means that, for cold atoms, the value of  $R_0$  may be well approximated by

$$R_0 \sim 2l_{\text{vdW}}. \quad (4.22)$$

### Case of ultra-cold alkali vapours

Cold-atomic Bose–Einstein condensation is best performed with alkali atoms, the largest of which is  $^{133}\text{Cs}$  with  $l_{\text{vdW}} = 101a_0$ , where  $a_0 = 5.292 \times 10^{-12}\text{m}$  is the Bohr radius (Chin *et al.*, 2010). If we bring weakly-interacting  $^{133}\text{Cs}$  atoms to the free Bose–Einstein condensation temperature at the typical density  $n = 10^{13}\text{cm}^{-3}$ , and then quench them to unitarity through a Feshbach resonance, we see from Fig. 4.14 that they would spontaneously phase-separate into the Efimov liquid and the normal gas. Having a smaller value of  $l_{\text{vdW}}$  than  $^{133}\text{Cs}$ , gases of any other alkali atoms commonly used for Bose–Einstein condensation would be even deeper in the phase separation region.

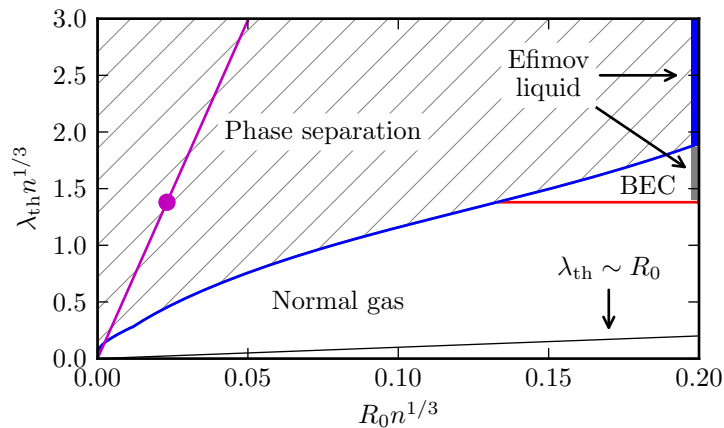


Figure 4.14: At the free Bose–Einstein condensation temperature and at the typically achieved density  $n = 10^{13}\text{cm}^{-3}$ , the gas of  $^{133}\text{Cs}$  atoms is in the phase coexistence region (*magenta dot*). It spontaneously phase separates into the normal gas and the Efimov liquid (intersections of the magenta line with the blue lines, one of which is out of the depicted region of the phase diagram).

When the gas is forced to a density  $n = 10^{13}\text{cm}^{-3}$ , it spontaneously phase-separates into the Efimov liquid of density  $n_l$  and the normal gas at its density of coexistence  $n_{\text{vap}}$ .

The volume conservation reads

$$\frac{1}{n} = \frac{x_l}{n_l} + \frac{1 - x_l}{n_{\text{vap}}}, \quad (4.23)$$

where  $x_l$  is the fraction of atoms in the liquid phase. Because  $n_{\text{vap}} \ll n_l$ , the value of  $x_l$  is

$$x_l = 1 - \frac{n_{\text{vap}}}{n}. \quad (4.24)$$

As  $n_{\text{vap}} \ll n$  (see Fig. 4.14) at the free Bose–Einstein transition temperature, the liquid fraction after the quench has to be very large. As the quench drives the gas deep into the region where the liquid is stable, there should be no free-energy barrier hampering the transition and the liquid should form through spinodal decomposition rather than a slow nucleation process (Binder, 1987).

### 4.3.2 Experimental observables

The phase separation of the unitary Bose gas described in the above paragraph is unlikely to be observed at thermal equilibrium, as three-body losses make the unitary Bose gas unstable. However, as discussed in the following, they could still be used to identify the Efimov liquid. I then discuss another possible experimental observable, the momentum distribution.

#### Three-body losses

In atomic alkali gases, the pair-interaction potential features deeply-bound dimer states which our interaction potential lacks. These cause three-body recombination processes, in which three atoms come close to one another, two of which form a deeply-bound dimer while the third atom carries the kinetic energy away. This process causes all three particles to leave the trap. The three-body losses are the same as those through which Efimov trimers were experimentally identified (Kraemer *et al.*, 2006; Zaccanti *et al.*, 2009; Pollack *et al.*, 2009).

After a recombination event, the density of particles  $n(t)$  in the trap decreases with the time  $t$  following the equation

$$\frac{dn(t)}{dt} \propto -K_3 n^3, \quad (4.25)$$

where  $K_3$  is called the *three-body recombination rate*. It was shown both experimentally and numerically that  $K_3$  is on the order of  $\hbar|a|^3/m$  and saturates as  $|a|$  reaches the order of the de Broglie thermal wave-length  $\lambda_{\text{th}}$  (Greene *et al.*, 2004; D’Incao *et al.*, 2004; Rem *et al.*, 2013).

Four-body processes, in which three bosons form a (possibly meta-stable) trimer and the fourth leaves the trap carrying the kinetic energy, are one possible way to form the Efimov liquid. They may be described by a four-body recombination rate  $K_4$ , so that the time variation of the density of free atoms is proportional to  $K_4 n^4$ . Theoretical models predict that  $K_4$  is on the order of  $\hbar a^7/m$  and, like  $K_3$ , thermally saturates when  $|a| \sim \lambda_{\text{th}}$ .

At unitarity, both the three and four-body recombination rates are thermally saturated. The condition for four-body losses to dominate over three-body losses is

$$nK_4 \gg K_3, \quad (4.26)$$

which may be re-written as

$$n\lambda_{\text{th}}^3 \gg 1. \quad (4.27)$$

This condition is similar to that for the Bose–Einstein condensation of free atoms (Eq. 1.12). Therefore, quenching a Bose–Einstein condensed atomic vapour to unitarity at a Feshbach resonance may be a way to form the Efimov liquid.

Because of the three-body losses, that still would be present, full phase separation is however unlikely to be observed. Nevertheless, the formation of small liquid droplets may be a quite realistic scenario. These might be identified through the sudden increase of the losses, quite more important in the liquid phase as they are proportional to  $n_l^3$ .

### Momentum distribution

Even though only small droplets of liquid may form, the signature of the liquid fraction in terms of the momentum distribution  $n(k)$  might be obtained from time-of-flight measurements. This was recently done to some extent by Makotyn *et al.* (2014), with a good signal in the low- $k$  region. Nevertheless, the current lack of model or data for  $n(k)$  at unitarity makes it difficult to state whether their system (a gaseous phase) is fully thermalized, and the characteristic unitary  $1/k^4$  tail of the momentum distribution (see Tan (2008) and Section 4.A.2) has yet not been observed.

In path-integral Monte Carlo simulations, the momentum distribution may be obtained through the off-diagonal density matrix elements (Ceperley, 1995), a process detailed in Section 4.A. This is done by stochastically alternating between diagonal configurations such as those in the simulations performed in this work (see Chapter 1), in which all bosons lie on closed paths starting at their positions and ending at those of their permutations, and non-diagonal configurations, in which one path is open. There is a wide variety of complexity in off-diagonal simulations, ranging from simply allowing one cycle to open (Holzmann *et al.*, 1999), to the complex worm algorithm (Prokof'ev *et al.*, 1996; Prokof'ev *et al.*, 1998), in which the two ends of the open cycle do not have to always be at the same imaginary time.

## 4.4 Conclusion

In this chapter, I have explained how the simulations show that the unitary Bose gas exists under three phases: the normal gas, the conventional Bose–Einstein condensate, and a new phase, the Efimov liquid. I also discussed the prospects of experimental observation and quantitative comparison to experiments, with the challenging problem of three-body losses at unitarity.

The simulation can further be enhanced by sampling the pair density matrix of bosons interacting through the zero-range unitary pair potential rejection-free, which is the subject of ongoing research. This may lead to a simulation able to sample a large liquid drop and to address systems of more than 100 bosons.

## Appendix 4.A Path integrals and momentum distribution

As explained in Section 4.3.2, the momentum distribution of a cold-atomic gas is an experimentally accessible observable, that can also be computed in a path-integral Monte Carlo simulation sampling the off-diagonal density matrix. Here, I explain the link between the off-diagonal density matrix and the momentum distribution, which I then illustrate by deriving the momentum distribution of two bosons and obtaining its characteristic  $1/k^4$  tail due to unitary interactions. I then describe a simple algorithm for computing both diagonal and off-diagonal density matrix elements (and hence momentum distributions) in a path-integral Monte Carlo simulation.

### 4.A.1 Off-diagonal density matrix and momentum distribution

When the density matrix is diagonal, the path starting at particle  $i$  at imaginary time 0 ends in  $\mathbf{x}_{P(i)}$ , the position of particle  $P(i)$  (see Chapter 1), at imaginary time  $\beta$ . For non-diagonal density matrix elements, the end of this path,  $\mathbf{x}'_i$ , is in general different from  $\mathbf{x}_{P(i)}$ . Such a situation happens, for example, when the path is open between  $\mathbf{x}_1$  and  $\mathbf{x}_{P^{-1}(1)}$ , as illustrated in Fig. 4.15.

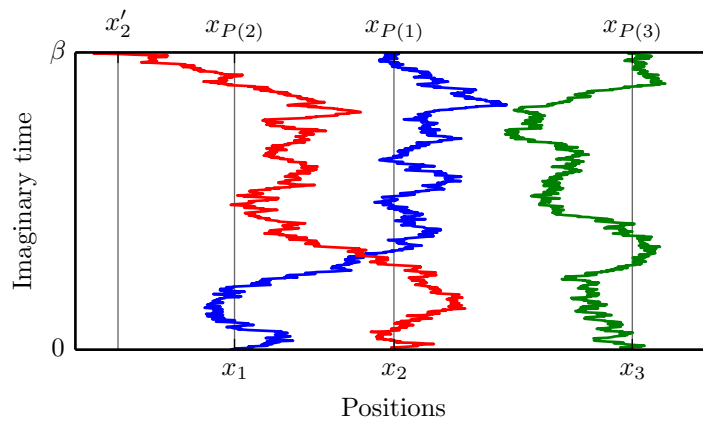


Figure 4.15: One-dimensional path-integral configuration with  $P(2) = 1$  (or alternatively  $P^{-1}(1) = 2$ ) in which the diagonal condition  $\mathbf{x}'_{P^{-1}(1)} = \mathbf{x}_1$  has been released.

By symmetry, it is enough to compute the momentum distribution of particle 1. Let  $\mathbf{k}_1$  be its momentum. In the diagonal density matrix  $\rho(\mathbf{x}_1, \dots, \mathbf{x}_N; \mathbf{x}_{P(1)}, \dots, \mathbf{x}_{P(N)}; \beta)$ ,  $\mathbf{x}_1$  appears twice: as  $\mathbf{x}_1$ , and as  $\mathbf{x}'_{P^{-1}(1)}$ , that is, as the position at imaginary time  $\beta$  of the predecessor of particle 1 in the permutation. Using that the momentum is the Fourier transform of the position, the momentum distribution is

$$n(\mathbf{k}_1) = \frac{1}{(2\pi)^3 Z} \sum_{P \in S_N} \int d\mathbf{x}_1 d\mathbf{x}_2 \dots d\mathbf{x}_N d\mathbf{x}'_{P^{-1}(1)} e^{-i\mathbf{k}_1 \cdot (\mathbf{x}'_{P^{-1}(1)} - \mathbf{x}_1)} \rho(\mathbf{x}_1, \dots, \mathbf{x}_N; \mathbf{x}'_1, \dots, \mathbf{x}'_N; \beta), \quad (4.28)$$

where  $Z = \text{tr } \rho$  is the partition function of the system. In this integral,  $\mathbf{x}'_{P^{-1}(i)} = \mathbf{x}_i$  for  $i \neq 1$ .

In an off-diagonal simulation, the momentum distribution  $n(\mathbf{k}_1)$  is thus obtained by taking the Fourier transform of  $\mathbf{x}'_{P^{-1}(1)} - \mathbf{x}_1$ , which are both ends of the open path. This means that, in practice, it is possible to forget about the indices and simply observe the pair distance distribution between both open ends of the open path (Ceperley, 1995).

#### 4.A.2 Momentum distribution of two interacting bosons

To illustrate that it is possible to obtain momentum distributions using density matrices, in this section, I compute the momentum distribution of two unitary bosons. In this analytical calculation, the sum on permutations (see Eq. 4.28) needs to be carried out explicitly. In the following, I derive independently the contributions of the configuration where the two particles are on independent permutation cycles (the ‘‘classical’’ contribution) and of that where they are on the same permutation cycle (the ‘‘entangled’’ configuration).

##### Classical contribution

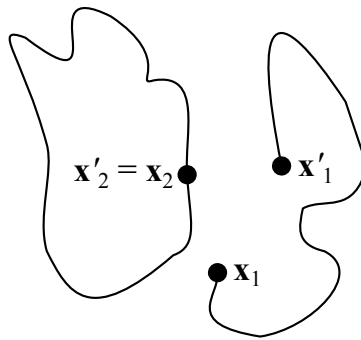


Figure 4.16: Two-dimensional sketch of the configuration used to compute  $n_{\text{cl}}(\mathbf{k}_1)$ . Positions at imaginary times 0 and  $\beta$  are identified by black dots, and plain lines show paths between 0 and  $\beta$ .

From Section 4.A.1, the classical contribution to the momentum distribution (illustrated

in Fig. 4.16) is

$$n_{\text{cl}}(\mathbf{k}_1) = \frac{1}{Z(2\pi)^3} \int d\mathbf{x}_1 d\mathbf{x}'_1 d\mathbf{x}_2 \rho(\mathbf{x}_1, \mathbf{x}_2; \mathbf{x}'_1, \mathbf{x}_2; \beta) e^{-i\mathbf{k}_1 \cdot (\mathbf{x}'_1 - \mathbf{x}_1)}. \quad (4.29)$$

For quantities to be easier to compute, the diagonality of particle 2 may be released by noting that

$$n_{\text{cl}}(\mathbf{k}_1) = \frac{1}{(2\pi)^6 Z} \int d\mathbf{k}_2 d\mathbf{x}_1 d\mathbf{x}_2 d\mathbf{x}'_1 d\mathbf{x}'_2 \rho(\mathbf{x}_1, \mathbf{x}_1; \mathbf{x}'_1, \mathbf{x}'_2; \beta) e^{-i\mathbf{k}_1 \cdot (\mathbf{x}'_1 - \mathbf{x}_1) - i\mathbf{k}_2 \cdot (\mathbf{x}'_2 - \mathbf{x}_2)} \quad (4.30)$$

$$= \int d\mathbf{k}_2 n_{\text{cl}}(\mathbf{k}_1, \mathbf{k}_2). \quad (4.31)$$

In practice, it is easier to compute  $n_{\text{cl}}(\mathbf{k}_1, \mathbf{k}_2)$  and then integrate  $\mathbf{k}_2$  out. To this end, let us separate the relative motion from that of the centre of mass. If  $\mathbf{r} = \mathbf{x}_2 - \mathbf{x}_1$  and  $\mathbf{r}' = \mathbf{x}'_2 - \mathbf{x}'_1$  are the separations between particles 1 and 2 respectively at imaginary times 0 and  $\beta$ , and  $\mathbf{C} = (\mathbf{x}_1 + \mathbf{x}_2)/2$  and  $\mathbf{C}' = (\mathbf{x}'_1 + \mathbf{x}'_2)/2$  are the corresponding coordinates of the centre of mass of particles 1 and 2,  $n_{\text{cl}}(\mathbf{k}_1, \mathbf{k}_2)$  may be rewritten

$$Z n_{\text{cl}}(\mathbf{k}_1, \mathbf{k}_2) = \underbrace{\frac{1}{(2\pi)^3} \int d\mathbf{C} d\mathbf{C}' \rho_{\text{CM}}(\mathbf{C}, \mathbf{C}'; \beta) e^{-i\mathbf{K} \cdot (\mathbf{C}' - \mathbf{C})}}_{n_{\text{cl}}(\mathbf{K}), \text{ contribution of centre of mass}} \underbrace{\frac{1}{(2\pi)^3} \int d\mathbf{r} d\mathbf{r}' \rho_{\text{rel}}(\mathbf{r}, \mathbf{r}'; \beta) e^{-i\mathbf{k} \cdot (\mathbf{r}' - \mathbf{r})}}_{n_{\text{cl}}(\mathbf{k}), \text{ contribution of the relative motion}}, \quad (4.32)$$

where  $\rho_{\text{CM}}$  and  $\rho_{\text{rel}}$  are the respective density matrices of the centre of mass and of the relative motion and  $\mathbf{K} = \mathbf{k}_1 + \mathbf{k}_2$  and  $\mathbf{k} = (\mathbf{k}_2 - \mathbf{k}_1)/2$  their respective momenta.

**Computation of  $n_{\text{cl}}(\mathbf{K})$**  We know that  $n_{\text{cl}}(\mathbf{K})$  is the momentum distribution of a free particle of mass  $2m$ , and from the free density matrix (see Eq. 1.5):

$$n_{\text{cl}}(\mathbf{K}) = \frac{V}{(2\pi)^3} \exp \left[ -\beta \frac{\hbar^2 K^2}{4m} \right], \quad (4.33)$$

where  $V$  is the accessible volume.

**Computation of  $n_{\text{cl}}(\mathbf{k})$**  We know that the relative density matrix of two particles interacting with a unitary potential is given by the free relative density matrix multiplied by the correction factor  $g_\infty$  (see Eq. 3.16), that is, if  $\mathbf{r} = \mathbf{x}_2 - \mathbf{x}_1$  and  $\mathbf{r}' = \mathbf{x}'_2 - \mathbf{x}'_1$ :

$$\rho_{\text{rel}}(\mathbf{r}, \mathbf{r}'; \beta) = \left( \frac{m}{4\pi\hbar^2\beta} \right)^{3/2} \exp \left[ -\frac{m(\mathbf{r}' - \mathbf{r})^2}{4\hbar^2\beta} \right] g_\infty(\mathbf{r}, \mathbf{r}'; \beta) \quad (4.34)$$

$$= \left( \frac{m}{4\pi\hbar^2\beta} \right)^{3/2} \left\{ \exp \left[ -\frac{m(\mathbf{r}' - \mathbf{r})^2}{4\hbar^2\beta} \right] + \frac{2\beta\hbar^2}{mrr'} \exp \left[ -\frac{m(r+r')^2}{4\hbar^2\beta} \right] \right\}. \quad (4.35)$$

The first term in the sum in Eq. 4.35 corresponds to the momentum distribution of a free particle of mass  $m/2$ . The corresponding contribution to  $n_{\text{cl}}(\mathbf{k})$  is therefore

$$n_{\text{cl}}^{\text{free}}(\mathbf{k}) = \frac{V}{(2\pi)^3} \exp \left[ -\frac{\beta \hbar^2 k^2}{m} \right]. \quad (4.36)$$

We now compute the contribution of the second term in Eq. 4.35 to the momentum distribution of the relative motion,  $\Delta n_{\text{cl}}(\mathbf{k})$ :

$$\Delta n_{\text{cl}}(\mathbf{k}) = \frac{1}{(2\pi)^4} \sqrt{\frac{m}{4\pi \hbar^2 \beta}} \int \frac{d\mathbf{r} d\mathbf{r}'}{rr'} \exp \left[ -\frac{m(r+r')^2}{4\hbar^2 \beta} - i\mathbf{k} \cdot (\mathbf{r}' - \mathbf{r}) \right]. \quad (4.37)$$

If  $\mathbf{k}$  is used to define the  $z$  direction, we may use the spherical coordinates  $(r, \theta, \phi)$  (resp.  $(r', \theta', \phi')$ ) associated to  $\mathbf{r}$  (resp.  $\mathbf{r}'$ ). We obtain

$$\Delta n_{\text{cl}}(\mathbf{k}) = \frac{1}{(2\pi)^2} \sqrt{\frac{m}{4\pi \hbar^2 \beta}} \int_0^\infty rr' dr dr' e^{-\frac{m(r+r')^2}{4\hbar^2 \beta}} \int_0^\pi d\theta d\theta' \sin \theta \sin \theta' e^{-ik \cdot (r' \cos \theta' - r \cos \theta)}. \quad (4.38)$$

The integrals on  $\theta$  and  $\theta'$  are straightforward and give:

$$\Delta n_{\text{cl}}(k) = \frac{1}{2(\pi k)^2} \sqrt{\frac{m}{4\pi \hbar^2 \beta}} \int_0^\infty dr dr' [\cos(k(r' - r)) - \cos(k(r + r'))] \exp \left[ -\frac{m(r+r')^2}{4\beta \hbar^2} \right]. \quad (4.39)$$

Using the change of variables  $u = (r + r')/2$  and  $v = r' - r$ , we obtain:

$$\Delta n_{\text{cl}}(k) = \frac{1}{2(\pi k)^2} \sqrt{\frac{m}{4\pi \hbar^2 \beta}} \left[ \underbrace{\int_0^\infty du \int_{-2u}^{2u} dv e^{-mu^2/\beta \hbar^2} \cos(kv)}_{I_1} \right] \quad (4.40)$$

$$- \underbrace{\int_0^\infty du \int_{-2u}^{2u} dv e^{-mu^2/\beta \hbar^2} \cos(2ku)}_{I_2}. \quad (4.41)$$

These two integrals may be expressed in terms of the Dawson integral

$$F(x) = e^{-x^2} \int_0^x e^{t^2} dt = \frac{1}{2} \int_0^\infty e^{-t^2/4} dt \sin xt \quad (4.42)$$

as

$$I_1 = \frac{2}{k} \sqrt{\frac{\beta \hbar^2}{m}} F \left( \sqrt{\beta \frac{\hbar^2 k^2}{m}} \right) \quad (4.43)$$

and

$$I_2 = 2 \frac{\beta \hbar^2}{m} - 4k \left( \beta \frac{\hbar^2}{m} \right)^{3/2} F \left( \sqrt{\beta \frac{\hbar^2 k^2}{m}} \right). \quad (4.44)$$

Combining these two expressions into  $\Delta n_{\text{cl}}(\mathbf{k})$ , and then with Eq. 4.36 into  $n_{\text{cl}}$ , we get

$$n_{\text{cl}}(\mathbf{k}) = n_{\text{cl}}^{\text{free}}(\mathbf{k}) + \Delta n_{\text{cl}}(\mathbf{k}) \quad (4.45)$$

$$= \frac{V}{(2\pi)^3} \exp\left[-\frac{\beta\hbar^2 k^2}{m}\right] + \frac{1}{2\pi^{5/2}k^3} \left[ \left(1 + 2\beta\frac{\hbar^2 k^2}{m}\right) F\left(\sqrt{\beta\frac{\hbar^2 k^2}{m}}\right) - \sqrt{\beta\frac{\hbar^2 k^2}{m}} \right] \quad (4.46)$$

**Large- $k_1$  behaviour of the classical contribution** The full classical contribution to the single-particle momentum distribution is (see Eq. 4.32):

$$n_{\text{cl}}(\mathbf{k}_1) = \frac{1}{Z} \int d\mathbf{k}_2 n_{\text{cl}}(\mathbf{K} = \mathbf{k}_1 + \mathbf{k}_2) n_{\text{cl}}\left(\mathbf{k} = \frac{\mathbf{k}_2 - \mathbf{k}_1}{2}\right) \quad (4.47)$$

$$= \frac{V}{Z(2\pi)^3} \left[ \frac{V}{\lambda_{\text{th}}^3} \exp\left(-\beta\frac{\hbar^2 k_1^2}{2m}\right) + \int d\mathbf{k}_2 \Delta n_{\text{cl}}\left(\frac{\mathbf{k}_2 - \mathbf{k}_1}{2}\right) \exp\left(-\beta\frac{\hbar^2(\mathbf{k}_1 + \mathbf{k}_2)^2}{4m}\right) \right]. \quad (4.48)$$

This expression is exact. It may however be integrated using the saddle-point method:

$$n_{\text{cl}}(\mathbf{k}_1) = \frac{V}{Z(2\pi)^3} \left[ \frac{V}{\lambda_{\text{th}}^3} \exp\left(-\beta\frac{\hbar^2 k_1^2}{2m}\right) + \left(\frac{4\pi m}{\beta\hbar^2}\right)^{3/2} \Delta n_{\text{cl}}(\mathbf{k}_1) \right]. \quad (4.49)$$

The  $k_1 \gg \sqrt{m/(\beta\hbar^2)}$  behaviour of  $n_{\text{cl}}(\mathbf{k}_1)$  may be deduced from the Taylor series  $F(x) = \frac{1}{2x} + \frac{1}{4x^3} + O(x^{-5})$ . In this regime,

$$n_{\text{cl}}(\mathbf{k}_1) = \frac{V}{Z(2\pi)^3} \left[ \frac{V}{\lambda_{\text{th}}^3} \exp\left(-\beta\frac{\hbar^2 k_1^2}{2m}\right) + \frac{4}{\pi k_1^4} \left(\frac{m}{\beta\hbar^2}\right)^2 \right]. \quad (4.50)$$

### Entangled contribution

From Section 4.A.1, the entangled contribution to the momentum distribution (illustrated in Fig. 4.17) is

$$n_{\text{ent}}(\mathbf{k}_1) = \frac{1}{Z(2\pi)^3} \int d\mathbf{x}_1 d\mathbf{x}'_1 d\mathbf{x}_2 \rho(\mathbf{x}_1, \mathbf{x}_2; \mathbf{x}_2, \mathbf{x}'_1 \beta) e^{-i\mathbf{k}_1 \cdot (\mathbf{x}'_1 - \mathbf{x}_2)}. \quad (4.51)$$

As for the classical contribution, the condition  $\mathbf{x}'_2 = \mathbf{x}_1$  may be released, and we may compute at first  $n_{\text{ent}}(\mathbf{k}_1, \mathbf{k}_2)$ , linked to  $n_{\text{ent}}(\mathbf{k}_1)$  by the integral

$$n_{\text{ent}}(\mathbf{k}_1) = \int d\mathbf{k}_2 n_{\text{ent}}(\mathbf{k}_1, \mathbf{k}_2). \quad (4.52)$$

We also separate the centre of mass (of contribution  $n_{\text{ent}}(\mathbf{K})$ ) and the relative motion (of contribution  $n_{\text{ent}}(\mathbf{k})$ ):

$$Z n_{\text{ent}}(\mathbf{k}_1, \mathbf{k}_2) = \underbrace{\frac{1}{(2\pi)^3} \int d\mathbf{C} d\mathbf{C}' \rho_{\text{CM}}(\mathbf{C}, \mathbf{C}'; \beta) e^{-i\mathbf{K} \cdot (\mathbf{C}' - \mathbf{C})}}_{n_{\text{ent}}(\mathbf{K}), \text{ contribution of centre of mass}} \underbrace{\frac{1}{(2\pi)^3} \int d\mathbf{r} d\mathbf{r}' \rho_{\text{rel}}(\mathbf{r}, \mathbf{r}'; \beta) e^{-i\mathbf{k} \cdot (\mathbf{r} + \mathbf{r}')}}_{n_{\text{ent}}(\mathbf{k}), \text{ contribution of the relative motion}}, \quad (4.53)$$

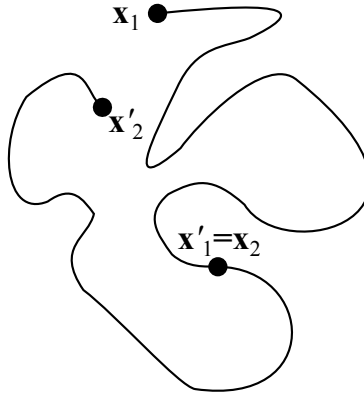


Figure 4.17: Two-dimensional sketch of the configuration used to compute  $n_{\text{ent}}(\mathbf{k}_1)$ . Positions at imaginary times 0 and  $\beta$  are identified by black dots, and plain lines show paths between 0 and  $\beta$ .

The contribution of the centre of mass is unchanged from the classical contribution. As we did above, we use that the relative unitary pair density matrix is the sum of a free contribution and a correction (see Eq. 4.35) to compute the respective contributions  $n_{\text{ent}}^{\text{free}}(\mathbf{k})$  and  $\Delta n_{\text{ent}}(\mathbf{k})$ .

$$n_{\text{ent}}^{\text{free}}(\mathbf{k}) = \frac{1}{(2\pi)^3} \left( \frac{m}{4\pi\hbar^2\beta} \right)^{3/2} \int d\mathbf{r}d\mathbf{r}' \exp \left[ -m \frac{(\mathbf{r}' - \mathbf{r})^2}{4\hbar^2\beta} - i\mathbf{k} \cdot (\mathbf{r} + \mathbf{r}') \right] \quad (4.54)$$

Using the change of variables  $\mathbf{u} = (\mathbf{r} + \mathbf{r}')/2$  and  $\mathbf{v} = \mathbf{r}' - \mathbf{r}$ , the computation is straightforward and gives

$$n_{\text{ent}}^{\text{free}}(\mathbf{k}) = \frac{\delta(\mathbf{k})}{8}, \quad (4.55)$$

where  $\delta$  is Dirac's delta function.

Since substituting  $-r$  for  $r$  in the last integral of Eq. 4.38 leaves  $\Delta n_{\text{cl}}(\mathbf{k})$  unchanged, we have  $\Delta n_{\text{ent}}(\mathbf{k}) = \Delta n_{\text{cl}}(\mathbf{k})$ . We obtained the two contributions to  $n_{\text{ent}}(\mathbf{k})$ , that we may multiply by the momentum distribution of the centre of mass to obtain  $n_{\text{ent}}(\mathbf{k}_1, \mathbf{k}_2)$ , from which  $\mathbf{k}_2$  may be integrated out to obtain  $n_{\text{ent}}(\mathbf{k}_1)$ . This yields

$$n_{\text{ent}}(\mathbf{k}_1) = \frac{V}{Z(2\pi)^3} \left[ \exp \left( -\beta \frac{\hbar^2 k_1^2}{m} \right) + \left( \frac{4\pi m}{\beta\hbar^2} \right)^{3/2} \Delta n_{\text{cl}}(\mathbf{k}_1) \right]. \quad (4.56)$$

For large values of  $k_1$ , we obtain:

$$n_{\text{ent}}(\mathbf{k}_1) = \frac{V}{Z(2\pi)^3} \left[ \exp \left( -\beta \frac{\hbar^2 k_1^2}{m} \right) + \frac{4}{\pi k_1^4} \left( \frac{m}{\beta\hbar^2} \right)^2 \right]. \quad (4.57)$$

### Overall momentum distribution

The momentum distribution is the sum of  $n_{\text{cl}}(\mathbf{k}_1)$  and  $n_{\text{ent}}(\mathbf{k}_2)$ . From Eq. 4.49 and 4.56:

$$n(\mathbf{k}_1) = \frac{V}{Z(2\pi)^3} \left[ \frac{V}{\lambda_{\text{th}}^3} \exp\left(-\beta \frac{\hbar^2 k_1^2}{2m}\right) + \exp\left(-\beta \frac{\hbar^2 k_1^2}{m}\right) + 2 \left(\frac{4\pi m}{\beta \hbar^2}\right)^{3/2} \Delta n_{\text{cl}}(\mathbf{k}_1) \right]. \quad (4.58)$$

The partition function  $Z$  may be seen as simply the normalization coefficient so that  $\int n(\mathbf{k}_1) = 1$ , and, alternatively, may be computed using the real-space density matrix.

At large values of  $k_1$ , Eq. 4.50 and 4.57 yield

$$n(\mathbf{k}_1) = \frac{V}{Z(2\pi)^3} \left[ \frac{V}{\lambda_{\text{th}}^3} \exp\left(-\beta \frac{\hbar^2 k_1^2}{2m}\right) + \exp\left(-\beta \frac{\hbar^2 k_1^2}{m}\right) + \frac{8}{\pi k_1^4} \left(\frac{m}{\beta \hbar^2}\right)^2 \right]. \quad (4.59)$$

We found the expected  $1/k_1^4$  tail of the pair distribution function, that is directly due to the unitary pair interaction (Tan, 2008).

### 4.A.3 Simple algorithm to obtain the momentum distribution

In the previous two sections, I explained how density matrices may be used to compute momentum distributions, and I derived the momentum distribution of two unitary bosons. In the following, I explain how momentum distributions may be obtained using path-integral algorithms that sample both closed and open paths. This description follows from the work of Holzmann *et al.* (1999).

#### Sampling two configuration spaces at a time

In the same simulation, it is possible to sample both the non-diagonal configuration space  $\mathcal{O}$  (that contains one open path) and the diagonal configuration space  $\mathcal{C}$  (that contains only closed paths). Configurations of both spaces are shown on Fig. 4.18. These two configuration spaces could be sampled in two independent simulations. In the simulation sampling closed paths in space  $\mathcal{C}$ , a configuration  $c$  has a statistical weight  $\pi(c)$ , and, likewise, in the simulation sampling open paths in space  $\mathcal{O}$ , a configuration  $o$  has a statistical weight  $\pi(o)$ .

In the Metropolis–Hastings algorithm (see Eq. 1.34), only ratios of probabilities are computed: in practice, the physical probabilities  $\pi$  may be multiplied by any positive constant without changing the output of the simulation. Let us consider a closed path ending in  $\mathbf{x}_c$  and an open path ending in  $\mathbf{x}_o$ , which are identical up to the point  $\mathbf{x}_i$  (see Fig. 4.18). In independent simulations, their probabilities would be given respectively by

$$\pi_c \propto \rho(\mathbf{x}_i, \dots, \mathbf{x}_c; \tau_S) \quad \text{and} \quad \pi_o \propto \rho(\mathbf{x}_i, \dots, \mathbf{x}_o; \tau_S), \quad (4.60)$$

where the part of the paths that do not differ in configurations  $c$  and  $o$  were not written. In the simulation that samples both  $\pi_c$  and  $\pi_o$ , we set the ratio  $\pi_c/\pi_o$ , by imposing

$$\frac{\pi_c}{\pi_o} = \alpha \frac{\rho(\mathbf{x}_i, \dots, \mathbf{x}_c; \tau_S)}{\rho(\mathbf{x}_i, \dots, \mathbf{x}_o; \tau_S)}, \quad (4.61)$$

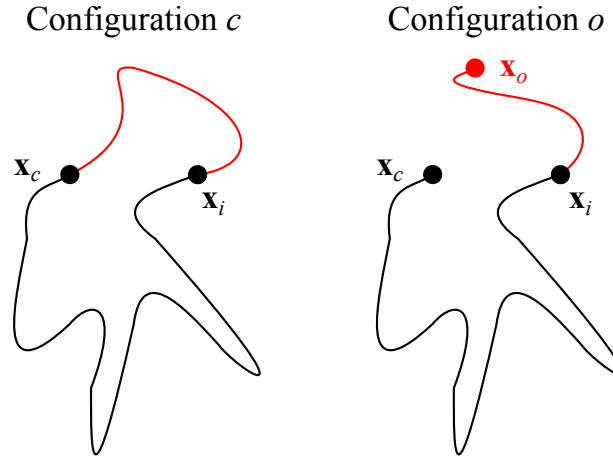


Figure 4.18: Configurations of space  $\mathcal{C}$  (left) and  $\mathcal{O}$  (right), differing only by their red parts.

that is, that the ratio of probabilities of open to closed paths is that of their statistical weights, multiplied by an arbitrary constant  $\alpha$  that sets the ratio of the configurations of space  $\mathcal{C}$  to those of space  $\mathcal{O}$ . In practice, this means that, in that simulation, the probabilities  $\pi$  may be taken as:

$$\pi_c = \alpha \rho(\mathbf{x}_i, \dots, \mathbf{x}_c; \tau_S) \quad \text{and} \quad \pi_o = \rho(\mathbf{x}_i, \dots, \mathbf{x}_o; \tau_S). \quad (4.62)$$

In moves that go from a closed configuration to another closed configuration, or from an open configuration to another open configuration, this does not affect the algorithm as probabilities may be harmlessly be multiplied by an arbitrary constant to respect detailed balance (see Eq. 1.33). Therefore, such moves may be performed like they would be in a simulation sampling only space  $\mathcal{C}$  or space  $\mathcal{O}$ .

### Moves opening or closing paths

Moves that open or close paths should satisfy the ratio  $\pi_c/\pi_o$  defined in Eq. 4.61. One way to set a detailed balance condition that satisfies this ratio is to choose

$$\mathcal{A}(o \rightarrow c) = \alpha \rho^{\text{free}}(\mathbf{x}_i, \mathbf{x}_c; \tau) \rho^{\text{free}}(\mathbf{x}_i, \dots, \mathbf{x}_c; \tau_S) \quad (4.63)$$

and

$$\mathcal{A}(c \rightarrow o) = \rho^{\text{free}}(\mathbf{x}_i, \mathbf{x}_o; \tau) \rho^{\text{free}}(\mathbf{x}_i, \dots, \mathbf{x}_o; \tau_S), \quad (4.64)$$

where  $\tau$  is the imaginary time between  $\mathbf{x}_i$  and either  $\mathbf{x}_o$  or  $\mathbf{x}_c$ . This means that moves going from configuration  $o$  to  $c$  are proposed with a probability  $\alpha \rho^{\text{free}}(\mathbf{x}_i, \mathbf{x}_c; \tau)$ . If they are proposed, the paths between  $\mathbf{x}_i$  and  $\mathbf{x}_c$  may be built following the Lévy construction (Lévy, 1940). The move is then accepted or rejected according to the standard procedure based on interaction weights (see Section 1.A).

Moves going from configuration  $c$  to configuration  $o$  are performed by sampling  $\mathbf{x}_o$  directly according to the Gaussian distribution  $\rho^{\text{free}}(\mathbf{x}_i, \mathbf{x}_o; \tau)$  (see Eq. 1.5). The path between  $\mathbf{x}_i$  and  $\mathbf{x}_o$  is then built rejection-free according to the Lévy construction, and the move is accepted or rejected according to the standard procedure based on interaction weights.

### Sampling momentum distribution

In such a simulation, that samples both open and closed paths, thermodynamic quantities may be sampled using ensemble averaging of diagonal configurations, like in purely-diagonal simulations. The momentum distribution may be extracted by performing the Fourier transform of the distribution of the distance between both ends of open paths (see Eq. 4.28).

---

## General conclusion

---

Quantum path-integral Monte Carlo simulations provide a very powerful tool to probe the low-temperature behaviour of cold bosonic gases. In this thesis, they were used to obtain the first beyond-mean-field corrections to the equation of state of the weakly-interacting Bose gas, and to address the case where the interactions between bosons are resonant, a situation called unitarity. There, they provided insights into the counter-intuitive Efimov effect, that causes three bosons to form trimers in a regime where two bosons cannot bind. Then, they were used to probe the physics of the unitary Bose gas, where they allowed to predict a phase transition to a new phase, the superfluid Efimov liquid.



---

## Bibliography

---

- Anderson, M. H., J. R. Ensher, M. R. Matthews, C. E. Wieman, and E. A. Cornell, 1995, *Science* **269**(5221), 198, URL <http://www.sciencemag.org/content/269/5221/198>.
- Barker, J. A., 1979, *Journal of Chemical Physics* **70**(6), 2914, URL [http://jcp.aip.org/resource/1/jcpsa6/v70/i6/p2914\\_s1](http://jcp.aip.org/resource/1/jcpsa6/v70/i6/p2914_s1).
- Bernard, E. P., W. Krauth, and D. B. Wilson, 2009, *Physical Review E* **80**(5), 056704, URL <http://link.aps.org/doi/10.1103/PhysRevE.80.056704>.
- Berninger, M., A. Zenesini, B. Huang, W. Harm, H.-C. Nägerl, F. Ferlaino, R. Grimm, P. S. Julienne, and J. M. Hutson, 2011, *Physical Review Letters* **107**(12), 120401, URL <http://link.aps.org/doi/10.1103/PhysRevLett.107.120401>.
- Bethe, H., and R. Peierls, 1935a, *Proceedings of the Royal Society of London. Series A - Mathematical and Physical Sciences* **148**(863), 146, URL <http://rspa.royalsocietypublishing.org/content/148/863/146>.
- Bethe, H. A., and R. Peierls, 1935b, *Proceedings of the Royal Society of London. Series A - Mathematical and Physical Sciences* **149**(866), 176, URL <http://rspa.royalsocietypublishing.org/content/149/866/176>.
- Binder, K., 1987, *Reports on Progress in Physics* **50**(7), 783, URL <http://iopscience.iop.org/0034-4885/50/7/001>.
- Bose, 1924, *Zeitschrift für Physik* **26**(1), 178, URL <http://link.springer.com/article/10.1007/BF01327326>.
- Braaten, E., and H.-W. Hammer, 2006, *Physics Reports* **428**(5–6), 259, URL <http://www.sciencedirect.com/science/article/pii/S0370157306000822>.

- Braaten, E., H.-W. Hammer, and T. Mehen, 2002, *Physical Review Letters* **88**(4), 040401, URL <http://link.aps.org/doi/10.1103/PhysRevLett.88.040401>.
- Castin, Y., and F. Werner, 2013, *Canadian Journal of Physics* **91**(5), 382, English version: arXiv:1212.5512., URL <http://www.nrcresearchpress.com/doi/abs/10.1139/cjp-2012-0569>.
- Ceperley, D. M., 1995, *Reviews of Modern Physics* **67**(2), 279, URL <http://link.aps.org/doi/10.1103/RevModPhys.67.279>.
- Chin, C., R. Grimm, P. Julienne, and E. Tiesinga, 2010, *Reviews of Modern Physics* **82**(2), 1225, URL <http://link.aps.org/doi/10.1103/RevModPhys.82.1225>.
- Cohen-Tannoudji, C., 1973, *Mécanique quantique*, volume 2 (Hermann, Paris), 3rd edition.
- Dalfovo, F., S. Giorgini, L. P. Pitaevskii, and S. Stringari, 1999, *Reviews of Modern Physics* **71**(3), 463, URL <http://link.aps.org/doi/10.1103/RevModPhys.71.463>.
- D’Incao, J. P., H. Suno, and B. D. Esry, 2004, *Physical Review Letters* **93**(12), 123201, URL <http://link.aps.org/doi/10.1103/PhysRevLett.93.123201>.
- Efimov, V., 1970, *Physics Letters B* **33**(8), 563, URL <http://www.sciencedirect.com/science/article/pii/0370269370903497>.
- Efimov, V., 1979, *Yadernaya Fizika* **29**, 1058, English version: 1979, *Soviet Journal of Nuclear Physics* **29**(4), 546.
- Efimov, V. N., 1971, *Yadernaya Fizika* **12**, 1080, English version: 1970, *Soviet Journal of Nuclear Physics* **12**(5), 589.
- Einstein, A., 1924, *Sitzungsberichte der Königlich Preussischen Akademie der Wissenschaften* , 261.
- Einstein, A., 1925, *Sitzungsberichte der Königlich Preussischen Akademie der Wissenschaften* , 6.
- Esry, B. D., C. H. Greene, and J. Burke, James P., 1999, *Physical Review Letters* **83**(9), 1751, URL <http://link.aps.org/doi/10.1103/PhysRevLett.83.1751>.
- Faddeev, L., 1960, *Zhurnal Eksperimental’noi i Teoreticheskoi Fiziki* **39**(5), 1459, English version: 1961, *Soviet Physics JETP* **12**(5), 1014.
- Ferlaino, F., S. Knoop, M. Berninger, W. Harm, J. P. D’Incao, H.-C. Nägerl, and R. Grimm, 2009, *Physical Review Letters* **102**(14), 140401, URL <http://link.aps.org/doi/10.1103/PhysRevLett.102.140401>.

- Ferlaino, F., A. Zenesini, M. Berninger, B. Huang, H.-C. Nägerl, and R. Grimm, 2011, *Few-Body Systems* **51**(2-4), 113, URL <http://link.springer.com/article/10.1007/s00601-011-0260-7>.
- Feynman, R. P., 1972, *Statistical mechanics: A set of lectures* (W. A. Benjamin).
- Gaunt, A. L., T. F. Schmidutz, I. Gotlibovych, R. P. Smith, and Z. Hadzibabic, 2013, *Physical Review Letters* **110**(20), 200406, URL <http://link.aps.org/doi/10.1103/PhysRevLett.110.200406>.
- Greene, C. H., B. Esry, and H. Suno, 2004, *Nuclear Physics A* **737**, 119, URL <http://www.sciencedirect.com/science/article/pii/S0375947404003045>.
- Gross, E. P., 1961, *Il Nuovo Cimento* **20**(3), 454, URL <http://link.springer.com/article/10.1007/BF02731494>.
- Gross, E. P., 1963, *Journal of Mathematical Physics* **4**(2), 195, URL [http://jmp.aip.org/resource/1/jmapaq/v4/i2/p195\\_s1](http://jmp.aip.org/resource/1/jmapaq/v4/i2/p195_s1).
- Hastings, W. K., 1970, *Biometrika* **57**(1), 97, URL <http://biomet.oxfordjournals.org/content/57/1/97>.
- Ho, T.-L., and Q. Zhou, 2010, *Nature Physics* **6**(2), 131, URL <http://www.nature.com/nphys/journal/v6/n2/full/nphys1477.html>.
- Holzmann, M., 2000, *La transition de Bose-Einstein dans un gaz dilué*, Ph.D. thesis, Université Pierre et Marie Curie - Paris VI, URL <http://tel.archives-ouvertes.fr/tel-00011774>.
- Holzmann, M., and W. Krauth, 2008, *Physical Review Letters* **100**(19), 190402, URL <http://link.aps.org/doi/10.1103/PhysRevLett.100.190402>.
- Holzmann, M., W. Krauth, and M. Naraschewski, 1999, *Physical Review A* **59**(4), 2956, URL <http://link.aps.org/doi/10.1103/PhysRevA.59.2956>.
- Huang, K., 1987, *Statistical mechanics* (Wiley, New York), 2nd edition.
- Kraemer, T., M. Mark, P. Waldburger, J. G. Danzl, C. Chin, B. Engeser, A. D. Lange, K. Pilch, A. Jaakkola, H.-C. Nägerl, and R. Grimm, 2006, *Nature* **440**(7082), 315, URL <http://www.nature.com/nature/journal/v440/n7082/full/nature04626.html>.
- Krauth, W., 1996, *Physical Review Letters* **77**(18), 3695, URL <http://link.aps.org/doi/10.1103/PhysRevLett.77.3695>.
- Krauth, W., 2006, *Statistical Mechanics: Algorithms and Computations* (Oxford University Press, USA).

- Landau, L. D., and L. M. Lifshitz, 1981, *Quantum Mechanics (Non-Relativistic Theory)*, number 3 in Course of theoretical physics (Butterworth-Heinemann), 3rd edition.
- Landsberg, P. T., 1961, *Thermodynamics, with quantum statistical illustrations* (Interscience).
- Lee, T. D., K. Huang, and C. N. Yang, 1957, Physical Review **106**(6), 1135, URL <http://link.aps.org/doi/10.1103/PhysRev.106.1135>.
- Lévy, P., 1940, Compositio Mathematica **7**, 283, URL [http://www.numdam.org/numdam-bin/item?id=CM\\_1940\\_\\_7\\_\\_283\\_0](http://www.numdam.org/numdam-bin/item?id=CM_1940__7__283_0).
- Maji, J., S. M. Bhattacharjee, F. Seno, and A. Trovato, 2010, New Journal of Physics **12**(8), 083057, URL <http://iopscience.iop.org/1367-2630/12/8/083057>.
- Makotyn, P., C. E. Klauss, D. L. Goldberger, E. A. Cornell, and D. S. Jin, 2014, Nature Physics URL <http://www.nature.com/nphys/journal/vaop/ncurrent/full/nphys2850.html>.
- Metropolis, N., A. W. Rosenbluth, M. N. Rosenbluth, A. H. Teller, and E. Teller, 1953, Journal of Chemical Physics **21**(6), 1087, URL [http://jcp.aip.org/resource/1/jcpsa6/v21/i6/p1087\\_s1](http://jcp.aip.org/resource/1/jcpsa6/v21/i6/p1087_s1).
- Michel, M., S. C. Kapfer, and W. Krauth, 2014, Journal of Chemical Physics **140**(5), 054116, URL <http://scitation.aip.org/content/aip/journal/jcp/140/5/10.1063/1.4863991>.
- Nishida, Y., Y. Kato, and C. D. Batista, 2013, Nature Physics **9**(2), 93, URL <http://www.nature.com/nphys/journal/v9/n2/full/nphys2523.html>.
- Pitaevskii, L., and S. Stringari, 2003, *Bose–Einstein Condensation* (Oxford University Press).
- Pitaevskii, L. P., 1961, Zhurnal Eksperimental'noi i Teoreticheskoi Fiziki **40**, 646, English version: 1961, Soviet Physics JETP **13**, 451.
- Pollack, S. E., D. Dries, and R. G. Hulet, 2009, Science **326**(5960), 1683, URL <http://www.sciencemag.org/content/326/5960/1683>.
- Pollock, E. L., and D. M. Ceperley, 1984, Physical Review B **30**(5), 2555, URL <http://link.aps.org/doi/10.1103/PhysRevB.30.2555>.
- Prokof'ev, N. V., B. V. Svistunov, and I. S. Tupitsyn, 1998, Physics Letters A **238**(4–5), 253, URL <http://www.sciencedirect.com/science/article/pii/S0375960197009572>.

- Prokof'ev, N. V., B. V. Svistunov, and I. S. Tupitsyn, 1996, *Journal of Experimental and Theoretical Physics Letters* **64**(12), 911, URL <http://link.springer.com/article/10.1134/1.567243>.
- Rem, B. S., A. T. Grier, I. Ferrier-Barbut, U. Eismann, T. Langen, N. Navon, L. Khaykovich, F. Werner, D. S. Petrov, F. Chevy, and C. Salomon, 2013, *Physical Review Letters* **110**(16), 163202, URL <http://link.aps.org/doi/10.1103/PhysRevLett.110.163202>.
- Roy, S., M. Landini, A. Trenkwalder, G. Semeghini, G. Spagnolli, A. Simoni, M. Fattori, M. Inguscio, and G. Modugno, 2013, *Physical Review Letters* **111**(5), 053202, URL <http://link.aps.org/doi/10.1103/PhysRevLett.111.053202>.
- Schmidt, R., S. Rath, and W. Zwerger, 2012, *The European Physical Journal B* **85**(11), 386, URL <http://epjb.epj.org/articles/epjb/abs/2012/11/b120841/b120841.html>.
- von Stecher, J., 2010, *Journal of Physics B: Atomic, Molecular and Optical Physics* **43**(10), 101002, URL <http://iopscience.iop.org/0953-4075/43/10/101002>.
- von Stecher, J., J. P. D'Incao, and C. H. Greene, 2009, *Nature Physics* **5**(6), 417, URL <http://www.nature.com/nphys/journal/v5/n6/full/nphys1253.html>.
- Tan, S., 2008, *Annals of Physics* **323**(12), 2971, URL <http://www.sciencedirect.com/science/article/pii/S0003491608000432>.
- Thomas, L. H., 1935, *Physical Review* **47**(12), 903, URL <http://link.aps.org/doi/10.1103/PhysRev.47.903>.
- Thøgersen, M., D. V. Fedorov, and A. S. Jensen, 2008, *EPL* **83**(3), 30012, URL <http://iopscience.iop.org/0295-5075/83/3/30012/>.
- Trotter, H. F., 1959, *Proceedings of the American Mathematical Society* **10**(4), 545, URL <http://www.ams.org/proc/1959-10-04/S0002-9939-1959-0108732-6/>.
- Wang, J., J. P. D'Incao, B. D. Esry, and C. H. Greene, 2012, *Physical Review Letters* **108**(26), 263001, URL <http://link.aps.org/doi/10.1103/PhysRevLett.108.263001>.
- Wild, R. J., P. Makotyn, J. M. Pino, E. A. Cornell, and D. S. Jin, 2012, *Physical Review Letters* **108**(14), 145305, URL <http://link.aps.org/doi/10.1103/PhysRevLett.108.145305>.
- Zaccanti, M., B. Deissler, C. D'Errico, M. Fattori, M. Jona-Lasinio, S. Müller, G. Roati, M. Inguscio, and G. Modugno, 2009, *Nature Physics* **5**(8), 586, URL <http://www.nature.com/nphys/journal/v5/n8/full/nphys1334.html>.



## Publication 1: Dynamics and thermodynamics of the low-temperature strongly interacting Bose gas

Nir Navon, Swann Piatecki, Kenneth Günter, Benno Rem, Trong Canh Nguyen, Frédéric Chevy, Werner Krauth, and Christophe Salomon, *Physical Review Letters* **107**, 135301 (2011).

This article presents a check of the Lee–Huang–Yang equation of state of the weakly-interacting Bose gas, both using experimental and numerical measures. In the second part, that deals with results obtained by my collaborators from the Lithium group of Laboratoire Kastler Brossel, the dynamic response to varying interaction sweeps is studied experimentally.



## Dynamics and Thermodynamics of the Low-Temperature Strongly Interacting Bose Gas

Nir Navon,<sup>1,\*</sup> Swann Piatecki,<sup>2,†</sup> Kenneth Günter,<sup>1</sup> Benno Rem,<sup>1</sup> Trong Canh Nguyen,<sup>1</sup>  
Frédéric Chevy,<sup>1</sup> Werner Krauth,<sup>2</sup> and Christophe Salomon<sup>1</sup>

<sup>1</sup>Laboratoire Kastler Brossel, CNRS, UPMC, École Normale Supérieure, 24 rue Lhomond, 75005 Paris, France

<sup>2</sup>Laboratoire de Physique Statistique, École Normale Supérieure, UPMC, Université Paris Diderot,  
CNRS, 24 rue Lhomond, 75005 Paris, France

(Received 15 March 2011; revised manuscript received 21 June 2011; published 19 September 2011)

We measure the zero-temperature equation of state of a homogeneous Bose gas of <sup>7</sup>Li atoms by analyzing the *in situ* density distributions of trapped samples. For increasing repulsive interactions our data show a clear departure from mean-field theory and provide a quantitative test of the many-body corrections first predicted in 1957 by Lee, Huang, and Yang [Phys. Rev. **106**, 1135 (1957)]. We further probe the dynamic response of the Bose gas to a varying interaction strength and compare it to simple theoretical models. We deduce a lower bound for the value of the universal constant  $\xi > 0.44(8)$  that would characterize the universal Bose gas at the unitary limit.

DOI: 10.1103/PhysRevLett.107.135301

PACS numbers: 67.85.-d, 05.30.Jp, 32.30.Bv, 67.60.Fp

From sandpiles to neuronal networks, electrons in metals, and quantum liquids, one of the greatest challenges in modern physics is to understand the behavior of strongly interacting systems. A paradigmatic example is superfluid <sup>4</sup>He, the understanding of which has resisted theoretical analysis for decades. Early attempts to address the problem of the strongly interacting Bose liquid focused on the dilute limit. A seminal result for the thermodynamics of the dilute Bose gas was the expansion of the ground state energy (per volume  $V$ ), first obtained in the late 1950s [1]:

$$\frac{E}{V} = \frac{gn^2}{2} \left( 1 + \frac{128}{15\sqrt{\pi}} \sqrt{na^3} + \dots \right), \quad (1)$$

where  $n$  is the density of the gas,  $g = 4\pi\hbar^2 a/m$  is the coupling constant for particles with mass  $m$ , and  $a$  is the  $s$ -wave scattering length, which characterizes the low-energy interactions. The first term in Eq. (1) is the mean-field energy, while the Lee-Huang-Yang (LHY) correction, proportional to  $\sqrt{na^3}$ , is due to quantum fluctuations [1]. Up to this order, the expansion is *universal*, in the sense that it depends solely on the gas parameter  $na^3$  and not on microscopic details of the interaction potential [2–4].

Despite its fundamental importance, this expansion was never checked experimentally before the advent of ultracold quantum gases, where it became possible to tune the value of the scattering length using magnetic Feshbach resonances [5,6]. A first check of the LHY prediction was provided by recent experiments on strongly correlated Fermi gases [7–9] that behave as a gas of tightly bound dimers in the limit of small and positive values of  $a$  [10–12]. By contrast, early studies of Bose gases in the strongly interacting regime were plagued by severe inelastic atom loss [13], but recent experiments at JILA and Rice have revived interest in these systems and showed the onset of beyond mean-field effects [14,15]. Here we report on a quantitative measurement of the thermodynamic equation

of state (EOS) of a strongly interacting atomic Bose gas in the low-temperature limit. We show that the EOS follows the expansion (1), and the comparison with fermionic systems illustrates the universality of the LHY correction.

In the first part, we restrict ourselves to a moderately interacting gas with negligible 3-body atom loss:  $a/a_0 \sim 2000$ ,  $a_0$  being the Bohr radius. In this regime our EOS reveals the Lee-Huang-Yang correction due to quantum fluctuations. We perform quantum Monte Carlo (QMC) simulations to support our zero-temperature approximation. We then test our assumption of thermal equilibrium by dynamically bringing the gas into a more strongly interacting regime where atom loss is no longer negligible. Finally, we explore the unitary regime where the scattering length is infinite.

Our experimental setup was described in [16]. Starting from a <sup>7</sup>Li cloud in a magneto-optical trap, we optically pump the atoms into the  $|F = 2, m_F = 2\rangle$  hyperfine state and transfer them into a magnetic Ioffe trap. After evaporative cooling to a temperature of  $\sim 4 \mu\text{K}$ , the atoms are loaded into a hybrid magnetic/optical trap and then transferred to the  $|F = 1, m_F = 1\rangle$  state. The radial optical confinement of the trap is provided by a single laser beam of  $35 \mu\text{m}$  waist operating at a wavelength of 1073 nm, while the weak axial confinement is enhanced by an additional magnetic-field curvature. We apply a homogeneous magnetic field to tune the interaction strength by means of a wide Feshbach resonance that we locate at 737.8(2) G. The final stage of evaporation in the optical trap is carried out at a bias field of 717 G, where the scattering length has a value of about  $200a_0$ , and results in a Bose-Einstein condensate of  $\sim 6 \times 10^4$  atoms with no discernible thermal part. In the final configuration the trapping frequencies are given by  $\omega_r = 2\pi \times 345(20)$  Hz in the radial and  $\omega_z = 2\pi \times 18.5(1)$  Hz in the axial direction. The magnetic bias field is then adiabatically ramped

to the vicinity of the Feshbach resonance in 150 ms and the density distribution is recorded using *in situ* absorption imaging (Fig. 1). As the EOS critically depends on the scattering length, a precise knowledge of the latter close to the Feshbach resonance is essential. In view of the discrepancy between two recent works [15,17], we have independently calibrated the scattering length  $a(B)$  as a function of magnetic field  $B$  by radio-frequency molecule association spectroscopy [18], as described in the Supplemental Material [19].

For the measurement of the EOS, we follow the method of [9,20–23]. Accordingly, the local pressure  $P(z)$  along the symmetry axis of a harmonically trapped gas is related to the doubly integrated *in situ* density profile  $\bar{n}(z) = \int dx dy n(x, y, z)$ :

$$P(\mu_z) = \frac{m\omega_z^2}{2\pi} \bar{n}(z). \quad (2)$$

This formula relies on the local-density approximation in which the local chemical potential is defined as  $\mu_z = \mu_0 - \frac{1}{2}m\omega_z^2 z^2$ , where  $\mu_0$  is the global chemical potential of the gas.

To measure the pressure at different interaction strengths we have selected images with atom numbers in the range of  $3\text{--}4 \times 10^4$  in order to avoid high optical densities during absorption imaging while keeping a good signal-to-noise ratio. A total of 50 images are used, spanning values of  $a/a_0$  from 700 to 2150. We calibrate the relation between the integrated optical density and the pressure of the gas at weak interaction, well described by mean-field theory (inset of Fig. 2). The density profiles then generate the

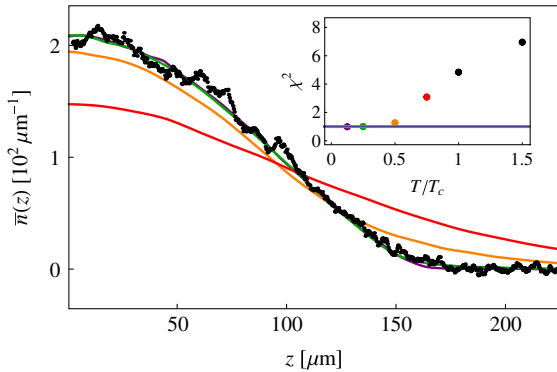


FIG. 1 (color online). Doubly integrated density profile of a trapped Bose gas at a scattering length  $a/a_0 = 2150$ , used to measure the LHY expansion (1). The average over 5 experimental images is shown in black points. The QMC predictions for  $3.9 \times 10^4$  atoms are plotted in a solid line for  $T/T_c = 0.75$  in red, 0.5 in orange, 0.25 in green, and 0.125 in purple (solid lines from bottom to top). Inset:  $\chi^2$  deviation per degree of freedom of a single experimental density profile with QMC results at different temperatures. The excellent agreement between experimental profiles and QMC validates the zero-temperature assumption for the EOS measurement.

EOS (2). The global chemical potential  $\mu_0$  remains to be determined. For this work, we infer  $\mu_0$  self-consistently in a model-independent way from the density profiles (see the Supplemental Material [19]).

In the dilute limit  $na^3 \ll 1$ , where the EOS is universal, dimensional analysis can be used to write the grand canonical EOS of the homogeneous Bose gas at zero temperature in the form

$$P(\mu, a) = \frac{\hbar^2}{ma^5} h(\nu), \quad (3)$$

where  $\nu \equiv \mu a^3/g$  is the (grand canonical) gas parameter and  $h(\nu)$  is the normalized pressure. This EOS contains all thermodynamic macroscopic properties of the system. For example, the energy can be deduced from the pressure using a Legendre transform detailed in the Supplemental Material [19], and in particular, its LHY asymptotic expansion (1). According to the above definition of  $h$ , the mean-field EOS simply reads  $h(\nu) = 2\pi\nu^2$ . These predictions for  $h(\nu)$  are compared to the experimental data points in Fig. 2, and to our QMC calculation. We observe a clear departure of the EOS from the mean-field prediction [dashed gray line (dashed red online)]. At the largest measured value of  $\nu = 2.8 \times 10^{-3}$  our data show a reduction of 20% of the pressure with respect to the mean-field result.

We observe that LHY theory accurately describes our experimental data and is hardly distinguishable from the

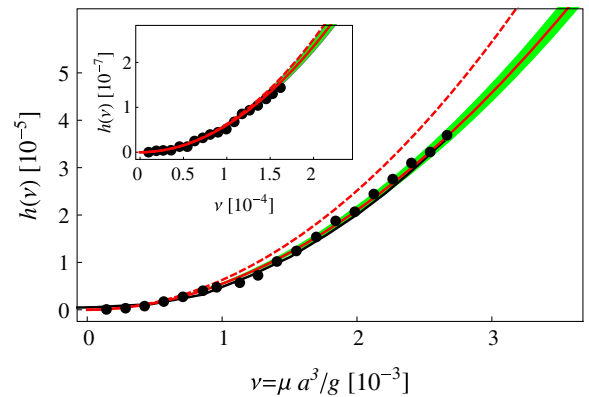


FIG. 2 (color online). Equation of state of the homogeneous Bose gas expressed as the normalized pressure  $h$  as a function of the gas parameter  $\nu$ . The gas samples for the data shown in the main panel (inset) have been prepared at scattering lengths of  $a/a_0 = 1450$  and  $2150$  ( $a/a_0 = 700$ ). The gray (red online) solid line corresponds to the LHY prediction, and the gray (red online) dashed line to the mean-field EOS  $h(\nu) = 2\pi\nu^2$ . In the weakly interacting regime the data are well described by mean-field theory (inset), in opposition to stronger interactions where beyond-mean-field effects are important (main panel). The QMC EOS at  $T/T_c = 0.25$  (solid black line) is nearly indistinguishable from the LHY EOS. The shaded (green online) area delimits the uncertainty of 5% on the value of  $a$ .

QMC in the studied range of interaction strength, a point already put forward in a diffusion Monte Carlo simulation at even higher values of the gas parameter [24]. We can quantify the deviation of our data from mean-field theory by fitting the measured EOS with a function that includes a correction of order  $\sqrt{na^3}$ . For this purpose we convert the energy  $E/N = [2\pi\hbar^2/(ma^2)]na^3[1 + \alpha(na^3)^{1/2}]$  to the grand canonical EOS (see the Supplemental Material [19]) and use  $\alpha$  as a fit parameter in the resulting pressure  $P(\mu)$ . The fit yields the value  $\alpha = 4.5(7)$ , which is in excellent agreement with the theoretical result  $128/(15\sqrt{\pi}) \approx 4.81$  in Eq. (1). Together with the measurement with composite bosons of [9], this provides a striking check of the universality predicted by the expansion (1) up to order  $\sqrt{na^3}$  [11].

In the above interpretation we assumed that the zero-temperature regime has effectively been reached. To check this crucial assumption, we have performed finite-temperature path-integral quantum Monte Carlo simulations [25] in the anisotropic harmonic trap geometry of the experiment with continuous space variables. The experimental atom number can be reached without difficulty and pair interactions are described by a pseudopotential. All thermodynamic properties of the gas at finite temperature are obtained to high precision and without systematic errors. As seen in Fig. 1, we find good agreement between the experimental density distributions and the QMC profiles at temperatures up to  $0.25T_c$ , where  $T_c$  is the condensation temperature of the ideal Bose gas. This shows that thermal effects are negligible and lead to an error in the EOS much smaller than the statistical error bars in Fig. 2.

We now assess the adiabaticity of the interaction sweep in the measurements described above. A violation of adiabaticity could lead to nonequilibrium density profiles that distort the measured EOS. We study the dynamics of the Bose gas subjected to time-dependent interaction sweeps into increasingly strongly interacting regimes, where the enhanced three-body loss rate limits the practical duration of the sweep. In Fig. 3 we plot the axial cloud size determined by a Thomas-Fermi fit as a function of the sweep duration. The magnetic field is ramped approximately linearly in time, sweeping  $a/a_0$  from an initial value of 200 to different final values. Besides the experimental data we present theoretical results from a mean-field scaling solution [26,27] and from a solution of the hydrodynamic equations incorporating the LHY EOS based on a variational scaling ansatz [28]. The latter shows a remarkable agreement with our experimental data for  $a \leq 3000a_0$ . For scattering lengths  $a/a_0 \leq 840$  the radius is nearly constant for sweep durations  $\tau\omega_z/(2\pi) > 1.5$  ( $\tau > 80$  ms), indicating that the cloud follows the interaction strength adiabatically. For the largest value used in the EOS study ( $a/a_0 = 2150$ ), the atom loss is less than 4% and the cloud size after the  $\tau = 150$  ms sweep [ $\tau\omega_z/(2\pi) \approx 2.8$ ] is 2.5%

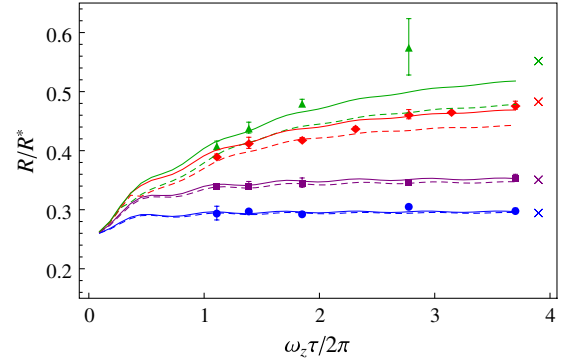


FIG. 3 (color online). Radius  $R$  of the Bose gas as a function of the duration  $\tau$  of the interaction sweep. The radius  $R$  is normalized to the radius  $R^* = a_{\text{ho}}(15\lambda^2 N)^{1/5}$  [where  $a_{\text{ho}} = (\hbar/m\omega_z)^{1/2}$  and  $\lambda = \omega_r/\omega_z$ ].  $N$  is the measured atom number at the end of each sweep. The final values of  $a/a_0$  are 380 (blue dots), 840 (purple squares), 2940 (red diamonds), and 4580 (green triangles). The solid (dashed) lines show the solution of a variational hydrodynamic approach (mean-field scaling solutions). The crosses show the predicted equilibrium beyond-mean-field radii.

smaller than the equilibrium value. We have corrected for this systematic effect by rescaling the measured density  $n_0$  for the determination of the EOS,  $\bar{n} = \eta^{-1}\bar{n}_0(\eta z)$  (with  $\eta = 0.975$  for  $a/a_0 = 2150$ ).

The properties of the Bose gas for very large values of  $na^3$  constitute a challenging open problem. Because of the

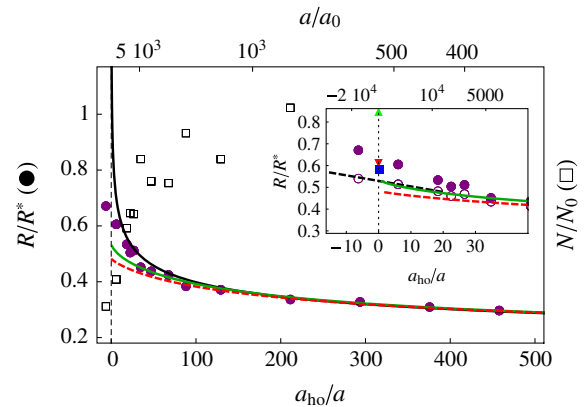


FIG. 4 (color online). Normalized cloud radius  $R_{\text{TF}}/R^*$  (filled purple circles) and normalized atom number (open black squares) as a function of the inverse scattering length  $a_{\text{ho}}/a$  at the end of a 75-ms magnetic-field sweep. The static mean-field prediction is plotted in a solid black line, the mean-field scaling solution in a dashed red line, and the beyond mean-field scaling ansatz in a solid gray line (green online). Inset: Zoom around the unitary limit. Predictions for the universal constant  $\xi$  are shown in an up triangle [34], down triangle [33], and square [32]. The filled (empty) circles correspond to the radii normalized to the final (initial) atom number (see [31]). The dashed black line is the linear interpolation at unitarity.

experimental limitation imposed by three-body recombination, we access this region with a shorter sweep of duration  $\tau\omega_z/(2\pi) = 1.35$  ( $\tau \approx 75$  ms). In Fig. 4 we plot the normalized radius of the Bose gas as a function of the inverse scattering length  $a_{\text{ho}}/a$ . Deep in the mean-field regime ( $a \lesssim 800a_0$ ) the ramp is adiabatic as the data match the equilibrium Thomas-Fermi prediction. As the scattering length is increased, both nonadiabaticity and beyond mean-field effects become important. A departure from the equilibrium result becomes evident above a scattering length of  $\approx 2000a_0$ . Taking into account the mean-field dynamics gives an improved description of our data (red dashed line). Even better agreement (up to values of  $a/a_0 \approx 5000$ ) is obtained with the variational approach incorporating the LHY correction as presented above [gray solid line (green online)] [28]. Probing larger values of the scattering length enables us to gain further insight into the unitary Bose gas,  $a = \infty$ . Because of the low densities of our samples, only half of the atoms are lost at the end of the sweep to the resonance (see squares in Fig. 4). Universal thermodynamics at unitarity have been conjectured for quantum gases [29] and successfully checked experimentally for Fermi gases [30]. In the case of bosonic atoms the existence of a many-body universal state at unitarity is still unknown. Under the assumption of universality, the only relevant length scale should be the interparticle spacing  $n^{-1/3}$  and the EOS would take the form  $\mu \propto \frac{\hbar^2}{m} n^{2/3}$ . Up to a numerical factor, this EOS is identical to that of an ideal Fermi gas and we can write  $\mu = \xi E_F$  [where  $E_F = \hbar^2/2m(6\pi^2 n)^{2/3}$ ]. As we increase the scattering length towards the unitarity regime, the cloud is expected to grow in size. Because of the finite response time of the gas, it is reasonable to assume that the measured radius  $R$  is smaller than the equilibrium radius. From this inequality, in the spirit of variational methods, we deduce a lower bound for the value of  $\xi$  by interpolating our data at unitarity [black dashed line in the inset of Fig. 4]:  $\xi > 0.44(8)$  [31]. This bound is satisfied for the predictions  $\xi = 0.66$  [32] and for the upper bounds from variational calculations, 0.80 [33] and 2.93 [34].

Future work could focus on the measurement of the condensate fraction since the quantum depletion is expected to be as large as  $\sim 8\%$  for our most strongly interacting samples in equilibrium, and on finite-temperature thermodynamic properties [35]. Our measurements on resonance as well as future theoretical studies should give crucial insights on the unitary Bose gas.

We are grateful to Y. Castin, F. Werner, X. Leyronas, S. Stringari, S. Giorgini, S. Pilati, and A. Grier for discussions and to C. Lancien, I. Lahlou, S. El-Ghazzal, T. Vu, and L. Bernard for experimental assistance. We thank J. Dalibard and S. Nascimbène for useful comments on the manuscript. We acknowledge support from ESF Euroquam (FerMix), ANR FABIOLA, Région Ile de France (IFRAF), ERC, and Institut Universitaire de France.

\*navon@ens.fr

†swann.piatecki@ens.fr

- [1] T. D. Lee, Kerson Huang, and C. N. Yang, *Phys. Rev.* **106**, 1135 (1957).
- [2] K. Brueckner and K. Sawada, *Phys. Rev.* **106**, 1117 (1957).
- [3] S. Beliaev, *JETP* **7**, 289 (1958).
- [4] E. Lieb, *Phys. Rev.* **130**, 2518 (1963).
- [5] S. Inouye *et al.*, *Nature (London)* **392**, 151 (1998).
- [6] J. Roberts *et al.*, *Phys. Rev. Lett.* **85**, 728 (2000).
- [7] A. Altmeyer *et al.*, *Phys. Rev. Lett.* **98**, 40401 (2007).
- [8] Y. Shin *et al.*, *Phys. Rev. Lett.* **101**, 070404 (2008).
- [9] N. Navon *et al.*, *Science* **328**, 729 (2010).
- [10] G. Astrakharchik *et al.*, *Phys. Rev. Lett.* **93**, 200404 (2004).
- [11] X. Leyronas and R. Combescot, *Phys. Rev. Lett.* **99**, 170402 (2007).
- [12] H. Hu *et al.*, *Europhys. Lett.* **74**, 574 (2006).
- [13] P. Fedichev *et al.*, *Phys. Rev. Lett.* **77**, 2921 (1996).
- [14] S. Papp *et al.*, *Phys. Rev. Lett.* **101**, 135301 (2008).
- [15] S. Pollack *et al.*, *Phys. Rev. Lett.* **102**, 90402 (2009).
- [16] S. Nascimbene *et al.*, *Phys. Rev. Lett.* **103**, 170402 (2009).
- [17] N. Gross *et al.*, *Phys. Rev. Lett.* **105**, 103203 (2010).
- [18] J. Zirbel *et al.*, *Phys. Rev. A* **78**, 13416 (2008).
- [19] See Supplemental Material at <http://link.aps.org/supplemental/10.1103/PhysRevLett.107.135301> for technical details about the density profiles analysis and Feshbach resonance calibration.
- [20] C. H. Cheng and S. K. Yip, *Phys. Rev. B* **75**, 14526 (2007).
- [21] Y. I. Shin, *Phys. Rev. A* **77**, 41603 (2008).
- [22] T. Ho and Q. Zhou, *Nature Phys.* **6**, 131 (2009).
- [23] S. Nascimbene *et al.*, *Nature (London)* **463**, 1057 (2010).
- [24] S. Giorgini, J. Boronat, and J. Casulleras, *Phys. Rev. A* **60**, 5129 (1999).
- [25] W. Krauth, *Phys. Rev. Lett.* **77**, 3695 (1996).
- [26] Y. Castin and R. Dum, *Phys. Rev. Lett.* **77**, 5315 (1996).
- [27] Y. Kagan, E. L. Surkov, and G. V. Shlyapnikov, *Phys. Rev. Lett.* **79**, 2604 (1997).
- [28] The details of the time-dependent analysis will be published elsewhere.
- [29] T. L. Ho, *Phys. Rev. Lett.* **92**, 90402 (2004).
- [30] M. Inguscio, W. Ketterle, and C. Salomon, *Proceedings of the International School of Physics Enrico Fermi, Course CLXIV* (IOS Press, Amsterdam, 2006).
- [31] At unitarity, the cloud radius  $R$  would scale as  $N^{1/6}\xi^{1/4}$ . The normalization  $R^*$  used in Fig. 4 scales as  $N^{1/5}$  so that  $R/R^* \propto \xi^{1/4}N^{-1/30}$  very slowly depends on the atom number. In order to take into account the changing atom number near unitarity and obtain a safe experimental lower bound on  $\xi \propto (R/R^*)^4 N^{2/15}$ , we minimize both  $R/R^*$  and  $N^{2/15}$ . This is done by taking for  $R/R^*$  the initial atom number (empty circles in the inset of Fig. 4), and the final, for  $N^{2/15}$ .
- [32] Y.-L. Lee and Y.-W. Lee, *Phys. Rev. A* **81**, 063613 (2010).
- [33] J. L. Song and F. Zhou, *Phys. Rev. Lett.* **103**, 25302 (2009).
- [34] S. Cowell *et al.*, *Phys. Rev. Lett.* **88**, 210403 (2002).
- [35] R. Smith, R. Campbell, N. Tammuz, and Z. Hadzibabic, *Phys. Rev. Lett.* **106**, 250403 (2011).

## Publication 2: Efimov-driven phase transitions of the unitary Bose gas

Swann Piatecki and Werner Krauth, *Nature Communications* **5**, 3503 (2014).

This article presents path-integral Monte Carlo computations for unitary bosons. Efimov trimers are discussed in terms of path integrals. Simulations of the unitary Bose gas provide a check of the third virial coefficient, and show that unitary bosons may undergo a first-order phase transition to a new quantum phase, the Efimov liquid.



# Efimov-driven phase transitions of the unitary Bose gas

Swann Piatecki and Werner Krauth\*

*Laboratoire de Physique Statistique, École Normale Supérieure,  
UPMC, Université Paris Diderot, CNRS,  
24 rue Lhomond, 75005 Paris, France*

## Abstract

Initially predicted in nuclear physics, Efimov trimers are bound configurations of three quantum particles that fall apart when any one of them is removed. They open a window into a rich quantum world that has become the focus of intense experimental and theoretical research, as the region of “unitary” interactions, where Efimov trimers form, is now accessible in cold-atom experiments. Here, we use a path-integral Monte Carlo algorithm backed up by theoretical arguments to show that unitary bosons undergo a first-order phase transition from a normal gas to a superfluid Efimov liquid, bound by the same effects as Efimov trimers. A triple point separates these two phases and another superfluid phase, the conventional Bose–Einstein condensate, whose coexistence line with the Efimov liquid ends in a critical point. We discuss the prospects of observing the proposed phase transitions in cold-atom systems.

(Article in the version accepted after peer review. Full article available at <http://www.nature.com/ncomms/2014/140320/ncomms4503/full/ncomms4503.html>.)

©2014 Macmillan Publishers Limited. All rights reserved.

---

\* [werner.krauth@ens.fr](mailto:werner.krauth@ens.fr)

## INTRODUCTION

A striking analogue to Borromean rings, Efimov trimers are bound configurations of three quantum particles that form near the point of “unitary” interactions [1], where the pair potential becomes too weak to bind any two of them. Efimov trimers open a window into a largely uncharted world of quantum physics based on many-particle bound states. They were discovered in nuclear physics[2–4], but have also been discussed in quantum magnets[5], biophysics of DNA[6] and, most importantly, in ultra-cold atomic gases. In these systems, it has become possible to fine-tune both the sign and the value of the pair interactions through the Feshbach mechanism [7], from a scattering length  $a$  close to zero up to the unitary point  $|a| = \infty$ . In current experiments, Efimov trimers have not been seen directly, but their presence has been traced through the variations of the rate at which the gas loses particles as the interactions are scanned through the unitary region[8–11].

Theoretical research on Efimov physics has unveiled its universal nature, with the three-particle bound states that form an infinite sequence at unitarity, and that disappear with zero energy at large negative scattering lengths. Beyond the physics of three bound particles, the ground-state properties of small unitary clusters were studied numerically [12], and their spectrum computed with a variational ansatz [13] in a trap. However, the macroscopic many-body properties of the unitary Bose gas have remained unknown. The understanding of its thermodynamic behaviour is of great importance, especially as the experimental stability of the unitary Bose gas of cold atoms has been reported for appreciable time scales[11, 14, 15].

In this work, we apply a dedicated Path-Integral Monte Carlo algorithm to the unitary Bose gas. This allows us to address the thermodynamics of unitary bosons at finite temperature, both above and below Bose-Einstein condensation. We obtain the phase diagram of a finite number of trapped bosons, and back up our numerical calculations by a general theoretical model, that yields a homogeneous phase diagram. At high temperature, we find that the unitary Bose gas is very well described by the available virial coefficients[16]. At lower temperature, the unitary Bose gas undergoes a first-order phase transition to a new superfluid phase, the Efimov liquid, held together by the same effects as Efimov trimers, and whose physical quantities are given by three-body observables. From these two phases, transition lines to a third phase, the conventional Bose-Einstein condensate (BEC), start at a triple point. The coexistence line between the Efimov liquid and the conventional Bose-

Einstein condensate ends in a critical point at high temperature. At a difference with the experimental systems, our model is thermodynamically stable. This is assured through a parameter, the three-body hard core  $R_0$ , that bounds from below the energies of the Efimov states. In cold-atom systems, this parameter is on the order of the van der Waals length  $l_{\text{vdW}}$  [17–19]. Experimental cold-atom systems are metastable, and particles disappear from the trap into deeply bound states, via the notorious three-body losses. This intricate quantum dynamics, and the description of the losses, are naturally beyond our exact Quantum Monte Carlo approach, and we discuss them on a phenomenological level, in order to assess the prospects for experimental tests of our predictions.

## RESULTS

### Model Hamiltonian

We describe the system of  $N$  interacting bosons by a Hamiltonian

$$H = \sum_i \frac{\mathbf{p}_i^2}{2m} + \sum_{i<j} V_2^a(r_{ij}) + \sum_{i<j<k} V_3(R_{ijk}) + \frac{m\omega^2}{2} \sum_i \mathbf{x}_i^2, \quad (1)$$

where  $\mathbf{p}_i$ ,  $\mathbf{x}_i$  and  $m$  are the momentum, the position and the mass of particle  $i$ . The pair interaction  $V_2^a$  has zero range, and may be viewed, as illustrated in Fig. 1a-c, as a square-well interaction potential whose range  $r_0$  and depth  $V_0$  are simultaneously taken to 0 and  $\infty$  while keeping the scattering length  $a$  constant. The unitary point, where the only bound state disappears with zero energy and infinite extension, corresponds to an infinite scattering length  $a$ . The three-body interaction  $V_3$  implements a hard-core hyperradial cutoff condition,  $R_{ijk} > R_0$ , where the hyperradius  $R_{ijk}$  of particles  $i$ ,  $j$ , and  $k$  corresponds to their root-mean-square pair distance ( $3R_{ijk}^2 = r_{ij}^2 + r_{ik}^2 + r_{jk}^2$ ). This three-body hard core prevents the so-called Thomas collapse[20] into a many-body state with vanishing extension and infinite negative energy by setting a fundamental trimer energy  $-E_t \propto R_0^{-2}$ . The final term in Eq. (1) models an isotropic harmonic trapping potential of length  $a_\omega = \sqrt{\hbar/(m\omega)}$  as it is realized in ultracold bosons experiments. The properties of the system described by Eq. (1) are universal when  $R_0$  is much smaller than all other length scales.

## Path-integral representation and Efimov trimers

In thermal equilibrium, within the path-integral representation of quantum systems that we use for our computations, position variables  $\mathbf{x}_i(\tau)$  carry an imaginary-time index  $\tau \in [0, \beta = 1/k_B T]$ , where  $k_B$  is the Boltzmann constant and  $T$  is the temperature. The fluctuations of  $\mathbf{x}_i(\tau)$  along  $\tau$  account for the quantum uncertainty. The bosonic nature of many-particle systems manifests itself through the periodic boundary conditions in  $\tau$  and, in particular, through the permutation structure of particles. The length of permutation cycles correlates with the degree of quantum coherence[21–23]. Interactions set the statistical weights of configurations[24, 25]. Ensemble averaging, performed by a dedicated Quantum Monte Carlo algorithm, yields the complete thermodynamics of the system (see the Methods section for computational details). The  $N$ -body simulation code is massively run on a cluster of independent processors. It succeeds in equilibrating samples with up to a few hundred bosons.

Fig. 1 presents snapshots of three bosons in a shallow trap at  $\omega \sim 0$  that illustrate the quantum fluctuations in  $\mathbf{x}_i(\tau)$ , and characterize the Efimov trimer (see the Methods section for a full description of the three bosons simulation). Indeed, for two-body interactions without a bound state, virtually free particles fluctuate on the scale of the de Broglie thermal wavelength  $\lambda_{\text{th}} = \sqrt{2\pi\hbar^2\beta/m}$  that diverges at low temperature (see Fig. 1a). In contrast, for positive  $a$ , a bound state with energy  $-E_{\text{dimer}} = -\hbar^2/(ma^2)$  forms in the two-body interaction potential. Two particles bind into a dimer, and the third particle is free (see Fig. 1c). At unitarity, the bound state of the pair potential is at resonance  $E_{\text{dimer}} = 0$ , and the scattering length  $a$  is infinite (see Fig. 1b). At this point, the two-body interaction is scale-free. While two isolated particles do not bind, in the three-particle system, pairs of particles approach each other, and then dissociate, so that, between  $\tau = 0$  and  $\tau = \beta$ , the identity of close-by partners changes several times. This coherent particle-pair scattering process, the hallmark of the Efimov effect[4], is highlighted in Fig. 1b. At small temperatures, the fluctuations of this bound state remain on a scale proportional to  $R_0$  and do not diverge as  $\lambda_{\text{th}}$ .

While the two-particle properties are universal at unitarity, the three-boson fundamental trimer state generally depends on the details of the pair interaction. Excited trimers form a geometric sequence of asymptotically universal Efimov trimers with an asymptotic ratio

of energies  $E_n/E_{n+1} \approx 515.0$  when  $n \rightarrow \infty$ , where  $E_n$  is the energy of the  $n$ -th excited trimer[1]. Due to this large ratio, thermal averages cannot identify individual trimer states other than the fundamental trimer at low temperature. For the model Hamiltonian of Eq. (1), the ground-state trimer is virtually identical to a universal Efimov trimer[12], and we obtain excellent agreement of the probability distribution of the hyperradius  $R$  with its analytically known distribution  $p_R(R)$  (see Fig. 1d)[1]. This effectively validates our algorithm. Furthermore, the observed quadratic divergence of the pair distance distribution  $\rho_r(r)$ , leading to an asymptotically constant  $r^2\rho_r(r)$  for  $r \rightarrow 0$  (see Fig. 1e), checks with the Bethe–Peierls condition for the zero-range unitary potential[26].

### Equation of state of the unitary Bose gas

In local-density approximation, particles experience an effective chemical potential  $\mu(r) = \mu_0 - m\omega^2 r^2/2$  that depends on the distance  $r$  from the centre of the trap. This allows us to obtain the grand-canonical equation of state (pressure  $P$  as a function of  $\mu$ ) from the doubly-integrated density profile [27] obtained from a single simulation run at temperature  $T$ . We find that the equation of state of the normal gas is described very accurately by the virial expansion up to third order in the fugacity  $e^{\beta\mu}$  (see Fig. 2 and the Methods section)[16]. The third-order term is crucial to the description of Efimov physics as it is the first term at which three-body effects appear[28]. It depends explicitly on  $T$  and  $R_0$ .

### Phase transitions in the trapped unitary Bose gas

In the harmonic trap, particles can be in different thermodynamic phases depending on the distance  $r$  from its centre. We monitor the correlation between the pair distances and the position in the trap, and are able to track the creation of a drop of high-density liquid at  $r \sim 0$  (see Fig. 3a-c). This drop grows as the temperature decreases. The observed behaviour corresponds to a first-order normal-gas-to-superfluid-liquid transition, and is fundamentally different from the second-order free Bose–Einstein condensation (see Supplementary Fig. 1). All particles in the drop are linked through coherent close-by particle switches as in Fig. 1b, showing that the drop is superfluid. Deep inside the liquid phase, the Quantum Monte Carlo simulation drops out of equilibrium on the available simulation times. Nevertheless, at its

onset and for all values of  $R_0$ , the peak of the pair correlation function is located around  $10R_0$ , which indicates that the liquid phase is of constant density  $n_l \propto R_0^{-3}$  (see Fig. 3c). At larger values of  $R_0$ , the density difference between the trap centre and the outside vanishes continuously, and the phase transition is no longer seen (see Fig. 3d-f). Beyond this critical point, the peak of the pair correlation also stabilizes around  $10R_0$ , which indicates a crossover to liquid behaviour (see Fig. 3f and the Methods section for additional details on the characterization of the first-order phase transition).

### Model for the normal-gas-to-Efimov-liquid transition

Our numerical findings suggest a theoretical model for the competition between the unitary gas in third-order virial expansion and an incompressible liquid of density  $n_l \propto R_0^{-3}$  and constant energy per particle  $-\epsilon \propto E_t$ , as suggested by ground-state computations for small clusters[12] (see Supplementary Fig. 2). For simplicity, we neglect the entropic contributions to the liquid-state free energy  $\epsilon \gg TS$ , so that  $F_l \approx -N\epsilon$ . The phase equilibrium is due to the difference in free energy and in specific volume at the saturated vapour pressure (see the Methods section and Supplementary Fig. 3). We extend the third-order virial expansion to describe the gaseous phase in the region where quantum correlations become important. Because the conventional Bose–Einstein condensation is continuous, it still conveys qualitative information about the transition into the superfluid Efimov liquid in that region. At small  $R_0 \rightarrow 0$ , the coexistence line approaches infinite temperatures as the fundamental trimer energy  $E_t \propto R_0^{-2}$  diverges. For larger values of  $R_0$ , the density of the liquid decreases and approaches the one of the gas. The liquid–gas transition line ends in a critical point, where both densities coincide. As the liquid is bound by quantum coherence intrinsic to the Efimov effect, this critical point must always be inside a superfluid, that is, between the Efimov liquid and the Bose–Einstein condensate, which become indistinguishable. The agreement between this approximate theory and numerical calculations for the trap centre phase diagram is remarkable (see Fig. 4a). Beyond the critical point, we no longer observe a steep drop in the density on decreasing the temperature. We also notice that quantum coherence builds up in the gaseous phase, so that only a conventional Bose–Einstein condensation takes place. Our numerical results suggest it occurs at a temperature slightly lower than that for the ideal Bose gas[29],  $k_B T_{\text{BEC}}^0 \approx \hbar\omega(0.94N^{1/3} - 0.69)$ .

## Homogeneous phase diagram of the unitary Bose gas

Our theoretical model also yields a phase diagram for a homogeneous system of unitary bosons (see Fig. 4b) where, in addition, the conventional Bose–Einstein condensation is simply modelled by that of free bosons[30]. In absence of a harmonic trap, only two independent dimensionless numbers may be built,  $k_{\text{B}}T/\epsilon$ , and  $P\hbar^3/\sqrt{m^3\epsilon^5}$ . As a consequence, the phase diagram in these two dimensionless numbers is independent of the choice of  $\epsilon$ , that is, of  $R_0$ . The scaling of the dimensionless pressure with  $R_0^5$  and of the dimensionless temperature with  $R_0^2$  explains that the triple point appears much farther from the critical point in the homogeneous phase diagram than in the trap. We expect model-dependent non-universal effects in two regions. At high temperature  $\lambda_{\text{th}} \ll R_0$ , only a classical gas should exist as the quantum fluctuations are too small to build up quantum coherence and, in particular, permutations between particles. At high pressure  $P \propto T$ , we expect a classical solid phase driven by entropic effects, as for conventional hard-sphere melting.

## DISCUSSION

To situate the theoretical results presented in this work in an experimental context, we present the data of Fig. 4b in terms of  $R_0n^{1/3}$  and  $\lambda_{\text{th}}n^{1/3}$  (see Fig. 5). In this diagram, systems with identical values of  $T$  and  $R_0$  and different densities correspond to straight lines passing through the origin. In the unstable region, we expect a homogeneous system described by the Hamiltonian of Eq. (1) to phase-separate on the same such line into the superfluid Efimov liquid and the normal gas or the Bose–Einstein condensate.

In cold-atom systems, the atomic interactions have deeply-bound states not present in our model, and the strict hyperradial cutoff is absent. Nevertheless, an effective three-body barrier at a universal value  $\sim 2l_{\text{vdW}}$ [18] induces a universal relation between the fundamental trimer energy  $E_t$  and the van der Waals length  $l_{\text{vdW}}$  [17, 19, 31, 32]. In Fig. 5, a vertical line marks the experimentally realistic value  $R_0n^{1/3} \sim 0.023$  obtained for  $^{133}\text{Cs}$  atoms at a density  $n = 10^{13}\text{cm}^{-3}$ , using  $R_0 \sim 2l_{\text{vdW}}$  and  $l_{\text{vdW}} = 101a_0$  [7], where  $a_0$  is the Bohr radius. Other atomic species yield smaller values of  $R_0n^{1/3}$ , for which this discussion is also valid. An experimental system may be quenched along this line into the unstable region by suddenly increasing the scattering length up to unitarity *via* the Feshbach mechanism. If this

quench starts from a weakly-interacting Bose–Einstein condensate at very low temperature, the four-body recombination process (that saturates at a rate  $K_4 \sim \hbar\lambda_{\text{th}}^7/m$ ) will dominate the three-body recombination process (that saturates at a rate  $K_3 \sim \hbar\lambda_{\text{th}}^4/m$ ) [11, 33–35], a condition that may be written as  $nK_4 \gtrsim K_3$  (cf. [36, 37]). Whereas the latter is responsible for the three-body losses into deeply-bound dimer states, the former may represent one possible strategy for creating Efimov trimers.

In the unstable region, the recombination process would create liquid droplets of ever increasing size. Deep inside the unstable region, far away from the coexistence line, we expect this growth to be a fast, barrier-free, runaway process involving spinodal decomposition [38, 39], rather than a slow activation process of nucleation over a free-energy barrier produced by the competition of bulk and surface energies. In a thermodynamically stable system, complete separation on macroscopic length scales proceeds through a coarsening process on length scales that slowly increase with time [38, 40]. At the Bose–Einstein condensation temperature of the non-interacting gas, this would lead to a large liquid fraction  $1 - n_g/n$ , where  $n_g$  is the density of the gas at coexistence, and  $n$  the density of the system before phase separation. However, this will certainly not be observable in current cold-atoms experiments, as sufficiently large droplets of dense liquid are unstable towards decay into deeply-bound atomic states. Nevertheless, the instability of the gas and the creation of microscopic liquid droplets might be quite realistic. These could be observed as they would lead to an important increase of the three-body losses, proportional to  $K_3 n_l^3$  in the liquid phase.

The timescales for the creation of a minority liquid phase after a quench is a classic problem of non-equilibrium statistical mechanics. In the present context, it is rendered even richer by the fact that the initial low-temperature phase is a weakly interacting superfluid, and that even the normal gas phase is thermodynamically unstable. These questions are closely related to the very existence of the unitary Bose gas on time scales larger than its thermalization time. Very recent experimental works indicate that the ultra-cold unitary Bose gas can indeed be stabilized on appreciable time scales [11, 14, 15].

## METHODS

### Path-integral Monte Carlo algorithm

In our path-integral quantum Monte Carlo simulation, the contribution of the three-body hard-core interaction to the statistical weights of discretised path configurations are computed using Trotter's approximation, which consists in simply rejecting configurations with  $R < R_0$ . The contribution of the zero-range unitary interaction is computed using the pair-product approximation, which estimates the weight of two nearby particles without taking other particles into consideration. Both approximations are valid when the discretisation step is small[23].

In the simulation, new configurations are built from existing configurations according to several possible update moves. A new one, the compression-dilation move, was introduced to specifically address the divergence of the pair correlation function at small distances (see Fig. 1e and Supplementary Fig. 4). For each set of parameters, the simulation was run on up to 16 independent processors for up to 10 days to reduce the statistical error.

### Simulation of three bosons

In our simulations of unitary bosons, the system is contained in a harmonic trap. This regulates the available configuration space. For the same purpose, in the three-body calculations at  $\omega \sim 0$  presented in Fig. 1, we impose that the three bosons are on a single permutation cycle: In Fig. 1a-c the blue, red, and green bosons are respectively exchanged with the red, green, and blue bosons at imaginary time  $\beta$ . This condition does not modify the properties of the fundamental trimers at unitarity, as other permutations could be sampled at no cost at points of close encounter such as those highlighted in Fig. 1b.

Fig. 1a-c presents four-dimensional co-cyclic path-integral configurations in three-dimensional plots. In this graphic representation, the centre of mass, whose motion is decoupled from the effect of the interactions, is set to zero at all  $\tau$ . The three spatial dimensions are then reduced to two dimensions by rotating the triangle formed by the three particles at each imaginary time to the same plane in a way that does not favour any of the three spatial dimensions while conserving the permutation cycle structure and the pair distances.

## High temperature equation of state

Within the local density approximation, the grand-canonical equation of state  $P(\mu)$  may be obtained from the numerical doubly-integrated density profile  $\bar{n}(x)$  [27] as

$$P(\mu(x)) = \frac{m\omega^2}{2\pi} \bar{n}(x), \quad (2)$$

where  $\mu(x) = \mu_0 - m\omega^2 x^2/2$  is the local chemical potential along direction  $x$ , and  $\mu_0$  the chemical potential at the centre of the trap, measured from a fit of the equation of state to that of an ideal gas in the outer region of the trap.

We compare this numerical equation of state to the cluster expansion, that expresses the pressure in terms of the fugacity  $e^{\beta\mu}$  (see Fig. 2):

$$P = \frac{k_B T}{\lambda_{\text{th}}^3} \sum_{l \geq 1} b_l e^{l\beta\mu}. \quad (3)$$

The  $l$ -th cluster integral  $b_l$  follows from the virial coefficients of smaller order. It represents  $l$ -body effects that cannot be reduced to smaller non-interacting groups of interacting particles[28]. We use the analytical expressions of  $b_2$  and  $b_3$  at unitarity that have become available [16].

## Monitoring the phase transitions

When the densities of the gas and the superfluid Efimov liquid approach each other, observing directly the two-dimensional histogram of pair distances and centre-of-mass positions does not allow to distinguish between a weakly first-order phase transition and a cross-over (see Supplementary Fig. 5). In this regime, we monitor the normal-gas-to-superfluid-liquid phase transition more accurately by following the evolution of the first peak of the pair correlation function (obtained by ensemble averaging) with temperature (see Supplementary Fig. 6). In Fig. 4, Bose–Einstein condensation is assumed when particles lie on a permutation cycle of length greater than 10 with probability 0.05[22].

## Analytical model for the transition into the Efimov liquid

First-order phase transitions take place when the free energy  $F$  of a homogeneous physical system is not a convex function of its volume  $V$ . Splitting the system into two phases is

then favourable over keeping it homogeneous (see Supplementary Fig. 3). In this situation, at coexistence and in absence of interface energy, the chemical potentials and the pressures of both phases are equal.

The virial expansion is an excellent approximation to describe the normal gas phase of unitary bosons far from the superfluid transition. Although this expansion becomes irrelevant in the superfluid gas, its analytic continuation conveys important qualitative features because of the continuous nature of conventional Bose–Einstein condensation, and is therefore a suitable approximation for the conventional Bose–Einstein condensate.

The theoretical model for the superfluid liquid is that of an incompressible liquid of specific volume  $v_1$  and negligible entropic contribution to the free energy  $F_1 = -N\epsilon$ . Simulations yield  $v_1^{-1/3} \sim 5R_0$ , and the negligible contribution of the entropy to the free energy is ensured for non-pathological systems at low temperature. The results of Ref. 12 may be extrapolated to  $\epsilon = 10.1E_t$  (see Supplementary Fig. 2), a value adjusted to  $\epsilon = 8E_t$  in Fig. 4a to account for finite-size effects.

In practice, we draw the transition line into the superfluid liquid by finding the smallest chemical potential at which the pressures of the incompressible liquid and of the normal gas coincide at a temperature  $T$ :

$$\frac{\mu + \epsilon}{v_1} = \frac{k_B T}{\lambda_{\text{th}}^3} (e^{\beta\mu} + b_2 e^{2\beta\mu} + b_3 e^{3\beta\mu}). \quad (4)$$

As  $n = 1/v = \partial_\mu P$ , the crossing to the regime where this equation has no solution corresponds to the critical point, where both densities are equal.

To draw the coexistence line for the trap centre with  $N = 100$  particles in Fig. 4a, its chemical potential  $\mu_0$  is found from integrating the density throughout the trap:

$$\frac{4\pi}{\lambda_{\text{th}}^3} \int r^2 dr (e^{\beta\mu(r)} + 2b_2 e^{2\beta\mu(r)} + 3b_3 e^{3\beta\mu(r)}) = N, \quad (5)$$

where the local chemical potential  $\mu(r) = \mu_0 - m\omega^2 r^2/2$  is computed within the local density approximation.

---

[1] E. Braaten and H.-W. Hammer, “Universality in few-body systems with large scattering length,” *Phys. Rep.* **428**, 259–390 (2006).

- [2] V. Efimov, “Energy levels arising from resonant two-body forces in a three-body system,” *Phys. Lett. B* **33**, 563–564 (1970).
- [3] V. Efimov, “Weakly-bound states of three resonantly-interacting particles,” *Sov. J. Nucl. Phys.* **12**, 589–595 (1971).
- [4] V. Efimov, “Low-energy property of three resonantly interacting particles,” *Sov. J. of Nucl. Phys.* **29**, 1058–1069 (1979).
- [5] Y. Nishida, Y. Kato, and C. D. Batista, “Efimov effect in quantum magnets,” *Nature Phys.* **9**, 93–97 (2013).
- [6] J. Maji, S. M. Bhattacharjee, F. Seno, and A. Trovato, “When a DNA triple helix melts: an analogue of the Efimov state,” *New J. Phys.* **12**, 10.1088/1367-2630/12/8/083057 (2010).
- [7] C. Chin, R. Grimm, P. Julienne, and E. Tiesinga, “Feshbach resonances in ultracold gases,” *Rev. Mod. Phys.* **82**, 1225–1286 (2010).
- [8] N. Gross, Z. Shotan, S. Kokkelmans, and L. Khaykovich, “Observation of universality in ultracold  $^7\text{Li}$  three-body recombination,” *Phys. Rev. Lett.* **103**, 163202 (2009).
- [9] S. E. Pollack, D. Dries, and R. G. Hulet, “Universality in three- and four-body bound states of ultracold atoms,” *Science* **326**, 1683–1685 (2009).
- [10] M. Zaccanti, B. Deissler, C. D’Errico, M. Fattori, M. Jona-Lasinio, S. Müller, G. Roati, M. Inguscio, and G. Modugno, “Observation of an Efimov spectrum in an atomic system,” *Nature Phys.* **5**, 586–591 (2009).
- [11] B. S. Rem, A. T. Grier, I. Ferrier-Barbut, U. Eismann, T. Langen, N. Navon, L. Khaykovich, F. Werner, D. S. Petrov, F. Chevy, and C. Salomon, “Lifetime of the Bose gas with resonant interactions,” *Phys. Rev. Lett.* **110**, 163202 (2013).
- [12] J. von Stecher, “Weakly bound cluster states of Efimov character,” *J. Phys. B* **43**, 101002 (2010).
- [13] M. Thøgersen, D. V. Fedorov, and A. S. Jensen, “N-body Efimov states of trapped bosons,” *EPL* **83**, 30012 (2008).
- [14] R. J. Fletcher, A. L. Gaunt, N. Navon, R. P. Smith, and Z. Hadzibabic, “Stability of a unitary Bose gas,” *Phys. Rev. Lett.* **111**, 125303 (2013).
- [15] P. Makotyn, C. E. Klauss, D. L. Goldberger, E. A. Cornell, and D. S. Jin, “Universal dynamics of a degenerate unitary Bose gas,” preprint at <http://arxiv.org/abs/1308.3696>.
- [16] Y. Castin and F. Werner, “Le troisième coefficient du viriel du gaz de Bose unitaire,” *Canad.*

- J. Phys. **91**, 382–389 (2013).
- [17] M. Berninger, A. Zenesini, B. Huang, W. Harm, H.-C. Nägerl, F. Ferlaino, R. Grimm, P. S. Julienne, and J. M. Hutson, “Universality of the three-body parameter for Efimov states in ultracold cesium,” Phys. Rev. Lett. **107**, 120401 (2011).
- [18] J. Wang, J. P. D’Incao, B. D. Esry, and C. H. Greene, “Origin of the three-body parameter universality in Efimov physics,” Phys. Rev. Lett. **108**, 263001 (2012).
- [19] R. J. Wild, P. Makotyn, J. M. Pino, E. A. Cornell, and D. S. Jin, “Measurements of Tan’s contact in an atomic Bose-Einstein condensate,” Phys. Rev. Lett. **108**, 145305 (2012).
- [20] L. H. Thomas, “The interaction between a neutron and a proton and the structure of  $H^3$ ,” Phys. Rev. **47**, 903–909 (1935).
- [21] R. P. Feynman, *Statistical mechanics: A set of lectures* (Addison-Wesley, 1982).
- [22] W. Krauth, “Quantum Monte Carlo calculations for a large number of bosons in a harmonic trap,” Phys. Rev. Lett. **77**, 3695–3699 (1996).
- [23] W. Krauth, *Statistical Mechanics: Algorithms and Computations* (Oxford University Press, 2006).
- [24] E. L. Pollock and D. M. Ceperley, “Simulation of quantum many-body systems by path-integral methods,” Phys. Rev. B **30**, 2555–2568 (1984).
- [25] D. M. Ceperley, “Path integrals in the theory of condensed helium,” Rev. Mod. Phys. **67**, 279–355 (1995).
- [26] H. A. Bethe and R. Peierls, “The scattering of neutrons by protons,” Proc. R. Soc. Lond., A **149**, 176–183 (1935).
- [27] T.-L. Ho and Q. Zhou, “Obtaining the phase diagram and thermodynamic quantities of bulk systems from the densities of trapped gases,” Nature Phys. **6**, 131–134 (2010).
- [28] K. Huang, *Statistical mechanics*, 2nd ed. (Wiley, 1987).
- [29] F. Dalfovo, S. Giorgini, L. P. Pitaevskii, and S. Stringari, “Theory of Bose-Einstein condensation in trapped gases,” Rev. Mod. Phys. **71**, 463–512 (1999).
- [30] L. D. Landau and L. M. Lifshitz, *Statistical physics*, 3rd ed., Course of theoretical physics No. 5 (Butterworth-Heinemann, 1980).
- [31] R. Schmidt, S.P. Rath, and W. Zwerger, “Efimov physics beyond universality,” EPJ B **85**, 386 (2012).
- [32] S. Roy, M. Landini, A. Trenkwalder, G. Semeghini, G. Spagnolli, A. Simoni, M. Fattori,

- M. Inguscio, and G. Modugno, “Test of the universality of the three-body Efimov parameter at narrow Feshbach resonances,” *Phys. Rev. Lett.* **111**, 053202 (2013).
- [33] J. P. D’Incao, H. Suno, and B. D. Esry, “Limits on universality in ultracold three-boson recombination,” *Phys. Rev. Lett.* **93**, 123201 (2004).
- [34] N. P. Mehta, Seth T. Rittenhouse, J. P. D’Incao, J. von Stecher, and Chris H. Greene, “General theoretical description of n-body recombination,” *Phys. Rev. Lett.* **103**, 153201 (2009).
- [35] W. Li and T.-L. Ho, “Bose gases near unitarity,” *Phys. Rev. Lett.* **108**, 195301 (2012).
- [36] F. Ferlaino, S. Knoop, M. Berninger, W. Harm, J. P. D’Incao, H.-C. Nägerl, and R. Grimm, “Evidence for universal four-body states tied to an Efimov trimer,” *Phys. Rev. Lett.* **102**, 140401 (2009).
- [37] C. H. Greene, “Universal insights from few-body land,” *Physics Today* **63**, 40 (2010).
- [38] K. Binder, “Theory of first-order phase transitions,” *Rep. Prog. Phys.* **50**, 783 (1987).
- [39] J. W. Cahn and J. E. Hilliard, “Free energy of a nonuniform system. I. Interfacial free energy,” *J. Chem. Phys.* **28**, 258–267 (2004).
- [40] I.M. Lifshitz and V.V. Slyozov, “The kinetics of precipitation from supersaturated solid solutions,” *J. Phys. Chem. Solids* **19**, 35–50 (1961).

## END NOTES

### Acknowledgements

We thank S. Balibar, Y. Castin, F. Chevy, I. Ferrier-Barbut, A. T. Grier, B. Rem, C. Salomon, and F. Werner for very helpful discussions. W.K. acknowledges the hospitality of the Aspen Center for Physics, which is supported by the National Science Foundation Grant No. PHY-1066293.

### Author contributions statement

Both authors contributed equally to this work.

**Conflict of interest statement**

The authors declare no conflicting interests.

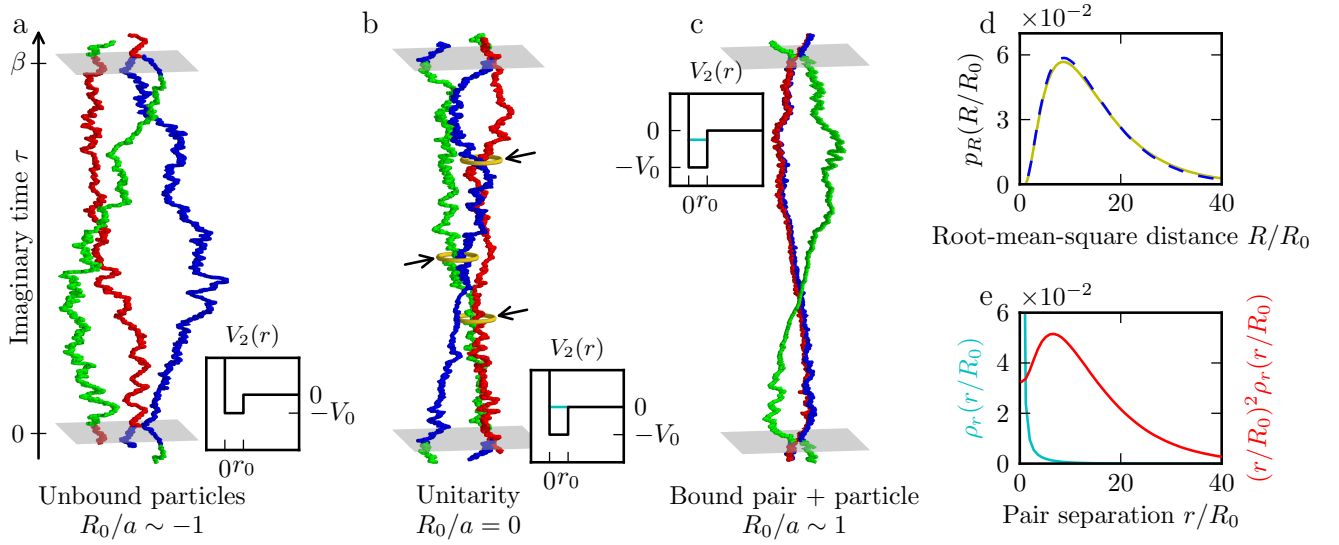


Figure 1. **Path-integral representation of three bosons at different scattering lengths** at  $R_0/\lambda_{\text{th}} = 1.3 \times 10^{-2}$  (for the graphical projection of  $(x, y, z, \tau)$  to three dimensions, see the Methods section). **a.** At  $R_0/a \sim -1$ , bosons are unbound and fluctuate on a scale  $\lambda_{\text{th}}$ . **b.** At unitarity ( $R_0/a = 0$ ), pairs of bosons form and break up throughout the imaginary time (yellow highlights, arrows), forming a three-body state bound by pair effects. **c.** At  $R_0/a \sim 1$ , two bosons bind into a stable dimer (*red, blue*) and one boson is unbound (*green*). Insets in **a-c** correspond to finite-range versions of the zero-range interaction used in each case. Blue levels correspond to the dimer energy. **d.** Sample-averaged hyperradial (root-mean-square pair distance) probability  $p_R(R)$  at constant  $\tau$  (*solid yellow*) compared to its analytic zero-temperature value (*dashed blue*). **e.** Sample-averaged pair distribution  $\rho_r(r)$ , diverging  $\propto 1/r^2$  as  $r \rightarrow 0$ , and asymptotically constant  $r$ -shell probability  $r^2 \rho_r(r)$ , in agreement with the Bethe–Peierls condition. Data in this figure concern co-cyclic particles in a shallow trap of  $\omega \sim 0$ .

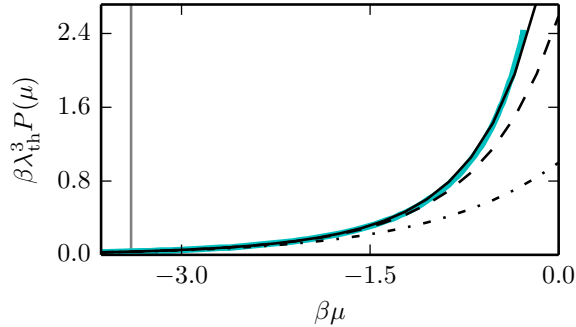


Figure 2. **Equation of state of unitary bosons in a harmonic trap** at  $R_0/a_\omega = 0.18$  and  $T/T_{\text{BEC}}^0 = 1.05$  and  $N = 100$ . The numerical equation of state of the normal gas for  $N = 100$  (*solid cyan line*) obtained by ensemble averaging of configurations[27] is compared to the theoretical virial expansion up to the 1st (*dash-dotted black line*), 2nd (*dashed black line*), and 3rd (*solid black line*) virial coefficients. The vertical gray line indicates the most central region of the trap used to determine  $\mu_0$  by comparison to an ideal gas.

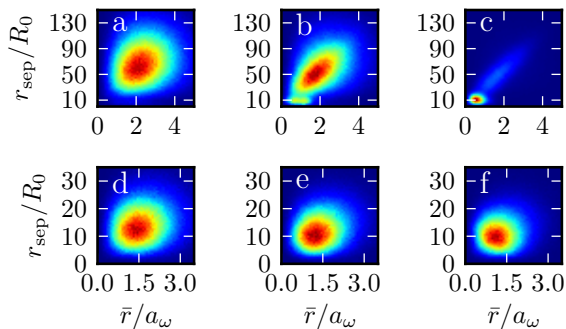


Figure 3. **Two-dimensional histogram of pair distances  $r_{\text{sep}}$  and centre-of-mass positions  $\bar{r}$  for  $N = 100$  bosons.** **Upper panels:** *First-order phase transition for  $R_0/a_\omega = 0.07$ .* **a.** At  $T/T_{\text{BEC}}^0 = 1.7$ , the distribution is that of the normal phase. **b.** At a slightly lower temperature  $T/T_{\text{BEC}}^0 = 1.6$ , a second peak with smaller pair distances  $\sim 10R_0$  appears in the trap centre. **c.** At  $T/T_{\text{BEC}}^0 = 1.5$ , most particles are in the trap centre, with small pair distances  $\sim 10R_0$ . **Lower panels:** *Smooth dependence of pair distances and densities on temperature.* At  $R_0/a_\omega = 0.23$ , the pair distances decrease smoothly between  $T/T_{\text{BEC}}^0 = 0.9$  (**d**) and  $T/T_{\text{BEC}}^0 = 0.8$  (**e**) and has stabilized around  $10R_0$  at  $T/T_{\text{BEC}}^0 = 0.7$  (**f**).

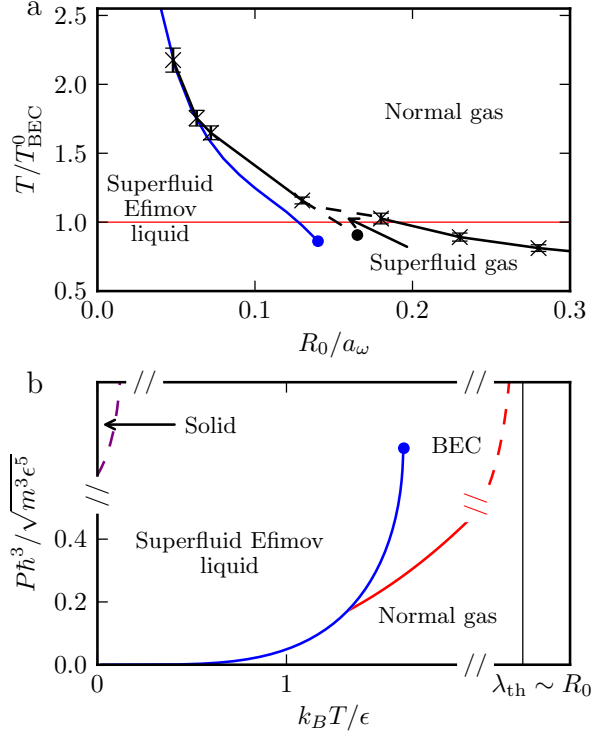


Figure 4. **Phase diagram of unitary bosons in the trap centre and in homogeneous space.** **a.** In the harmonic trap, depending on the value of  $R_0/a_\omega$ , we observe a normal-gas-to-superfluid-liquid first-order phase transition or a conventional second-order Bose–Einstein phase transition (*solid, black lines*). The error bars indicate the last value of  $T$  at which the system was a pure normal gas, and the first value of  $T$  at which we observed either the superfluid Efimov liquid or the Bose–Einstein condensate. The normal-gas-to-superfluid-liquid phase transition corresponds well to our theoretical model (*solid, blue line*) at high temperatures. Consistently with theoretical predictions, the numerical coexistence lines are qualitatively continued to a triple point and a critical point (*dashed black lines*). **b.** In a homogeneous system, the normal-gas-to-superfluid-liquid coexistence line (*solid, blue*) and the conventional Bose–Einstein condensation line (*solid, red*) are universal. The predicted divergence of the normal-gas-to-superfluid-liquid coexistence line (*dashed, red*) and the phase transition to a solid phase (*dashed, purple*) are non-universal physics specific to our interaction model.

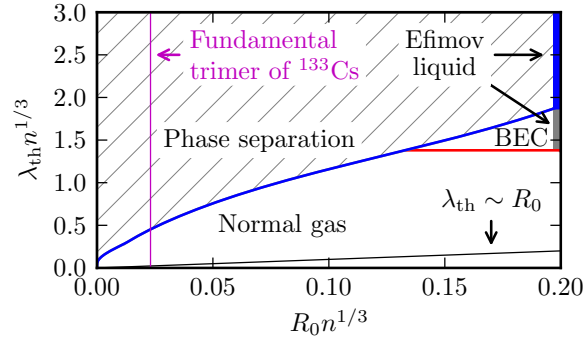


Figure 5. **Homogeneous phase diagram of unitary bosons: comparison with experimental densities.** (Data of Fig. 4b expressed through the dimensionless numbers  $\lambda_{\text{th}} n^{1/3}$  and  $R_0 n^{1/3}$ .) In the coexistence region, the system phase-separates into the superfluid Efimov liquid (*thick blue line*) and, depending on temperature, the normal gas or the Bose–Einstein condensate. At high density, the Bose–Einstein condensate undergoes a cross-over to Efimov liquid behaviour (*thick gray line*). The value of  $R_0 n^{1/3} \sim 0.023$  corresponding to the fundamental trimer of  $^{133}\text{Cs}$  at density  $n = 10^{13} \text{ cm}^{-3}$  is indicated by the vertical magenta line.



## Résumé

Cette thèse porte sur l'étude du gaz de Bose aux grandes longueurs de diffusion à l'aide de simulations Monte-Carlo quantiques par intégrale de chemin. Dans un premier chapitre, ce type de simulation est présenté en l'illustrant par l'exemple du gaz de Bose libre. À l'aide d'une simulation Monte-Carlo quantique qui reproduit quantitativement à la fois des résultats expérimentaux et des prédictions théoriques, le deuxième chapitre décrit la physique du gaz de Bose dans le régime où les interactions deviennent trop fortes pour que les théories de champ moyen s'appliquent.

La seconde partie de cette thèse concerne la situation où les interactions entre les bosons sont résonantes, appelée régime unitaire. Dans cette situation, bien que deux bosons ne puissent former un état lié, trois bosons peuvent former un état trimère. Cet effet contre-intuitif, nommé effet Efimov, est étudié dans le troisième chapitre de cette thèse, à l'aide la fois d'arguments théoriques et d'une simulation Monte-Carlo quantique de trois bosons. Dans un quatrième chapitre, cette simulation sert de base à une simulation du gaz de Bose unitaire, qui reproduit des résultats théoriques à haute température et prédit l'existence d'un liquide quantique à basse température, de la même origine physique que l'effet Efimov.

**Mots-clefs : simulation Monte-Carlo quantique, gaz de Bose unitaire, transition de phase, effet Efimov, intégrales de chemin, atomes froids.**

## Abstract

This thesis deals with the Bose gas at large scattering lengths using quantum path-integral Monte Carlo simulations. In the first chapter, this type of simulation is presented through the example of the free Bose gas. The second chapter describes the Bose gas in the regime where interactions become too strong for mean-field theories to be accurate, using a quantum Monte Carlo simulation that quantitatively reproduces both experimental results and theoretical predictions.

The second part of this thesis concerns the situation in which the interactions between bosons are resonant, called the unitary regime. In this situation, although two bosons cannot bind, three bosons may form a trimer state. This counter-intuitive effect, called the Efimov effect, is studied in the third chapter of this thesis, both through theoretical arguments and a dedicated three-body quantum path-integral Monte Carlo simulation. In the fourth chapter, this simulation serves as the building block of a simulation of the unitary Bose gas, that reproduces high-temperature theoretical results and predicts the existence of a low-temperature quantum liquid phase, of the same physical origin as the Efimov effect.

**Keywords: quantum Monte Carlo simulation, unitary Bose gas, phase transition, Efimov effect, path integrals, cold atoms.**